DEVELOPMENT OF NANOTECHNOLOGY FOR

MEDICAL SENSOR APPLICATIONS

TIK OUIRAM

DOCTOR OF PHILOSOPHY IN APPLIED CHEMISTRY

MAEJO UNIVERSITY

2019

DEVELOPMENT OF NANOTECHNOLOGY FOR

MEDICAL SENSOR APPLICATIONS

TIK OUIRAM

A DISSERTATION SUBMITTED IN PARTIAL FULFILLMENT

OF THE REQUIREMENTS FOR THE DEGREE OF DOCTOR OF PHILOSOPHY

IN APPLIED CHEMISTRY

ACADEMIC ADMINISTRATION AND DEVELOPMENT MAEJO UNIVERSITY

2019

DEVELOPMENT OF NANOTECHNOLOGY FOR
MEDICAL SENSOR APPLICATIONS

TIK OUIRAM

THIS THESIS HAS BEEN APPROVED IN PARTIAL FULFLLMENT

OF THE REQUIREMENTS FOR THE DEGREE OF DOCTOR OF PHILOSOPHY

IN APPLIED CHEMISTRY

APPROVED BY   Advisory Committee

Chair ....

(Assistant Professor Dr. Tanin Tangkuaram)

………………./………………/ ……………

Committee ....

(Assistant Professor Dr. Anchana Preechaworapun)

………………./………………/ ……………

Committee ....

(Dr. Sairoong Muangpil)

………………./………………/ ……………

Program Chair, Doctor of Philosophy ....

in Applied Chemistry   (Assistant Professor Dr. Supaporn Sangsrichan)

………………./………………/ ……………

CERTIFIED BY ACADEMIC   ....

ADMINISTRATION AND DEVELOPMENT

(Associate Professor Dr. Yanin Opatpatanakit)

Acting Vice President for the Acting President of

Maejo University

………………./………………/ ……………

ชื่อเรื่อง   การพัฒนานาโนเทคโนโลยีสำหรับประยุกต์ใช้เป็นเซนเซอร์ด้านการแพทย์
ชื่อผู้เขียน   นายติ๊ก อุ้ยรัมย์
ชื่อปริญญา   ปรัชญาดุษฎีบัณฑิต สาขาวิชาเคมีประยุกต์
อาจารย์ที่ปรึกษาหลัก ผู้ช่วยศาสตราจารย์ ดร.ธานินทร์ แตงกวารัมย์

บทคัดย่อ

คอปเปอร์ (I) ออกไซด์แอทแมงกานีส (IV) ออกไซด์ เป็นวัสดุใหม่ที่ถูกสังเคราะห์ขึ้นและถูกนำไปใช้สำหรับดัดแปลงลงบนพื้นผิวหน้าขั้วไฟฟ้ากลาสสิคาร์บอน เพื่อใช้เป็นไฮโดรเจนเปอร์ออกไซด์เซนเซอร์ วัสดุคอมโพสิตนี้ถูกศึกษาโครงสร้างและลักษณะทางสัณฐานวิทยาโดยใช้กล้องจุลทรรศน์อิเล็กตรอนแบบส่องกราด เทคนิคการกระจายพลังงานของรังสีเอกซ์ เทคนิควิเคราะห์การเลี้ยวเบนของรังสีเอ็กซ์ และฟูเรียทรานฟอร์มอินฟราเรดสเปกโทรสโกปี คอปเปอร์ (I) ออกไซด์แอทแมงกานีส (IV) ออกไซด์แสดงการตอบสนองทางไฟฟ้าที่ดีเยี่ยมต่อปฏิกิริยาออกซิเดชั่นของไฮโครเจนเปอร์ออกไซด์ ซึ่งให้ค่าคงที่อัตราการแลกเปลี่ยนประจุเท่ากับ 0.56 ต่อวินาที ค่าสัมประสิทธิ์การแพร่กระจาย 1.65×10^{-5} ตารางเซนติเมตรต่อวินาที พื้นที่ผิวของการเกิดปฏิกิริยา 0.12 ตารางมิลลิเมตร และความเข้มข้นพื้นผิวปกคลุม 1.04×10^{-8} โมลต่อตารางเซนติเมตร ในสภาวะที่เหมาะสมเซนเซอร์ที่สร้างขึ้นจะได้ช่วงความเป็นเส้นตรงตั้งแต่ 0.5 ไมโครโมลาร์ ถึง 20 มิลลิโมลาร์ โดยมีขีดจำกัดการตรวจวัดที่ต่ำ 63 นาโนโมลาร์ (3 เท่าของกระแสพื้น) และความไวที่ดี 256.33 ไมโครแอมแปร์ต่อมิลลิโมลาร์ต่อตารางเซนติเมตร นอกจากนี้ยังมีความเสถียรสูง (± 15%, n = 100) ความสามารถในการตรวจวัดซ้ำ (1.25% RSD, n=10) และความสามารถในการผลิตซ้ำ (3.55% RSD, n = 10) ผลการวิจัยพบว่าคอปเปอร์ (I) ออกไซด์แอทแมงกานีส (IV) ออกไซด์ เป็นแพลตฟอร์มใหม่สำหรับการตรวจวัดไฮโดรเจนเปอร์ออกไซด์

วัสดุโลหะคอมโพสิตเซอร์โคเนียมเคลือบอนุภาคทองนาโนพาทิเคิล คอปเปอร์(I)ออกไซด์แอทแมงกานีส (IV) ออกไซด์ และตรึงโคลีนออกซิเดสลงบนขั้วไฟฟ้ากลาสสิคาร์บอน (Cox/Cu$_2$O@MnO$_2$/ZrO$_2$@AuNPs/GCE) ถูกพัฒนาขึ้นเพื่อเพิ่มคุณสมบัติในการเร่งปฏิกิริยาทางเคมีไฟฟ้า สภาพความไวและสเถียรภาพของแอมเปอร์โรเมทริกโคลีนไบโอเซนเซอร์ ขั้วไฟฟ้าที่ปรับปรุงแสดงการตอบสนองทางไฟฟ้าที่ดีเยี่ยมต่อการเกิดปฏิกิริยาออกซิเดชันของไฮโดรเจนเปอร์ออกไซด์ ที่เกิดจากปฏิกิริยาออกซิเดชันของโคลีน ซึ่งค่าอัตราค่าคงที่การแลกเปลี่ยนประจุเท่ากับ 0.97 ต่อวินาที, ค่าสัมประสิทธิการแพร่เท่ากับ 4.50×10^{-6} ตารางเซนติเมตรต่อวินาที, พื้นที่ผิวขั้วไฟฟ้าไฟฟ้าที่เกิดปฏิกิริยา 0.24 ตารางมิลลิเมตร และความเข้มข้นที่ผิวหน้าขั้วไฟฟ้า 0.54×10^{-8}

โมลต่อตารางเซนติเมตร ขั้วไฟฟ้าที่ได้รับการปรับปรุงสามารถตรวจวัดโคลีนได้ในช่วงความเป็น
เส้นตรง 0.5 ถึง 1000 ไมโครโมลาร์ มีสภาพความไว 97.4 ไมโครแอมแปร์ต่อตารางเซนติเมตรต่อ
มิลลิโมลาร์ และขีดจำกัดการตรวจวัดที่ต่ำ (0.3 ไมโครโมลาร์) โคลีนไบโอเซนเซอร์แสดงให้เห็นค่า
การตรวจวัดซ้ำที่มีประสิทธิภาพสูง (%RSD = 2.90, n = 5), การผลิตซ้ำที่ดีเยี่ยม (%RSD = 2.90, n
= 5) สามาถใช้งานได้หลายครั้ง (n = 28 with %I > 50.00%) และมีความจำเพาะ ไม่ถูกรบกวน
จากจากสารที่มีผลทางไฟฟ้าเช่น กรดแอสคอร์บิค แอสไพริน อะมอกซีซิลิน คาแฟอีน โดปามีน
กลูโคส ซูโครส และกรดยูริก วิธีการที่ดีที่สุดนี้ถูกนำไปใช้ในการตรวจวัดโคลีนในตัวอย่างเลือดมนุษย์
ซึ่งแสดงให้เห็นถึงความแม่นยำและความน่าเชื่อถือที่ยอดเยี่ยมในช่วงการกลับคืน 97.1 ถึง 103.90%

คำสำคัญ : ไฮโดรเจนเปอร์ออกไซด์, โคลีนไบโอเซนเซอร์, วัสดุคอมโพสิต, ไซคลิกโวลแทมเมทรี, แอม
เปอร์โรเมทริกไบโอเซนเซอร์

Title	DEVELOPMENT OF NANOTECHNOLOGY FOR MEDICAL SENSOR APPLICATIONS
Author	Mr. Tik Ouiram
Degree	Doctor of Philosophy in Applied Chemistry
Advisory Committee Chairperson	Assistant Professor Dr. Tanin Tangkuaram

ABSTRACT

A novel composite material of copper (I) oxide at manganese (IV) oxide ($Cu_2O@MnO_2$), was synthesized and applied for modification on the glassy carbon electrode (GCE) surface ($Cu_2O@MnO_2$/GCE) as a hydrogen peroxide (H_2O_2) sensor. The composite material was characterized regarding its structural and morphological properties using field emission scanning electron microscopy (FE-SEM), energy-dispersive X-ray spectroscopy (EDX), X-ray diffraction (XRD) and Fourier transform infrared spectroscopy (FTIR). The $Cu_2O@MnO_2$/GCE showed an excellent electrocatalytic response to the oxidation of H_2O_2 which provided a 0.56 s^{-1} charge transfer rate constant, 1.65×10^{-5} cm^2 s^{-1} diffusion coefficient value, 0.12 mm^2 electroactive surface area and 1.04×10^{-8} mol cm^{-2} surface concentration. At the optimal condition, the constructed sensor exhibited a wide linear range from 0.5 μM to 20 mM with a low limit of detection of 63 nM. (S/N = 3) and a good sensitivity of 256.33 μA mM^{-1} cm^{-2}. It also presented high stability (± 15.00%, n=100), repeatability (1.25% RSD, n=10) and reproducibility (3.55% RSD, n=10). The results indicated that the synthesized $Cu_2O@MnO_2$ was successfully used as a new platform for H_2O_2 sensing.

A novel metal composite material based on zirconium dioxide coated gold nanoparticles ($ZrO_2@AuNPs$), copper (I) oxide at manganese (IV) oxide ($Cu_2O@MnO_2$) and immobilized choline oxidase (Cox) onto a glassy carbon electrode (GCE) (Cox/$Cu_2O@MnO_2$/$ZrO_2@AuNPs$/GCE) has been developed for enhancing the electrocatalytic property, sensitivity and stability of the amperometric choline biosensor. The Cox/$Cu_2O@MnO_2$/$ZrO_2@AuNPs$/GCE displayed an excellent

electrocatalytic response to the oxidation of the byproduct H_2O_2 from the choline catalyzed reaction, which exhibited charge transfer rate constant of 0.97 s^{-1}, diffusion coefficient value 4.50×10^{-6} cm^2 s^{-1}, electroactive surface area 0.24 mm^2 and surface concentration 0.54×10^{-8} mol cm^{-2}. The modified electrode also provided a wide linear range of choline concentration from 0.5 to 1,000.0 μM with good sensitivity (97.4 μA cm^{-2} mM^{-1}) and low detection limit (0.3 μM). This choline biosensor presented high repeatability (%RSD = 2.90, n = 5), excellent reproducibility (%RSD = 2.90, n = 5), long time usage (n = 28 with %I > 50.0%) and good selectivity without interfering effects from possible electroactive species such as ascorbic acid, aspirin, amoxicillin, caffeine, dopamine glucose, sucrose and uric acid. This optimal method was successfully applied for choline measurement in human blood samples which demonstrated highly accurate and excellent reliability in the recovery range from 97.10 to 103.90%.

ACKNOWLEDGEMENTS

TABLE OF CONTENTS

LIST OF TABLES

LIST OF FIGURES

LIST OF ABBREVIATIONS

A_e	Electroactive surface area
Abs	Absorbance
AuNPs	Gold nanoparticles
b	Cuvette's thickness
c	Sample concentration
$^{\circ}C$	Degree celsius
CHIT	Chitosan
COx	Choline oxidase
CE	Counter electrode
cm^{-1}	Per centimeter
cm^2	Square centimeter
CV	Cyclic voltammetry
D	Diffusion coefficient value
E	Potential
EDX	Energy-dispersive X-ray spectroscopy
EIS	Electrochemical impedance spectroscopy
E_{pa}	Anodic peak potential
E_{pc}	Cathodic peak potential
ε	Molar absorptivity
FE-SEM	Fiedld emission scanning electron microscopy
ELISA	Enzyme linked immunosorbent assay
FTIR	Fourier transform infrared spectroscopy
GC	Gas chromatography
GCE	Glassy carbon electrode
HPLC	High-performance liquid chromatography
I_{pa}	Anodic current
I_{pc}	Cathodic current
I_d	Diffusion current

L	Liter
M	Molar
MBA	Microsphere-based arrays
mg	Milligram
mg mL^{-1}	Milligram per milliliter
mL	Milliliter
mM	Milimolar
mm	Millimeter
nM	Nanomolar
PBS	Phosphate buffer
RE	References electrode
RIA	Radioimmunoassay
S	Second
S^{-1}	Per second
S/N	Signal to Noise
%T	%transmittance
UV	Ultra violet
UV-Vis	Ultra violet-visible
V	Volt
Vis	Visible
WE	Working electrode
XRD	X-ray diffraction
µg	Microgram
µL	Microliter
µM	Micro molar

CHAPTER 1

INTRODUCTION

1.1 Background

In the 21st century, the rapidly changing economy and society in Thailand critically affect to elderly population structure. This results from the lower birth rate that leads to the obvious different distribution of population by ages. The number of children under 15 years old has been predicted fallen from 14 to 9 million in 2005 to 2035. The working age population (aged 15 to 59) has been slightly changed. After that, the working age will become elder and also the child age will turn into the working population which will clearly decrease the working age population. Additionally, Thailand will completely steps into the elderly society because of the higher rate of elder population structure in the next 15 years which absolutely influences on the development of country in the next few decades.

Health problem is the major considering issue in the elder society, especially, depression disorder related to Alzheimer's disease ultimately. In the Ministry of Public Health of Thailand's report, it reveals that there are about 600,000 Thai people suffering from Alzheimer's disease in 2015 and will approximately increase up to 1,117,000 in 2030. From this point, the development in medical knowledge covering to public medical heath care service is needed to prevent and protect people to slower getting the symptom of Alzheimer's (Nestor et al., 2004).

The development of electrochemical sensors for hydrogen peroxide sensing and choline monitoring plays an important role in many fields such as clinic, pharmacy (Dunphy and Burinsky, 2003), industry (Näther et al., 2006), food (Zhang et al., 2019) and environment (Barnard and Stinson, 1999). Many of techniques have been studied and applied for quantitative analysis (spectrometry (Zeisel and daCosta, 1990), chemiluminescence (Marquette et al., 2003), fluorimetry (Říčný et al., 1992), titrimetry (Markunas and Riddick, 1952), photometry (Ohkawa et al., 2018) and chromato graphy (Van Zoonen et al., 1987), however the electrochemistry is an interesting dominant option and popularly used due to its simplicity, selectivity,

sensitivity, stability and fast determination (Stadler and Nesselhut, 1986). To further improve these properties to be more effective, the proper modification of electrode surface is an important key to enhance electrochemical analysis.

Thus, this research aims to apply an electrochemical technique for quantitative detection which the main purposes are focused on fabrication of electrochemical sensors for hydrogen peroxide sensing and its application as the developed choline biosensors. This method holds such a great promising of the possibility to provide low cost, accurate, minimal pre-treatment and rapid analysis of hydrogen peroxide and choline for humanity.

1.2 Objectives

1. To develop electrochemical sensors based on copper doped manganese oxide ($Cu_2O@MnO_2$) onto glassy carbon electrode (GCE) surface and then apply this method to be used as choline biosensors.

2. To develop biosensors based on zirconium dioxide coated gold nanoparticles ($ZrO_2@AuNPs$) , copper doped manganese oxide ($Cu_2O@MnO_2$) and immobilized choline oxidase (COx) onto glassy carbon electrode (GCE) surface for determination of choline in whole human blood samples.

3. To emphasize and present the knowledge about the importance of preliminary clinical diagnosis to the public based on the developed reliable and portable biosensors device.

1.3 Expectation

1. The electrochemical sensor based on copper doped manganese oxide ($Cu_2O@MnO_2$) onto glassy carbon electrode (GCE) surface for hydrogen peroxide sensing is successfully developed.

2. The choline biosensor is successfully fabricated.

3. Zirconium dioxide coated gold nanoparticles ($ZrO_2@AuNPs$) and copper doped manganese oxide ($Cu_2O@MnO_2$) are successfully synthesized and applied as

the modified materials for modification on ther glassy carbon electrode (GCE) surface.

4. The research is publicly presented and published by international journals.

CHAPTER 2

LITERATURE REVIEW

2.1 Biosensors

Biosensors is an biological sensing device relying on the biological reaction between biological substance and the target analyte which then provides the electrical signal or other kinds of detectable signal. In the last 30 years, biosensors and sensors have been increasingly developed in terms of financial supports, published reports and researchers. These results from the development of semiconductor industry which influences on novel various fabrications of tools and devices, especially, many kinds of sensors, such as hydrocarbon sensors in automotive industry and glucose biosensors in medical industry. Also, the development in micro-computer since 1980 has led to technological revolution in sensors and devices resulting in higher performance-price index. Biosensors has grown up in various fields, it has been increasingly used up to 60% per year in medicine, industry, and environment which provides the advantages as followings;

1. High sensitivity, sensitivity and stability.

2. Independent reaction on physical parameters such as pH and temperature, minimal pretreatment.

3 . Accuracy, precision, reproducibility, wide linearity and without interfering effects form electro-active species.

4. Invasive monitoring, minimal probe and biocompatibility.

5 . Moderate cost, small size, portability and semi-skilled operators without decentralization of laboratory.

6. Marketing supports and government subsidies.

Recently, the biochemical determination as biosensors has been developed by advanced sensing technology leading to the level of early manifest diagnosis for preliminary treatment of various diseases. This overcome the limitations as presented in previous analytical techniques such as gas chromatography (GC), high-performance liquid chromatography (HPLC), microsphere-based arrays (MBA), radioimmunoassay

(RIA) and enzyme linked immunosorbent assay (ELISA) in terms of monitoring time, expense, complicated operation and toxic reagents.

2.1.1 Biosensors component

Biosensors is a device including of two main parts, 1) biological substances or receptor and 2) transducer as shown in Figure 1.
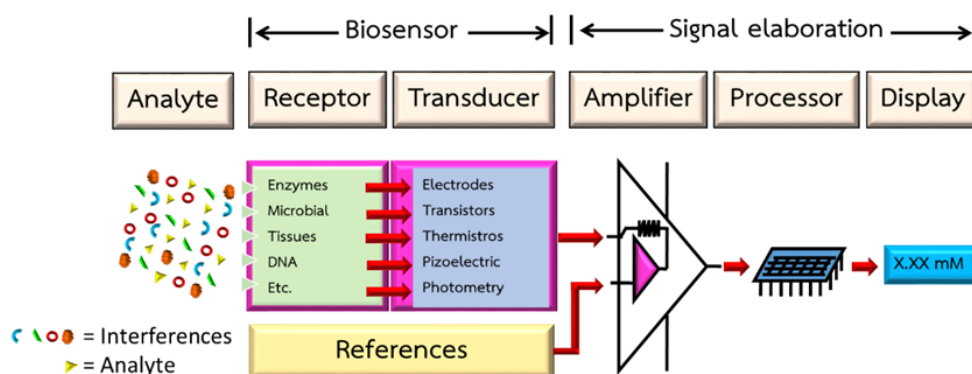
Figure 1 Schematic diagram of biosensors.

1) Biological substances or receptor, for instance, enzyme, microorganism, plant or animal tissues, DNA, antibody and etcetera; each biological substance specifically biochemical react to the target analyte and then provides the product and signal to be then operated by the transducer.

2) Receptor; it turns the obtained signal in terms of physical, chemical or biochemical patterns into electrical signal to be further processed in elaboration section.

There are many different combinations between receptors and transducers depending on each purpose of application as presented in Table 1.

Table 1 Biosensors' component.

Receptor	Transducer
Organism	Potentiometric
Tissue	Amperometric
Cells	Conductometric
Organelles	Impedimetric
Membranes	Optical
Enzymes	Calorimetric
Enzyme components	Acoustics
Receptors	Mechanical
Antibodies	Molecular electronic
Nucleic acids	
Organic molecules	

To obtain the signal as each evaluable or readable value, it requires amplifier, processor and signal elaboration for user.

2.1.2 Characteristics of biosensors

Effective biosensors require selectivity to each target analyte in each individual specific matrix. Thus, its effectiveness can be changed in different matrixes relying on temperature, pressure and interfering species in the system as briefly concluded in Table 2.

Table 2 Biosensors' characteristics.

Property	Definition
1. Simple mathematical relationships	Biosensors can immediately translate the detected signal to quantitative information compared to the linear equation.
2. None hysteresis	The signal rapidly gets back to the baseline after monitoring.
3. Response time	Biosensors provide fast response. If not, it results from kinetics of slow reaction which can be improved by the immobilization of biological receptors.
4. Signal to noise ratio (S/N)	Biosensors provide high ratio of signal to noise resulting in low limit of detection.
5. Selectivity	Biosensors provide high selectivity without the effect from interfering species in sample matrix.

According to practical principle, biosensors can be divided in two parts as shown below.

1) Direct recognition sensor; the signal is followed by the detected quantity which is directly related to the target analyte content.

2) Indirect detection sensor; the signal is followed by the obtained product of the reaction between biological substance and the target analyte which the detected quantity of product is related to the target analyte content as illustrated in Figure 2.
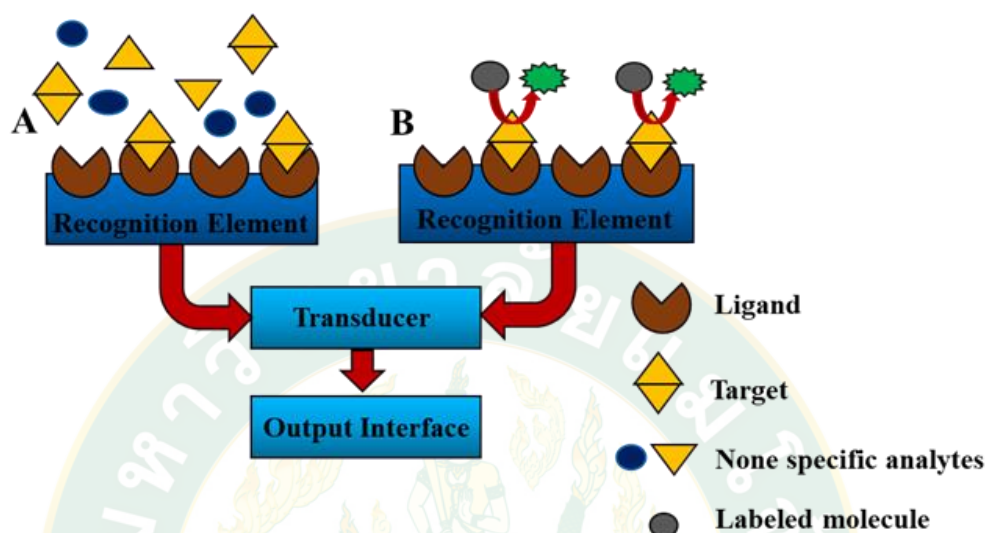
Figure 2 Biosensors' illustration: (A) direct recognition sensor
and (B) indirect recognition sensor.

The reaction between the biological substance and the target analyte mostly provides the electro-active product in both direct and indirect electrochemical reactions that can be detected the signal in terms of current by using amperometric transducer or potential by using potentiometric transducer, respectively. In the present, the signal processing of biosensors has been popularly used by applying the proper potential to electro-mediator in oxidation/reduction reactions and then detecting the obtained current, called "amperometric analysis".

Amperometry or amperometric transducer relies on oxidation/reduction reaction of the product or the electro-mediator in the biological system.

Biosensors can be fabricated based on immobilization of enzyme or other biological substances onto the working electrode surface which the enzyme then specifically reacts with the substrate (the target analyte) turning into the product or the electro-mediator. The applied proper potential to the oxidation/reduction

reaction of the product leads to the flow of electrons. The obtained current relates to the mediator quality and also the target analyte content according to stoichiometry. Additionally, biosensors can be called following to each target analyte such as hydrogen peroxide sensor, choline biosensor and etc.

2.2 Cyclic voltammetry (CV)

Cyclic voltammetry or CV is an electrochemical technique by applying potential as a cycle, forward and backward. This technique can be used for both qualitative and quantitative studies which the amount of electrons obtained from oxidation/reduction reaction in analysis directly relates to the content or the concentration of the target analyte.

Additionally, this technique provides simplicity and rapid analysis which its main composition can be presented in Figure 3. Potentiostat is an electronic device connected to the computer and operated by the specific software for electrochemical analysis that is used for controlling the applied potential and detection of the current response. For the experimental operation, it is connected to three-system electrochemical cells as following;
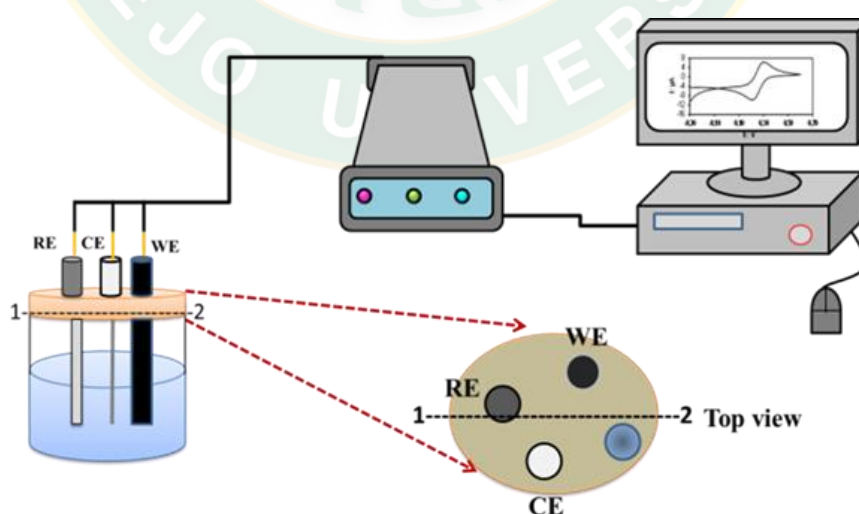
Figure 3 Cell diagram of amperometric detection consisting of reference electrode (RE), counter electrode (CE) and working electrode (WE).

1. Working electrode (WE); the reaction of the target electro-active specie occurs onto the WE surface. Normally, it can be made of various high stable materials such as glassy carbon, platinum and gold.

2. Reference electrode (RE); It is used as the reference with constant potential and compared to the working electrode to obtained the changed potential value of the working electrode.

3. Counter electrode (CE); It is important electrode to fulfill the system which platinum wire is popularly applied.

These aforementioned three electrodes are located near to each other but not connected. They all are dipped into the electrochemical cell. The cell is mostly made from glass. In the experiment, it contains the electrolyte solution in the presence of the target analyte. The electrolyte solution provides ions in the system resulting in high conductivity. The proper solvent and electrolyte solution are stable at the optimal condition and do not affect the oxidation/reduction reaction of the target analyte as well.

In this technique, the potentiostat apply the applied potential to each electrode which the potential between the working electrode and the reference electrode are controlled to linearly change of potential pattern. For example, the potential from V1 to V2 is called as switching potential which is illustrated the relation between the potential and time in Figure 4.
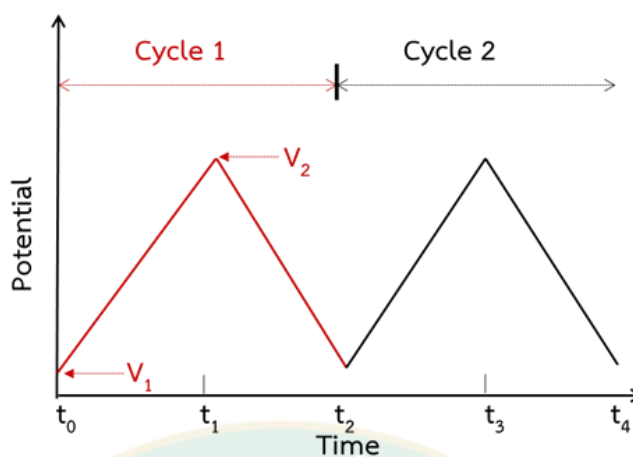
Figure 4 Cyclic voltammogram wave form.

Cyclic voltammogram of each reaction as shown above is a reversible reaction which the current response is obtained from the reaction or Faradaic current. This current response is obtained from the electron transfer of the redox reaction. The above peak is defined as an anodic peak of the oxidation reaction which the peak height is called anodic current or I_{pa} and the potential position of the peak is called anodic peak potential or E_{pa}. On the other hand, the below peak is defined as an cathodic peak of the reduction reaction which the peak height is called cathodic current or Ipc and the potential position of the peak is called cathodic peak potential or Epc in Figure 5
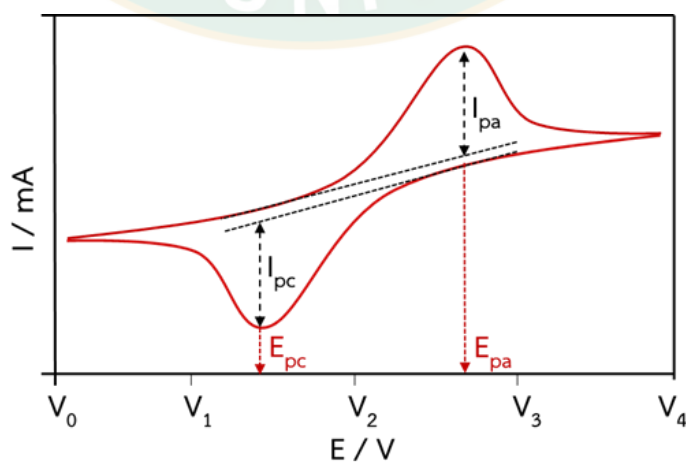
Figure 5 Cyclic voltammogram.

As the aforementioned, the important parameters in cyclic voltammogram are E_{pa}, E_{pc}, I_{pa} and I_{pc}. The rate of reduction reaction that is equal to the rate of oxidation reaction is called electrochemically reversible reaction and the peak separation can be defined as ΔE_p as the equation (1)

$$\Delta E_p = [E_{pa} - E_{pc}] - 2.303RT/nF \ \dots\dots\dots\dots\dots\dots\dots \ (1)$$

In conclusion, cyclic voltammetric technique is applied for study of the oxidation/reduction mechanism by potential scan which the peak and the current response can be noticed. In case of quantitative analysis, it can be applied with calibration curve and standard addition method.

2.3 Amperometry

Amperometry is an applied technique from voltammetric principal which provides the fixed potential value to the electrode and the reaction of the target analyte then occurs onto the electrode surface. The obtained current response relates to the sample concentration. As same as cyclic voltammetric technique, it can determine the sample with calibration curve and standard addition methods for quantitative analysis. In the experiment, it is operated under stirring condition which the current response results from mass transfer including of migration, convection and diffusion. The electrochemical cell for this technique is presented in Figure 6.
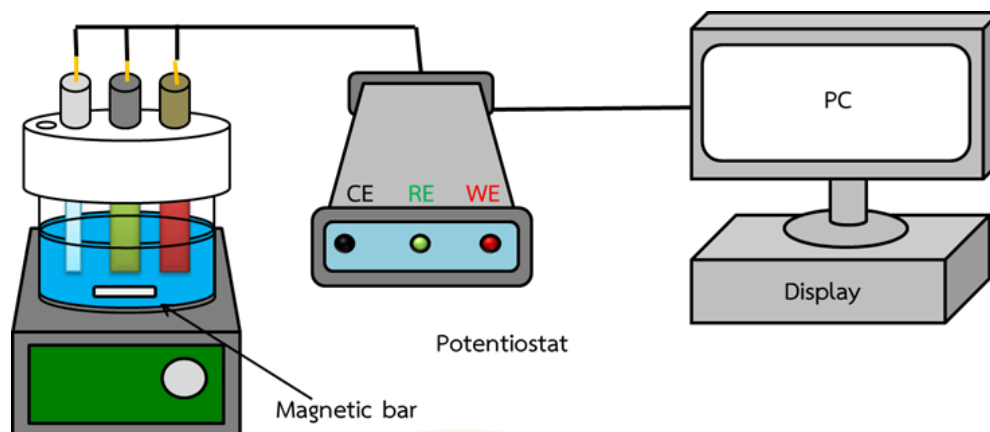
Figure 6 Electrochemical cell.

Migration is the movement of charged particles by the electric field. The contribution of migration to the total flux is directly relates to the ion charge, the ion concentration, the diffusion coefficient and the magnitude of the electric field gradient from the ion.

Convection is the random mass movement forced by mechanical (stirring) force or heat which results in convection current. This current is proportional to the stirring rate of solution.

Diffusion is a mass movement resulting from concentration gradient of the solution. In this system, the ions move at higher concentration to the lower that the entropy increases. The movement rate is proportional to the difference of concentration levels that relates to Fick's law. For the electrical cell in solution, the ion concentration at the electrode surface area almost decreases to zero. This differentiates the concentration level. After that, the ions in bulk solution area move to the electrode surface by diffusion process. So, the current is controlled by the rate of diffusion controlled current, called "Diffusion current (Id)".

The current responses (ΔI) of each analyte concentration level are obtained at fixed potential. The relation between the current response and standard concentration, calibration curve, is determined for quantitative analysis.

2.4 Fourier Transform Infrared Spectrometer (FTIR)

Fourier Transform Infrared Spectrometer is an instrument for materials characterization in all states (gas, liquid and solid) which is based on radiation absorption in infrared range with the wave number from 12,800 to 10 cm^{-1}.

Infrared radiation is invisible electromagnetic radiation which provides touchable heat. Its range is between visible radiation and microwave radiation that can be divided in 3 ranges as below;

1. Near Infrared (12800-4000 cm^{-1}).

2. Middle Infrared (4000-200 cm^{-1}).

3. Far Infrared (200-10 cm^{-1}).

Among these various ranges, Middle IR is applied for chemical analysis. Due to low energy of the radiation, when the molecules absorb the infrared radiation, it results in the transitions of molecules in Figure 7, vibration and rotation.

Each molecule can absorb infrared radiation at specific infrared's frequency which is equals to its vibration value. In this point, each organic substance has its own specific vibration value. Thus, this technique can be used to determine the structure and the group of each organic substance. The result from this technique is showed the relation between wave number and transmittance called Infrared spectra as in Figure 8.
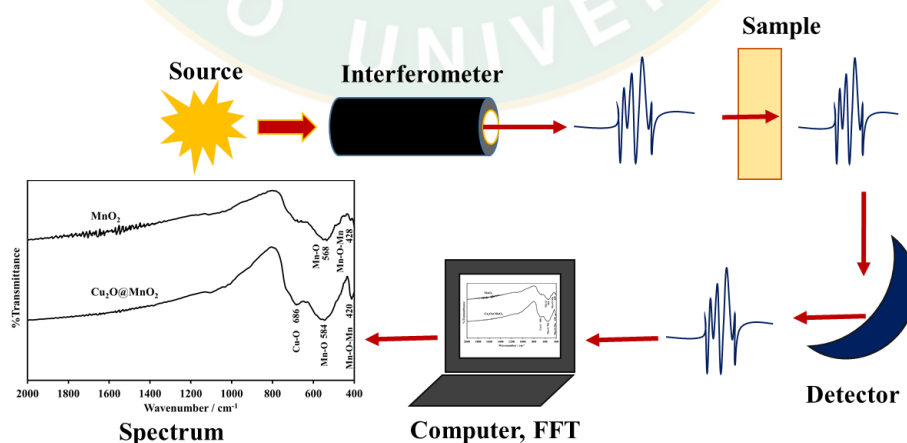
Figure 7 Schematic of FTIR spectrometer.
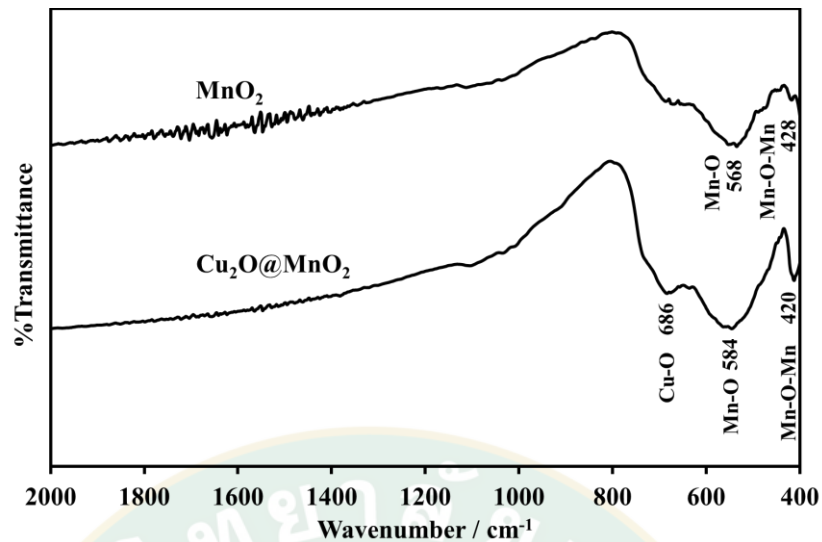
Figure 8 Infrared spectra.

The composition of FTIR spectrometer mainly includes of light source, interferometer sample, detector and computer.

2.5 UV-Visible spectrophotometer (UV-Vis)

UV-VIS Spectrophotometer is an instrument for characterization of materials based on radiation absorption in Ultra Violet (UV)-Visible (Vis) range from 190 to 1000 nm which each wavelength value relates to the quality and quantity of each substance in the sample. Following to Beer-Lambert's Law, the absorbance of the detected light passing by or reflecting by the sample compared to the light source at fixed wavelength directly relates to the amount of light-absorbing molecules. Therefore, this technique can be used for qualitative and quantitative analysis. In the present, UV-Visible spectrophotometer can be divided in two main types, single beam and double beam as shown in Figure 9 and Figure 10, respectively, which they both have same main compositions as following;
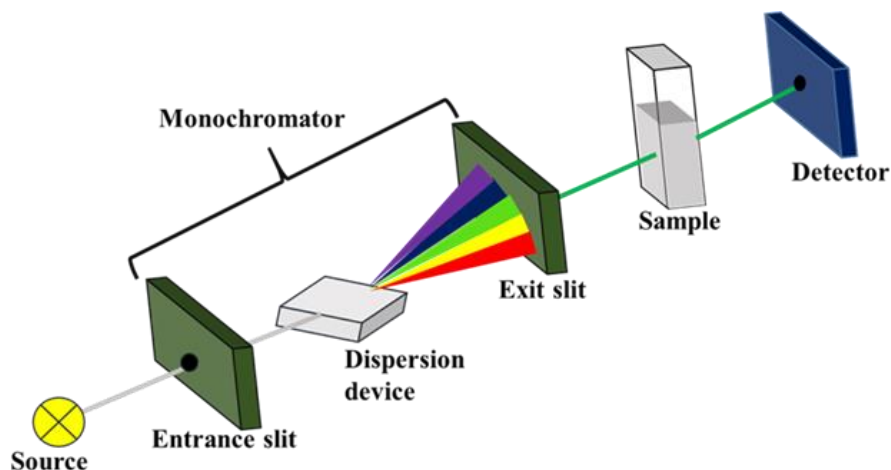
Figure 9 Composition of a single beam UV-visible spectrometer.
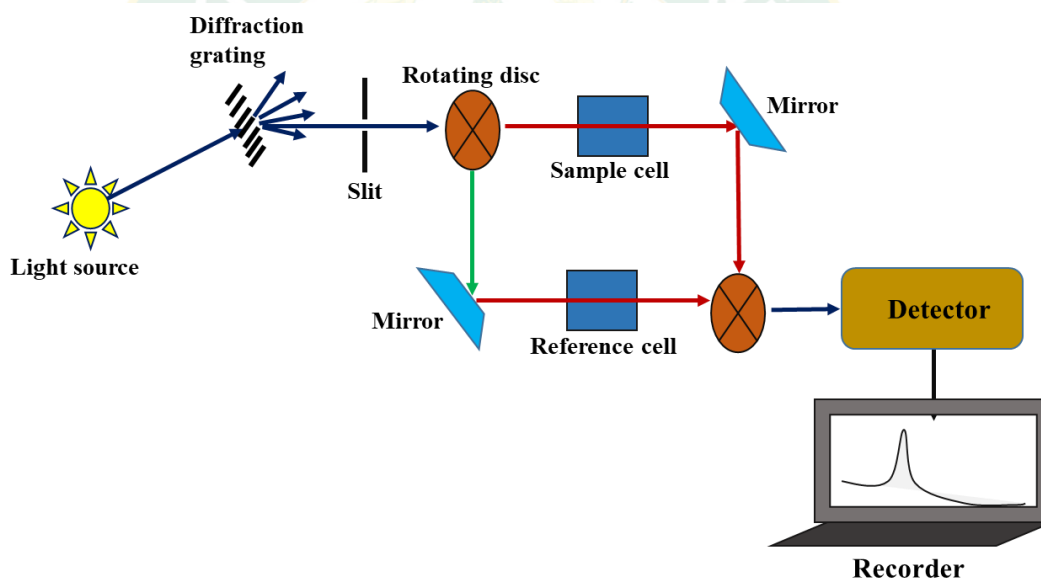
Figure 10 Composition of a double beam UV-visible spectrometer

1. Light source is the part of electromagnetic radiation source such as hydrogen lamp, deuterium lamp and tungsten lamp. For hydrogen lamp and deuterium lamp, they both provide UV radiation in the range between 160 to 380 nm. For tungsten lamp, it provides visible light from 240 to 2,500 nm.

2. Monochromator, for instance, grating and prism, is used for selecting each required wavelength from continuous multi-wavelengths provided by the light source turning into a single wavelength or specific wavelength.

3. Sample cell or cuvette (Figure 9), it can be used for sample analysis in all states (gas, liquid and solid). Thus, it can be made by different kinds of materials such as glass which is suitable for determination in UV range. Quartz and silica cuvettes, they are suitable for analysis in visible range. In double beam UV-Vis spectrophotometer, there is a reference cell that is used for containing the blank solution as shown in Figure 10.

4. Detector is used for detection of radiation intensity that is passed through or absorbed by the sample solution. The detected intensity is processed into electric signal. There are many kinds of detectors, for example, photovoltaic cell, photomultiplier tube, phototube and silicon diode detector.

5. Recorder is used for recording the signal obtained from the detector in term of absorbance (A) number or UV spectrum. The obtained graph is the relation between wavelength as X-axis versus absorbance (A) or %transmittance (%T) or molar absorptivity (ε) or log ε as Y-axis (Figure 11). Although the pattern of presented graph depends on each different kind of UV-Visible spectrophotometer, plotting Y-axis as absorbance is popularly used in the present.
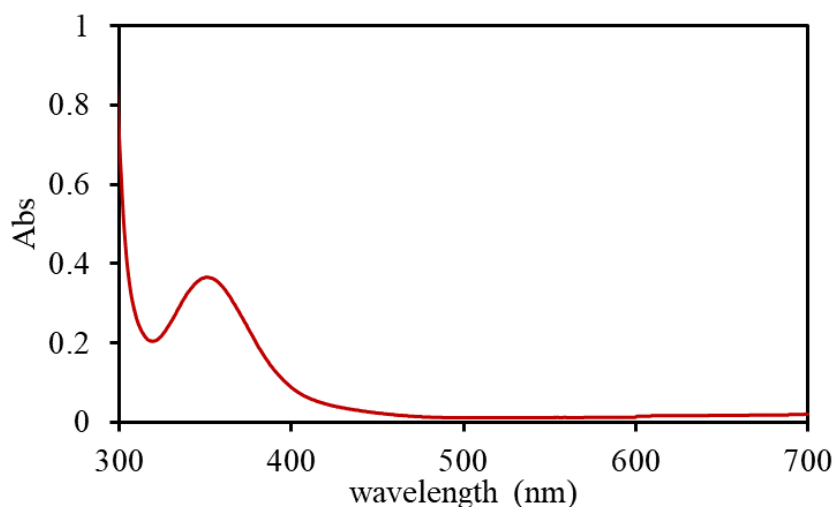
Figure 11 UV-visible spectrum.

Nowadays, spectrophotometer can be used for both qualitative and quantitative analysis. The principle operation of double beam spectrophotometer can be briefly discussed starting with the light source. It produces the light with multi-wavelength in the range of 200 to 800 nm which then is passed through the monochromator turning into specific wavelength radiation. After that, it is passed through sample cell and reference cell to determine the sample concentration compared to the obtained intensity from the blank solution. The detector processed the data and presents as electric signal, respectively. Therefore, the absorbance of blank solution is required to be detected and set up as zero before detecting the sample.

In case of unknown sample, the wavelength is scanned from the maximum value between 200 to 800 nm which the highest absorbance of UV spectrum peak is an applied wavelength for the unknown sample.

Beer-Lambert Law

The intensity or absorbance of an organic substance relies on Beer-Lambert Law when it absorbs UV-Visible radiation as the same energy as the energy between exciting state and ground state. Following Beer's Law, the intensity or absorbance

absorbed by each sample directly relates to the sample concentration when UV-Vis radiation passed through the sample solution. From Lambert's Law, the intensity or absorbance absorbed by each sample directly relates to the distance of light to the sample solution or cuvette's thickness when UV-Vis radiation passed through the sample solution (College of Life Science, 2016).

Therefore, the absorbance's relation following to Beer-Lambert Law can be presented as the equation (2).

$$A = \varepsilon bc \quad \text{.......................................} \quad (2)$$

A = absorbance
ε = molar absorptivity (M^{-1} cm^{-1})
b = cuvette's thickness (cm)
c = sample concentration (M or mol L^{-1})

Molar absorptivity is a constant depending on each kind of substance and the applied wavelength. The sample is detected by the instrument in term of transmittance as equation (3) or % transmittance as equation (4).

$$T = I/I_o \quad \text{...} \quad (3)$$
$$\text{or} \quad \%T = [I/I_o]\text{x}100 \quad \text{................................} \quad (4)$$

T = transmittance
I = intensity after passing by the sample solution
I_o = intensity before passing by the sample solution

$$\text{Thus} \quad I/I_o = \%T/100 \quad \text{..............................} \quad (5)$$

The relation between absorbance and intensity can be shown in equation (6)

$$A = -\log [I/Io] \quad ....(6)$$

Apply I / I_o from (5) into (6) to obtain the relation between absorbance and transmittance as equation (7).

$$A = -\log[\%T/100] = -\log T \quad ....(7)$$

However, the deviant of linearity can happen in Beer-Lambert Law as the following causes below;

- Sample concentration higher than 0.01 M leading to absorptivity coefficient and refractive index errors.

- Fluorescence, phosphorescence, decomposition and integration of the sample.

- Interfering radiation or stray.

2.6 Scanning Electron Microscope (SEM)

SEM principle basically consists of electron source which produces the electron for the system. Then, the obtained electron group is accelerated by electric field and passed through the condenser lens turning into electron beam which can be adjusted its size depending on the required quality of image resolution; the smaller electron beam provides the higher image resolution. After that, the focus distance of the electron beam is adjusted by the objective lens all over the object surface which produces the secondary electron. The signal of the second electron is recorded, turned into electronic signal and presented as an image on the monitor, respectively. The diagram and principle of SEM can be briefly presented as in Figure 12.
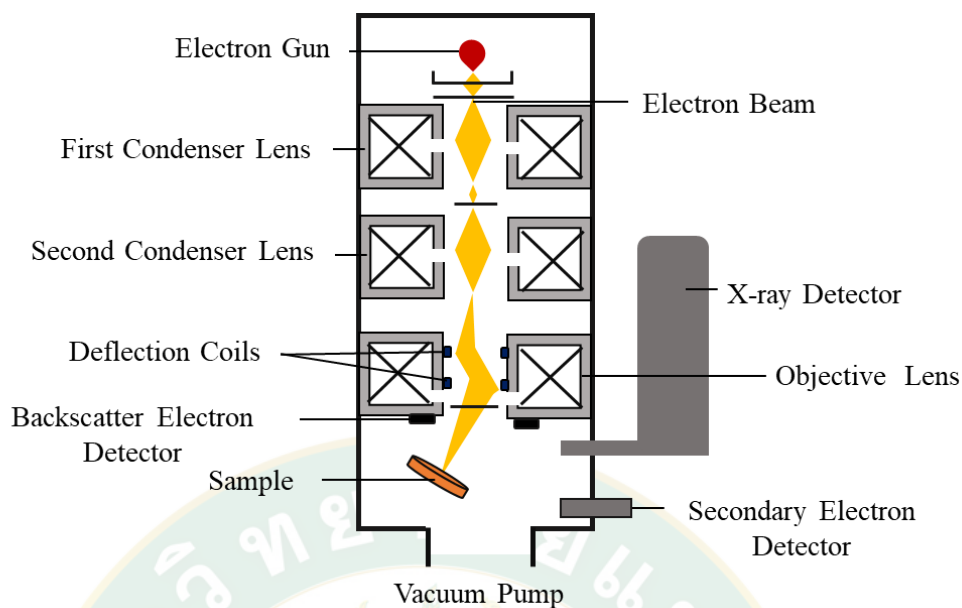
Figure 12 SEM diagram.

2.7 Electrochemical Impedance Spectroscopy (EIS)

Electrochemical Impedance Spectroscopy (EIS) or AC Impedance is one of electroanalytical techniques which is very useful for study of electrochemical cell's system. Additionally, it has been widely applied in material science such as protective method for battery and fuel cell, analysis of ions' diffusion onto semi-permeable membrane and study of the gap between semiconductors as well.

The principle of AC Impedance is to providing alternating current electricity (AC) in the pattern of Since wave under control of applied potential with low amplitude from 10 to 50 mV and adjustable frequency from 10^{-3} to 10^5 Hz. Firstly, the applied potential is fixed at specific value and then the applied potential is increased with alternating current pattern to the system. After that the current response is detected. This obtained current response can be used for analyzing the impedance of the electrochemical cell system which provides the response information of the target interesting materials in terms of current response, potential response or even other signals.

In general, Impedance study of electric system consists of Potentialstat or Galvanostat, Frequency Response Analyzer (FRA) and electrochemical cell. The

electrochemical cell includes of three basic kinds of electrodes; working electrode (WE), reference electrode (RE) and counter electrode (CE).

Impedance is the resistance of alternating current which the impedance value is provided by applying Ohm's law as the following equation:

$$E = IZ \quad ....(8)$$

Where *E* is the applied potential, *I* is the current and *Z* is impedance or the resistance of alternating current pattern, respectively.

Impedance value is equal to resistance (R) when phase shift of potential (E) and current (I) are equal to zero which is presented Figure 13.
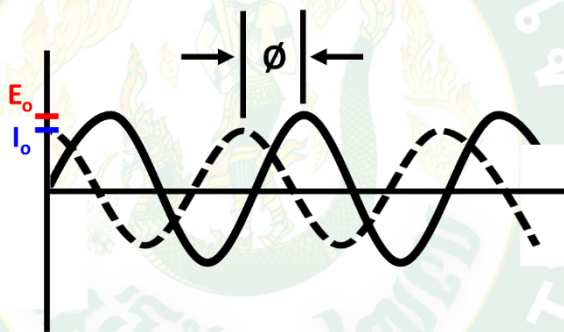
Figure 13 Phase shift of potential (E) and current (I).

Therefore, impedance value based alternating current pattern can be calculated by applying this following equation:

$$Z = \frac{E_0 \sin \omega t}{I_0 \sin(wt + \theta t)} \quad .... (9)$$

Where ω is angular frequency per second equal to $2\pi f$, *f* is frequency (Hz), θ is phase shift (Radien).

Impedance consists of real impedance and imaginary impedance which potential (E) and current (I) are in the same phase of the current called "In Phase". Opposite to imaginary impedance, potential and current are out of phase from the

current. The relation between imaginary impedance (Y-axis) and real impedance (x-axis) provides the Nyquist plot as shown in Figure 14.
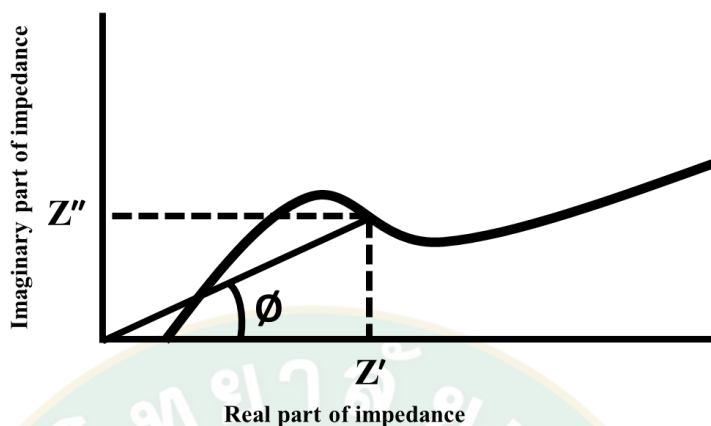
Figure 14 Nyquist plotting between imaginary impedance and real impedance.

From this relation, it can be presented as this following equation:

$$Z = Z' + Z'' \quad ....(10)$$

Where Z is the total of real impedance (Z$'$) and imaginary impedance (Z$''$) and $\tan\theta = \dfrac{Z''}{Z'}$

The obtained impedance value can be turned into the related proper electric circuit which can be used for prediction of the electrode's behavior or property under the optimal condition. From these, the Nyquist plot can provide equivalent circuit.

2.8 Hydrogen peroxide sensor reviews

Throughout the past few decades, the development of devices for hydrogen peroxide (H_2O_2) measurement has been increasingly interesting because hydrogen peroxide plays an important role in environmental, industrial and clinical uses (Chen, J. et al., 2018; Roushani and Dizajdizi, 2015; Zhang and Chen, 2017). Moreover, it is a byproduct of a large number of oxidase enzymes such as glucose oxidase,

cholesterol oxidase, cholinesterase and lactase in biochemical reactions (Kiani Shahvandi et al., 2018; Li et al., 2015; Mutyala and Mathiyarasu, 2016). Accordingly, there is a huge demand and thus multiple attempts to enhance H_2O_2 determination to be rapid, efficient and low-cost. Up to now, various analytical techniques for H_2O_2 detection have been reported such as chemiluminescence (Pourfaraj et al., 2018), chromatography (Gimeno et al., 2015), colorimetry (Zhang et al., 2016), fluorescence (Li, B. et al., 2018), spectrophotometry (Li et al., 2017) and titrimetry (Hurdis and Romeyn, 1954). However, electrochemistry has superior advantages in terms of excellent selectivity, high sensitivity, stability, instrumentation cost, efficiency and ease of operation (Anjum et al., 2015; Qi and Zheng, 2015).

Enzyme-based biosensors have been widely developed and applied, owing to their excellent sensitivity and high selectivity (Boujakhrout et al., 2016; Chen et al., 2016; Sekar et al., 2015), in the last few years. However, the poor intrinsic stability of enzymes significantly affects their biological function and lifetime usage of enzyme-based biosensors (Qin et al., 2015; Yan et al., 2012). In addition, immobilization techniques, denaturation, and storage stability effecting on the biological activity of enzymes restrict their applications (Kogularasu et al., 2017). In order to overcome these issues, the strategy of non-enzymatic or enzyme-free sensors modified various synthesized materials have been challenging and increasingly focused to minimize the drawbacks (Zhou et al., 2018). Recently, metal oxide materials such as Co (Wang, Mei et al., 2015), Ni (Yu et al., 2015), Fe (Lin and Chang, 2015), Cu (Yang et al., 2016) and Mn (Chaisuksant et al., 2016) have been used in sensor applications due to their attractive dominant properties including large surface area, long-term stability, catalytic efficiency and excellent conductivity (Reddy et al., 2017). Also, their metal oxide composite materials outstandingly enhance the electrochemical performances of the sensor (Asif et al., 2017; Wen et al., 2017).

Among various metal oxides, cuprous oxide (Cu_2O), an easily-obtained, intrinsic p-type semiconductor with a band gap of 2.17 eV (Balık et al., 2018; Su et al., 2018), has been extensively used in many applications such as photovoltaic (Wu et al., 2018), photocatalysis and solar cells (Chen, W. et al., 2018). It has also been applied in electrochemical sensing and related fields because of its electrocatalytic activity, low environmental impact and low cost. Unfortunately, these interesting particular properties are limited by its inherent poor conductivity which can affect to the charge transfer of sensor (Yin et al., 2016; Yu et al., 2018). For example, manganese dioxide (MnO_2), an important transition metal oxide, has extensive use as a modified material for batteries, supercapacitors, and sensors (Shu et al., 2017) due to its advantages of excellent catalytic activity, abundant availability, absorption ability, low toxicity and low cost (Li, S.-J. et al., 2018; Luo et al., 2012). However, the challenging issue remains owing to poor conductivity of MnO_2. Thus, for the first time, the novel synergetic $Cu_2O@MnO_2$ composite materials modified GCE surface for enhancement of enzyme-free H_2O_2 sensing was developed as shown in Figure 15. Moreover, the simple and direct drop casting of $Cu_2O@MnO_2$ was presented.
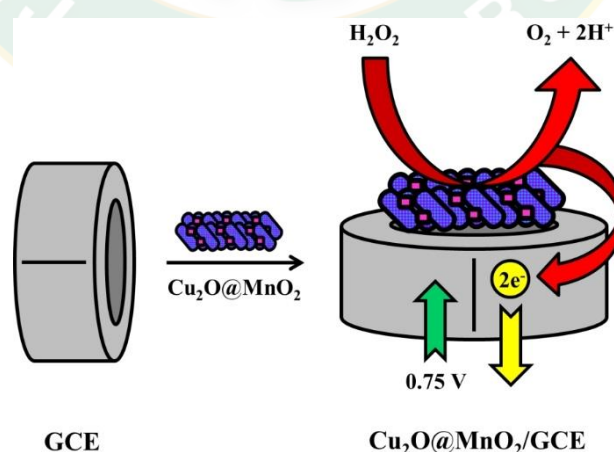
Figure 15 Schematic illustration of the simple step fabrication of enzyme-free H_2O_2 sensor and its proposed electrochemical reaction.

2.9 Choline biosensor reviews

        Choline is an essential nutrient which plays a complex role in the human body (Zeisel and da Costa, 2009) and it is required for many physiological purposes including neurotransmitter synthesis (acetylcholine) , cell-membrane signaling (phospholipids) , lipid transport (lipoproteins) , and methyl-group metabolism (homocysteine reduction) (Penry and Manore, 2008). It is also vital in brain and memory development (Zeisel, 1992; Zeisel, 2004), thus the determination of its level is very important in clinical analysis for early diagnosis of brain-related disorders, such as Alzheimer's (Nitsch et al., 1992), and Parkinson's (Yu et al., 2016) diseases. Different available methods for choline detection were reported, for example, mass spectrometry (Holm et al., 2003)), chromatography (Stadler and Nesselhut, 1986), chemiluminescence (Honda et al., 1986), electrophoresis (Wise et al., 2002), and proton nuclear magnetic resonance spectroscopy (Ackerstaff et al., 2001). Among these various methods, amperometric biosensors hold great promise for many biomedical applications (Wang, 1999) due to its advantages in simplicity, reliability, rapid response, portability, high sensitivity and economic feasibility (Moonla et al., 2017). In order to further develop an efficient choline biosensor, the physical and chemical properties of the modified materials used in their fabrication need to be consider as they exert a significant influence on electroanalytical sensing performance. Many earlier literature have been attempted to enhance choline biosensors with different configurations of carbon nanotubes (Qu et al., 2005), graphene (Deng et al., 2013), nanoparticles (Zhang et al., 2011), conducting polymers (Rahman et al., 2004), redox mediators (Ren et al., 2009) onto the working electrode surface.

        Recently, the proposed biosensors for choline monitoring have been mostly reported based on hydrogen peroxide (H_2O_2) detection, a byproduct from the enzyme-catalyzed reaction of choline oxidase (COx), which then directly reacts with the redox mediator (Bai et al., 2007; Bolat et al., 2017) or it is catalyzed by a second enzyme (horseradish peroxide; HRP) (Wang et al., 2006; Yang, M. et al., 2004), providing a current response signal corresponding to the concentration of the target

analyte. Therefore, the preparation and design of the modified composite material platform with excellent properties including biocompatibility, large surface area for enzyme loading, long-term stability, catalytic efficiency and excellent conductivity in sensor applications are needed to be extensively considered for enhancing the biosensors performances.

Different kinds of metal oxide composite materials such as cuprous oxide (Cu_2O) (Wang, Minghua et al., 2015), manganese dioxide (MnO_2) (Vukojević et al., 2018) and zirconium oxide (ZrO_2) (Yang, Y. et al., 2004) showing very high electrocatalytic activity as redox mediators to promote electron transfer between the biomolecules and the electrode surface has attracted the attention of many researchers. Metal nanoparticles, especially gold nanoparticles (AuNPs), have also been of particular interest in amperometric biosensors as its small size provides catalytic activity, and physical and chemical stability (Wu et al., 2011; Yáñez-Sedeño and Pingarrón, 2005). Up to now, composite materials have been widely used and increasingly playing key roles in the development of biosensors due to their unique physical and chemical properties (Hu et al., 2018; Salehabadi and Enhessari, 2019). One of their major advantages is the enhancement of the dominant inherent property of each comprised material to be such great synergistic redox mediator by adding another suitable combination.

Regarding our previous work, an effort in the enhancement of H_2O_2 determination (Ouiram et al., 2019), the synthesized bimetallic composite materials comprising Cu_2O and MnO_2 modified onto glassy carbon electrode (GCE) surface presented excellent electrochemical and satisfactory kinetic performances resulting from their synergistic interactions. Although an application of MnO_2 in biosensors was limited by its poor conductivity (Song et al., 2019), the interactions of Cu_2O at MnO_2 ($Cu_2O@MnO_2$), as composite material, benefit a redox-mediated behavior while maintaining the advantages of MnO_2 including catalytic activity, abundant availability, absorption ability and low toxicity (Lin et al., 2016; Tizfahm et al., 2016). For the ZrO_2, its forbidden bandgap (Eg = 5.0 eV) (Sinhamahapatra et al., 2016) limits the electrochemical performance which can be improved by fabricating some kinds of interactions between various matrix particles (Wang et al., 2000). This incorporation

indicated that the properties of metal oxides incorporated as composite material platform are influenced by their composition, microstructure, and configuration depending on the designed process.

The aim of our present work was to fabricate an improved amperometric biosensors for an effective quantitative monitoring of choline levels in an electrolyte solution (0.05 M PBS pH 7.8) and in biofluid samples (whole human blood). For this purpose, the performance of the developed $COx/Cu_2O@MnO_2/ZrO_2@AuNPs/GCE$ was comprehensively carried out by applying electrochemical techniques, cyclic voltammetry and amperometry, which significant experimental parameters were optimized for choline detection. This study demonstrated that the immobilized COx onto GCE surface has been synergized by the composite material platform of $Cu_2O@MnO_2/ZrO_2@AuNPs$ for choline analysis, and displayed excellent responses towards the target analyte concentration in human blood samples. The byproduct H_2O_2 was generated by the COx catalyzed reaction in the presence of choline. Then, it was oxidized by the $Cu_2O@MnO_2$ mediator. Meanwhile, the reduced form of the mediator was oxidized at the optimal applied potential. The mechanism of this biosensors is showed in Figure 16 The $ZrO_2@AuNPs$ synergistically enhanced the electron transfer onto the electrode surface and the obtained anodic current response was directly proportional to choline concentration.
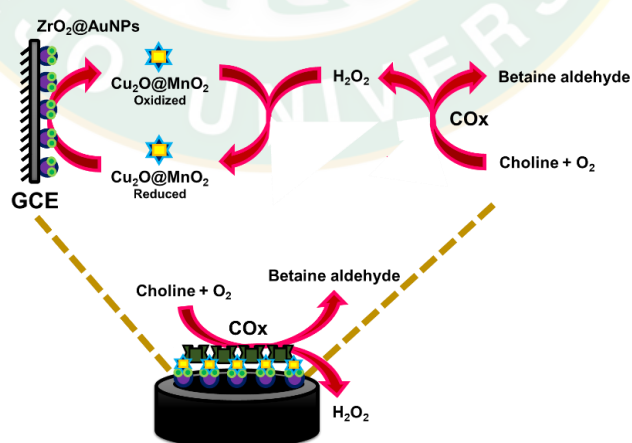
Figure 16 Schematic diagram illustrating the proposed mechanism of choline detection, possible formed enzyme choline oxidase (COx) and synthesized composite materials of $ZrO_2@AuNPs$, and $Cu_2O@MnO_2$ onto the glassy carbon electrode (GCE) surface.

CHAPTER 3

EXPERIMENT

3.1 Chemical reagents

All chemical reagents for solution preparation and material synthesis in this research are shown in Table 3.

Table 3 Chemical reagents used in the research.

No.	Reagent	Purity	Manufacturer	Country
1	Acetic acid (CH_3COOH)	99.7%	Merck	Germany
2	Alumina powder (Al)	99.9%	Sigma aldrich	USA
3	Ascorbic acid (C_8H_8)	99.5%	Sigma aldrich	USA
4	Carbon nanotube	>95%	Sigma aldrich	USA
5	Caffeine ($C_8H_{10}N_4O_2$)	99%	Sigma aldrich	USA
6	Chitosan	>93%	Sigma aldrich	USA
7	Choline chloride (($CH_3)_3N(Cl)CH_2CH_2OH$)	>99%	Sigma aldrich	USA
8	Choline oxidase	-	Sigma aldrich	USA
9	Diethyl ether ($C_4H_{10}O$)	99.5%	Sigma aldrich	USA
10	Ethanol (CH_3CH_2OH)	99.5%	Merck	USA
11	Glucose ($C_6H_{12}O_6$)	96%	Ajax Finechem	Australia
12	Glutaraldehyde ($C_5H_8O_2$)	50%	Sigma aldrich	USA
13	Gold (III) chloride trihydrate ($HAuCl_4$)	49%	Sigma aldrich	USA
14	Hydrogen peroxide (H_2O_2)	30%	Merck	Germany
15	Nitric acid (HNO_3)	65%	Sigma Aldrich	USA
16	Oxalic Acid ($H_2C_2O_4$)	99.5%	Ajax Chemical	Australia
17	Potassium chloride (KCl)	99.5%	Ajax Chemical	Australia
18	Potassium hydrogen phosphate	>99%	Sigma Aldrich	USA

Table 3 Chemical reagents used in the research (continued).

No.	Reagent	Purity	Manufacturer	Country
19	Potassium nitrate (KNO_3)	99%	Sigma Aldrich	USA
20	Potassium dihydrogen orthophosphate (KH_2PO_4)	99.5%	Ajax Chemical	Australia
21	Sodium chloride (NaCl)	99%	Ajax Chemical	Australia
22	Sodium hydroxide (NaOH)	97%	Ajax Chemical	Australia
23	Thionin acetate ($C_{12}H_9N_3S$ $C_2H_4O_2$)	95%	Sigma Aldrich	USA
24	Uric acid ($C_5H_4N_4O_3$)	99%	Sigma Aldrich	USA
25	Zirconium(IV) oxide-yttria stabilized	99.9%	Sigma Aldrich	USA

3.2 Instruments

All instruments used in the research are listed in Table 4.

Table 4 Instruments

No.	Instrument	Manufacturer	Country
1	WE; glassy carbon electrode	CH Instruments/⌀ 3 mm	USA
2	CE; platinum wire	CH Instruments/⌀ 3 mm	USA
3	RE; Ag/AgCl	CH Instruments/ 3 M KCl	USA
4	Analytical balance	Mettler Toledo	Switzerland
5	pH meter	Metrohm/pH lab 827	Switzerland
6	Potentiostat	CHInstruments/ CH1230A	USA
7	Ultrasonic instrument	Labquip	England
8	Sputter coater	Jeol/JFC1200	Japan
9	Anodisc membrane ⌀ 0.02 μm	Whatman	Germany
10	Electrochemical Cell	Home-made, 5 mL	Thailand

3.3 Hydrogen peroxide sensor

3.3.1 Preparation of each solution in the research

Preparation of 0.5% chitosan solution (0.5% CHIT)

0.50 g chitosan powder was dissolved and then slowly dropped concentrated acetic acid into the solution until pH value of the solution was about 4-5. After that, the volume of solution was adjusted as 100 mL. Finally, the obtained 0.5% CHIT solution was kept in the refrigerator at 4 $^{\circ}$C for further use.

Preparation of 0.1 M phosphate buffer solution pH 7.2

1.0 M Potassium hydrogen phosphate: K_2HPO_4 (Solution A)

43.55xx g potassium hydrogen phosphate was dissolved by deionized water and then adjusted the volume as 250.00 mL.

1.0 M Potassium dihydrogen phosphate: KH_2PO_4 (Solution B)

34.02xx g potassium dihydrogen phosphate was dissolved by deionized water and then adjusted the volume as 250.00 mL.

35.8 mL of the solution A was mixed with 14.20 mL of the solution B into 500.00 mL volumetric flask and then adjusted the volume by deionized water to obtain 0.1 M phosphate buffer solution pH 7.2.

Preparation of interfering solution

0.1 M phosphate buffer solution pH 7.2 was used as a solvent for preparation of interfering solutions including of 250 mg mL^{-1} ascorbic acid, 99.9% ethanol, 500 mg mL^{-1} glucose, 200 mg mL^{-1} sucrose and 0.06 mg mL^{-1} uric acid.

Synthesis of $Cu_2O@MnO_2$

The $Cu_2O@MnO_2$ composite materials was synthesized using the single-step reflux method which was adjusted from the earlier report (Chen et al., 2015). First, a 0.32 M $KMnO_4$ solution was prepared and then $CuSO_4·5H_2O$ was added into 100 mL of the 0.32 M $KMnO_4$ solution (stoichiometric ratio of Cu:Mn as 1:5) – Solution A. After that, 50 mL of a 0.88 M $MnSO_4$ solution was prepared and then 8.5 mL HNO_3 was added – Solution B. Solution B was added drop-wise into Solution A under continuous stirring. This resulted in dark precipitate formation. The resultant slurry was refluxed at 120 degrees Celsius for 12 hours, washed and dried at 120 degrees

Celsius for 12 hours, respectively. Finally, the obtained $Cu_2O@MnO_2$ powder was kept in a desiccator at room temperature for the further work. The MnO_2 powder was also synthesized, without adding $CuSO_4 \cdot 5H_2O$ into solution A, using the same method of $Cu_2O@MnO_2$ synthesis. The synthesized material was characterized by using SEM, EDX, FTIR and XRD, respectively. Ultimately, it was kept in desiccator for further applications in this work.

3.3.2 Preparation of the modified electrodes

Preparation : Cleaning of bare GCE

For the preparation of the bare electrode, it is rubbed by alumina powder, washed with DI water, sonicated for 5 minutes, dipped into HNO_3 solution for a while and dried at room temperature before use in Figure 17.

Figure 17 Cleaning of glassy carbon electrode surface.

Preparation : CHIT-MnO$_2$/GCE

For the preparation of the CHIT-MnO$_2$/GCE, it can be prepared by dropping the prepared MnO_2 mixed 0.5% chitosan solution onto the electrode surface. Leave it dried at room temperature before use in Figure 18.
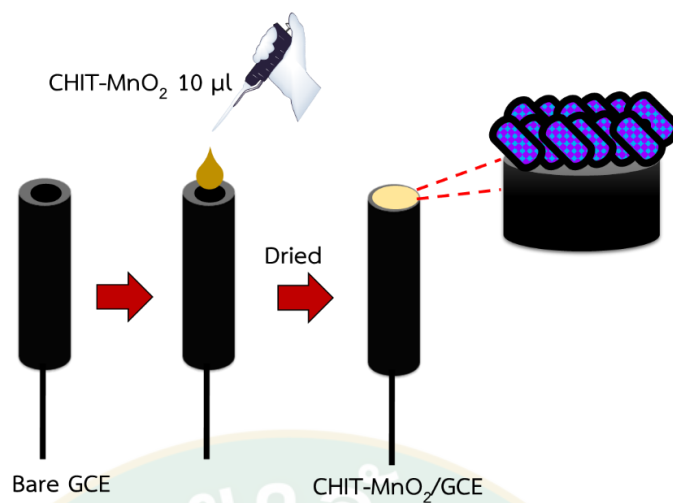
Figure 18 Preparation of the CHIT-MnO$_2$/GCE.

Preparation : CHIT- Cu$_2$O@MnO$_2$ /GCE

For the preparation of the CHIT-Cu$_2$O@MnO$_2$/GCE, it can be prepared by dropping the prepared Cu$_2$@MnO$_2$ mixed 0.5% chitosan solution onto the electrode surface. Leave it dried at room temperature before use in Figure 19.
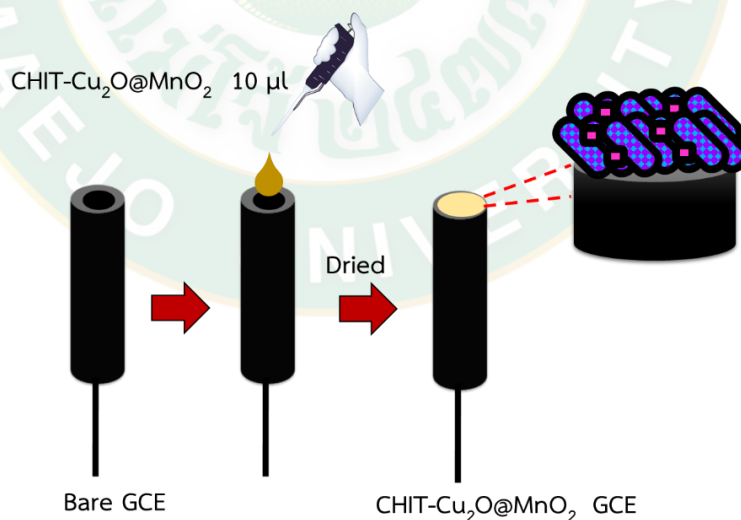
Figure 19 Preparation of the CHIT- Cu$_2$O@MnO$_2$ /GCE.

All of each different modified electrode was tested using cyclic voltammetry in the potential range from 0.0 to 1.0 V in 0.1 M phosphate buffer solution pH 7.2

and in 0.1 M phosphate buffer solution pH 7.2 containing 0.5 mM H_2O_2, respectively, for studying of the electrochemical reaction onto the electrode surface as presented in Figure 20. Moreover, each modified electrode was studied the resistance onto its surface by applying electrochemical impedance spectroscopy (EIS).
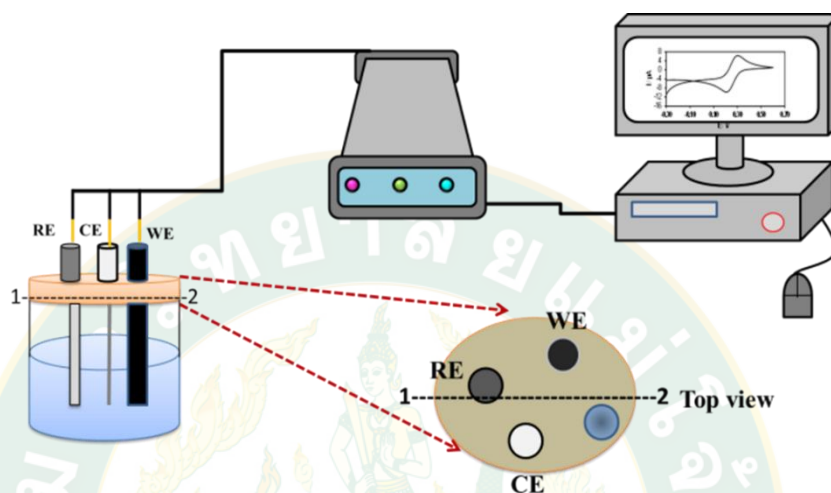
Figure 20 Chemical cells for cyclic voltammetric study.

To study the optimal condition and the property of each modified electrode, an amperometric technique was applied under stirring condition which the arrangement of chemical cells was illustrated in Figure 21.
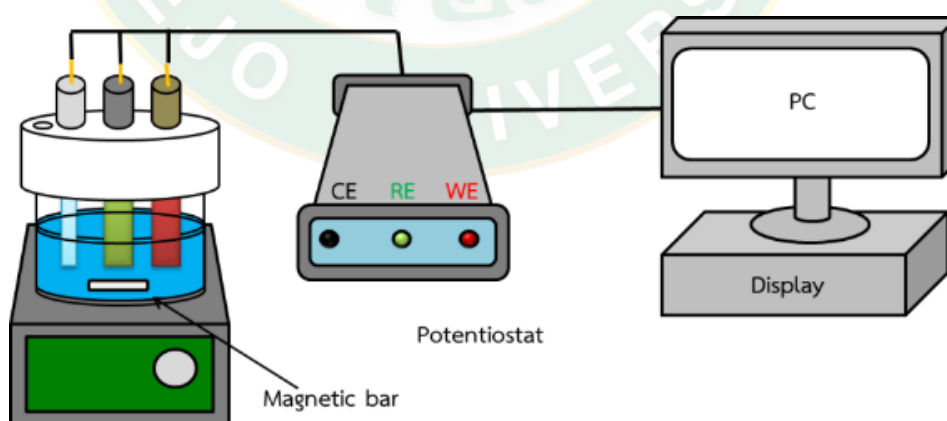
Figure 21 Electrochemical cells for amperometric study.

3.3.3 Applied potential

To obtain the applied potential for oxidation reaction of H_2O_2, the CHIT-$Cu_2O@MnO_2$/GCE was tested in 0.1 M phosphate buffer solution pH 7.2 by spiking 0.5 mM H_2O_2 standard solution with applying amperometry at various potential values from 0.6 to 0.9 V (0.05 V increment). The applied potential value which provided the highest current response will be chosen for further experiment.

3.3.4 pH effect of electrolyte solution

To obtain the proper pH value, the CHIT-$Cu_2O@MnO_2$/GCE was operated in 0.1 M phosphate buffer solution by spiking 0.5 mM H_2O_2 standard solution with applying amperometry at various pH values including of 6.0, 6.2, 6.4, 6.6, 6.8, 7.0, 7.2, 7.4, 7.6, 7.8 and 8.0, respectively. The pH value of the electrolyte solution which provided the highest current response will be selected for next step.

3.3.5 Effect of $Cu_2O@MnO_2$ content

To obtain suitable concentration of $Cu_2O@MnO_2$ modified onto the electrode surface, each CHIT-$Cu_2O@MnO_2$/GCE with different $Cu_2O@MnO_2$ including of 0, 1, 2, 3, 4, 5, 6 and 7 mg ml^{-1}, respectively, was tested in 0.1 M phosphate buffer solution by spiking 0.5 mM H_2O_2 standard solution with applying amperometry. The concentration of $Cu_2O@MnO_2$ modified onto the electrode surface which provided the highest current response will be selected for the further work.

3.3.6 Linearity and Limit of Detection

The CHIT-$Cu_2O@MnO_2$/GCE was tested in 0.1 M phosphate buffer solution by spiking 0.5, 1, 2, 5, 10, 20, 50, 100, 200, 500, 1000, 2000, 5000, 10000 and 20000 µM H_2O_2 standard solution, respectively, with applying amperometry. Then, the obtained current response (y-axis) was plotted versus each H_2O_2 concentration (x-axis) which can be used for calculation of limit of detection (Signal to Noise = 3).

3.3.7 Repeatability

The CHIT-Cu$_2$O@MnO$_2$/GCE was repetitively operated in 0.1 M phosphate buffer solution by spiking 5.0 mM H$_2$O$_2$ standard solution with applying amperometry for 7 times at the same electrod for assessment the precision of this biosensor.

3.3.8 Reproducibility

Each CHIT-Cu$_2$O@MnO$_2$/GCE was operated in 0.1 M phosphate buffer solution by spiking 0.5 mM H$_2$O$_2$ standard solution with applying amperometry for 7 fresh electrodes to evaluate the reproducibility of the method.

3.3.9 Operation time

The CHIT-Cu$_2$O@MnO$_2$/GCE was repetitively operated in 0.1 M phosphate buffer solution by spiking 5.0 mM H$_2$O$_2$ standard solution with applying amperometry until the obtained current response was lower than 50% of the first detected current response to determine operation time.

3.3.10 Effect of Interferences

The CHIT-Cu$_2$O@MnO$_2$/GCE was operated in 0.1 M phosphate buffer solution by spiking 0.5 mM H$_2$O$_2$ standard solution and then followed by spiking various possible interfering species including of ascorbic acid, ethanol, glucose, sucrose and uric acid with applying amperometry.

3.3.11 Sample analysis

The standard solution (0, 50 and 500 µM, 0.5 mL) was prepared by using Standard addition method. Then, each prepared standard solution was added 0.5 mL of the target sample.

0.5 mL of 250 µM H$_2$O$_2$ was added into 0.5 mL of the target sample for calculation of % recovery.

The CHIT-Cu$_2$O@MnO$_2$/GCE was applied to detect H$_2$O$_2$ concentration in different 6 samples with applying amperometry in 0.1 M phosphate buffer solution pH 7.2, 5 mL. Each 10 µL of each prepared sample was added in to the chemical cell

to obtain the current response resulting from H_2O_2 oxidation reaction onto the working electrode surface. After that, the obtained current response (y-axis) was plotted versus each added H_2O_2 concentration (x-axis) which can be used for calculation of H_2O_2 concentration in each sample and also % recovery.

3.4 Choline biosensor

3.4.1 Preparation of each solution in the research

Preparation of 0.1 M phosphate buffer solution pH 7.8

1.0 M Potassium hydrogen phosphate: K_2HPO_4 (Solution A)

43.55 g potassium hydrogen phosphate was dissolved by deionized water and then adjusted the volume as 250.00 mL.

1.0 M Potassium dihydrogen phosphate: KH_2PO_4 (Solution B)

34.02 g potassium dihydrogen phosphate was dissolved by deionized water and then adjusted the volume as 250.00 mL.

40.00 mL of the solution A was mixed with 10.00 mL of the solution B into 500.00 mL volumetric flask and then adjusted the volume by deionized water to obtain 0.1 M phosphate buffer solution pH 7.8.

Preparation of interfering solution

0.1 M phosphate buffer solution pH 7.8 was used as a solvent for preparation of interfering solutions including of 100 mg mL^{-1} amoxicillin, 300 mg mL^{-1} ascorbic acid, 100 mg mL^{-1} aspirin, 15 mg mL^{-1} caffeine, 19 mg mL^{-1} dopamine, 100 mg mL^{-1} glucose, 100 mg mL^{-1} sucrose and 60 mg mL^{-1} uric acid.

For 0.5% CHIT and synthesis of $Cu_2O@MnO_2$ were discussed in 3.3.1.

3.4.2 Preparation of the modified electrodes

Preparation : Cleaning of bare GCE

For the preparation of the bare electrode, it is rubbed by alumina powder, washed with DI water, sonicated for 5 minutes, dipped into HNO_3 solution for a while and dried at room temperature before use in Figure 22.
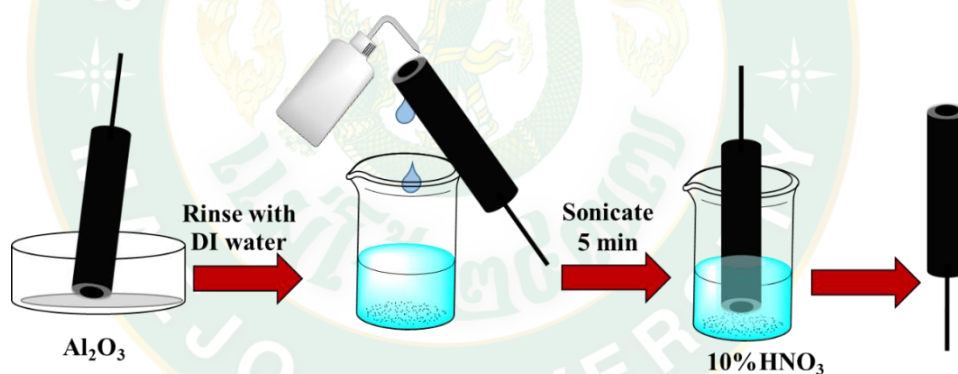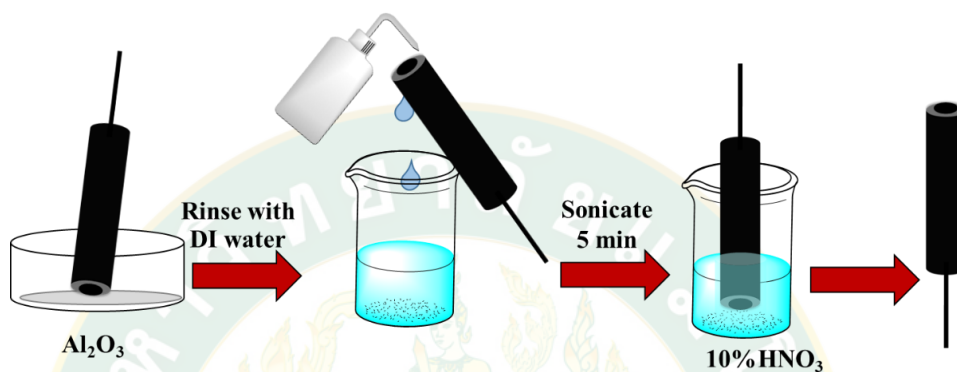

Figure 22 Cleaning of glassy carbon electrode surface.

Preparation : COx/CHIT/GCE

For the preparation of the COx-chit/GCE, it can be prepared by dropping the 0.5% chitosan solution onto the electrode surface and follow by dropping COx solution. Leave it dried at room temperature before use in Figure 23.
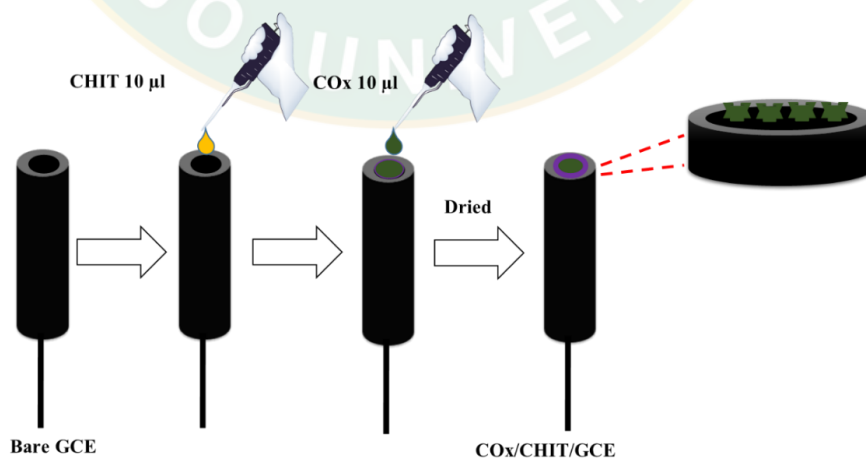
Figure 23 Preparation of the COx-CHIT/GCE.

Preparation : COx/CHIT-ZrO$_2$@AuNPs/GCE

For the preparation of the Cox/ZrO$_2$@AuNPs-Chit/GCE, it can be prepared by dropping the ZrO$_2$@AuNPs mixed 0.5% chitosan solution onto the electrode surface and follow by dropping COx solution. Leave it dried at room temperature before use in Figure 24.
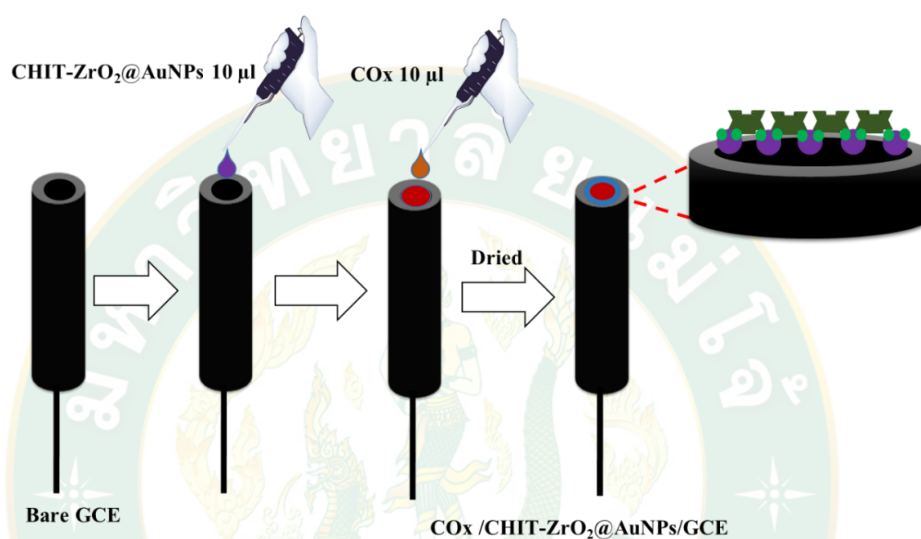
Figure 24 Preparation of the COx/CHIT-ZrO$_2$@AuNPs/GCE.

Preparation : COx/CHIT-Cu$_2$O@MnO$_2$/GCE

For the preparation of the Cox/Cu2O@MnO2-Chit/GCE, it can be prepared by dropping the Cu$_2$O@MnO$_2$ mixed 0.5% chitosan solution onto the electrode surface and follow by dropping COx solution. Leave it dried at room temperature before use in Figure 25.
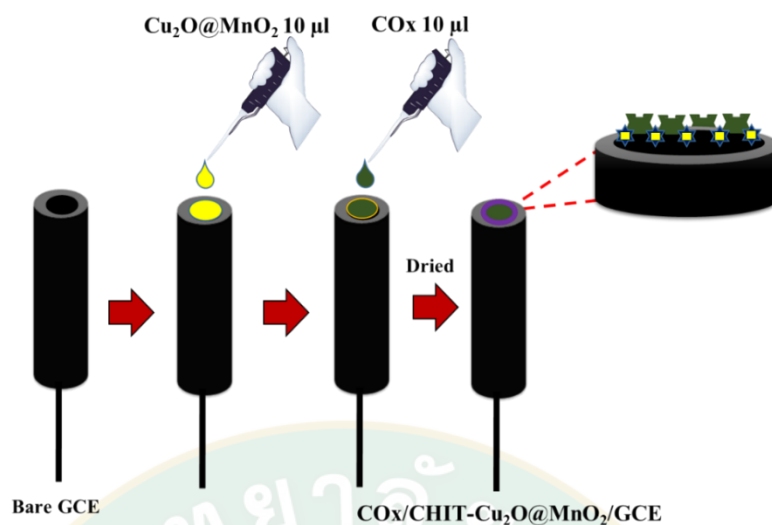
Figure 25 Preparation of the COx/CHIT-Cu$_2$O@MnO$_2$/GCE.

Preparation : COx/Cu$_2$O@MnO$_2$/CHIT-ZrO$_2$@AuNPs/GCE

For the preparation of the COx/Cu$_2$O@MnO$_2$-Chit-ZrO$_2$@AuNPs/GCE, it can be prepared by dropping ZrO$_2$@AuNPs mixed 0.5% chitosan solution onto the electrode surface and follow by dropping the Cu$_2$O@MnO$_2$ mixed 0.5% chitosan solution and COx solution, respectively. Leave it dried at room temperature before use in Figure 26.
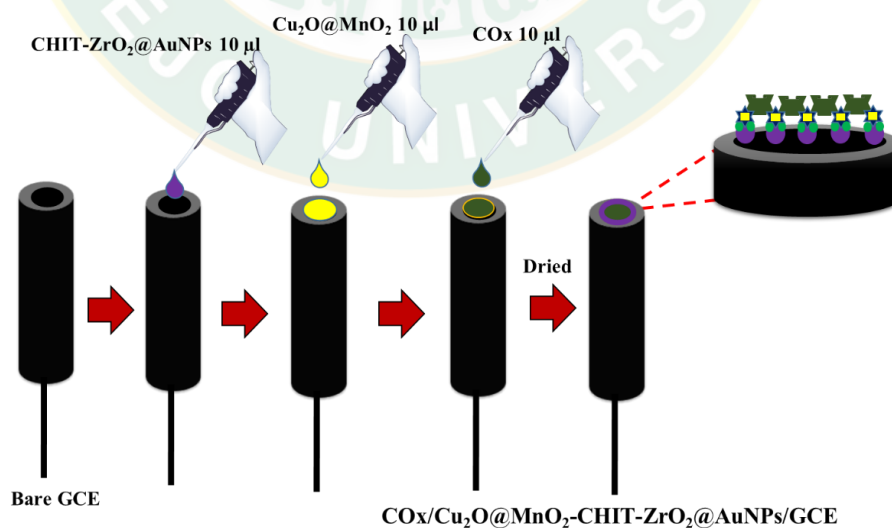
Figure 26 Preparation of the COx/Cu$_2$O@MnO$_2$/CHIT-ZrO$_2$@AuNPs/GCE.

All four different modified electrodes were tested by using cyclic voltammetry in the potential range from 0.0 to 1.0 V in 0.1 M phosphate buffer solution pH 7.8 and in 0.1 M phosphate buffer solution pH 7.2 containing 1.0 and 2.5 mM H_2O_2, respectively, for study of the electrochemical reaction onto the electrode surface. Furthermore, each modified electrode was studied the resistance onto its surface by applying electrochemical impedance spectroscopy (EIS).

3.4.3 Applied potential

To obtain the applied potential, the $COx/Cu_2O@MnO_2$-CHIT-$ZrO_2@AuNPs/GCE$ was tested in 0.1 M phosphate buffer solution pH 7.8 by spiking 2.5 mM choline standard solution with applying amperometry at various potential values from 0.65 to 0.9 V (0.05 V increment). The applied potential value which provided the highest current response will be chosen for further experiment.

3.4.4 pH effect of electrolyte solution

To obtain the proper pH value, the $COx/Cu_2O@MnO_2$-CHIT-$ZrO_2@AuNPs/GCE$ was operated in 0.1 M phosphate buffer solution by spiking 0.25 mM choline standard solution with applying amperometry at various pH values including of 6.8, 7.0, 7.2, 7.4, 7.6, 7.8 and 8.0, respectively. The pH value of the electrolyte solution which provided the highest current response will be selected for next step.

3.4.5 Temperature effect

To obtain suitable temperature for the experiment, the $COx/Cu_2O@MnO_2$-CHIT-$ZrO_2@AuNPs/GCE$ was operated in 0.1 M phosphate buffer solution pH 7.8 by spiking 0.25 mM choline standard solution with applying amperometry at various temperatures including of 30, 35, 40, 45 and 50 $^\circ$C, respectively. The temperature which provided the highest current response will be selected for next step.

3.4.6 Effect of enzyme content

To obtain proper content of choline oxidase immobilized onto the electrode surface, Each $COx/Cu_2O@MnO_2$-CHIT-$ZrO_2@AuNPs$/GCE with different content of choline oxidase including of 0 .2, 0.5, 1.0, 1.5, 2.0 and 2.5 Unit, respectively, was tested in 0.1 M phosphate buffer solution pH 7.8 by spiking 0.25 mM choline standard solution with applying amperometry. The content of choline oxidase immobilized onto the electrode surface which provided the highest current response will be selected for the further work.

3.4.7 Effect of $ZrO_2@AuNPs$ concentration

To obtain proper concentration of $ZrO_2@AuNPs$ modified onto the electrode surface, Each $COx/Cu_2O@MnO_2$-CHIT-$ZrO_2@AuNPs$/GCE with different concentration of $ZrO_2@AuNPs$ including of 0, 1, 5, 10, 20, 30 and 40 mg mL^{-1}, respectively, was tested in 0.1 M phosphate buffer solution pH 7.8 by spiking 0.25 mM choline standard solution with applying amperometry. The concentration of $ZrO_2@AuNPs$ modified onto the electrode surface which provided the highest current response will be chosen.

3.4.8 Effect of $Cu_2O@MnO_2$ concentration

To obtain proper concentration of $Cu_2O@MnO_2$ modified onto the electrode surface, Each $COx/Cu_2O@MnO_2$-CHIT-$ZrO_2@AuNPs$/GCE with different concentration of $Cu_2O@MnO_2$ including of 0 , 1.0, 2.5 , 5.0 , 10.0, 15.0 and 20.0 mg mL^{-1}, respectively, was tested in 0.1 M phosphate buffer solution pH 7.8 by spiking 0.25 mM choline standard solution with applying amperometry. The concentration of $Cu_2O@MnO_2$ modified onto the electrode surface which provided the highest current response will be applied for the next step.

3.4.9 Linearity and Limit of Detection

The COx/Cu$_2$O@MnO$_2$-CHIT-ZrO$_2$@AuNPs/GCE was tested in 0.1 M phosphate buffer solution pH 7.8 by spiking 0.5, 1.0, 2.5, 5.0, 10, 25, 50, 100, 250, 500 and 1000 μM choline standard solution, respectively, with applying amperometry. Then, the obtained current response (y-axis) was plotted versus each choline concentration (x-axis) which can be used for calculation of limit of detection (Signal to Noise = 3).

3.4.10 Repeatability

The COx/Cu$_2$O@MnO$_2$-CHIT-ZrO$_2$@AuNPs/GCE was repetitively operated in 0.1 M phosphate buffer solution pH 7.8 by spiking 0.1 mM choline standard solution with applying amperometry for 5 times to determine the stability of each obtained current response.

3.4.11 Reproducibility

Each COx/Cu$_2$O@MnO$_2$-CHIT-ZrO$_2$@AuNPs/GCE was operated in 0.1 M phosphate buffer solution pH 7.8 by spiking 0.25 mM choline standard solution with applying amperometry for 5 electrodes to evaluate the reproducibility of the method.

3.4.12 Operation time

The COx/Cu$_2$O@MnO$_2$-CHIT-ZrO$_2$@AuNPs/GCE was repetitively operated in 0.1 M phosphate buffer solution pH 7.8 by spiking 0.1 mM choline standard solution with applying amperometry until the obtained current response was lower than 50% of the first detected current response to determine the stability of each modified material onto the working electrode surface.

3.4.13 Effect of interferences

The COx/Cu$_2$O@MnO$_2$-CHIT-ZrO$_2$@AuNPs/GCE was operated in 0.1 M phosphate buffer solution pH 7.8 by spiking 0.1 mM choline standard solution and then followed by spiking various possible interfering species including of amoxicillin,

ascorbic acid, aspirin, caffeine, dopamine, glucose, sucrose and uric acid with applying amperometry.

3.4.14 Choline analysis in real whole blood samples

The standard solution (0, 50, 125 and 250 µM, 0.5 mL) was prepared using Standard addition method. Then, each prepared standard solution was added 0.5 mL of real whole blood sample.

0.5 mL of 150 µM choline was added into 0.5 mL of real whole blood sample for calculation of % recovery.

The COx/Cu$_2$O@MnO$_2$-CHIT-ZrO$_2$@AuNPs/GCE was applied to determine choline concentration in different 6 real whole blood samples supported by Sansai hospital, Chiang Mai, Thailand with applying amperometry in 0.1 M phosphate buffer solution pH 7.8, 5 mL. Each 10 µL of each prepared sample was added in to the chemical cell to obtain the current response resulting from byproduct H$_2$O$_2$ oxidation reaction in the system onto the working electrode surface. After that, the obtained current response (y-axis) was plotted versus each added choline concentration (x-axis) which can be used for calculation of choline concentration in each sample and also % recovery.

CHAPTER 4

RESULTS AND DISCUSSION

4.1 Hydrogen peroxide sensor

4.1.1 Characterization of synthesized materials

To characterize and confirm the synthesized materials, MnO_2 and $Cu_2O@MnO_2$ were studied and compared using various techniques. Figure 27 A(a) and 27B(a) showed the SEM images of MnO_2 and $Cu_2O@MnO_2$, respectively. The MnO_2 showed rod shape with a diameter of 2 μm while the $Cu_2O@MnO_2$ showed the mixture of the rod (diameter 1 μm) and flake (wide 5 μm) shapes. Also, the difference between MnO_2 and $Cu_2O@MnO_2$ and their qualitative compositions were confirmed with the presence of elements such as manganese, potassium, and oxygen from MnO_2 EDX pattern (Figure 27 A(b)) while the copper was additional added in $Cu_2O@MnO_2$ (Figure 27 B (b)).

Additionally, XRD patterns (Figure 27 C) presented structural and morphological features as the crystalline natures of MnO_2 and $Cu_2O@MnO_2$. The XRD pattern of MnO_2 was indexed as (110), (101), (200), (111), (210), (211), (220), (002), (310), (221) and (301) planes of tetragonal MnO_2 crystal system (JCPDS no. 01-081-2261). Compared to the synthesized $Cu_2O@MnO_2$, the presence of cubic Cu_2O crystal phase of the composite materials was confirmed corresponding to the planes (110), (111), (200), (220) and (311) (JCPDS no. 00-034-1354). The FTIR result of MnO_2 and $Cu_2O@MnO_2$ were shown in Figure 27 D. The bands of the MnO_2 spectrum at 568 and 428 cm^{-1} could be attributed to Mn–O and Mn–O–Mn lattice vibration, respectively. Compared to $Cu_2O@MnO_2$, the bands of the spectrum at 686, 584 and 420 cm^{-1} corresponded to Cu (I)–O, Mn–O and Mn–O–Mn, respectively, which was in good agreement with previous reports.
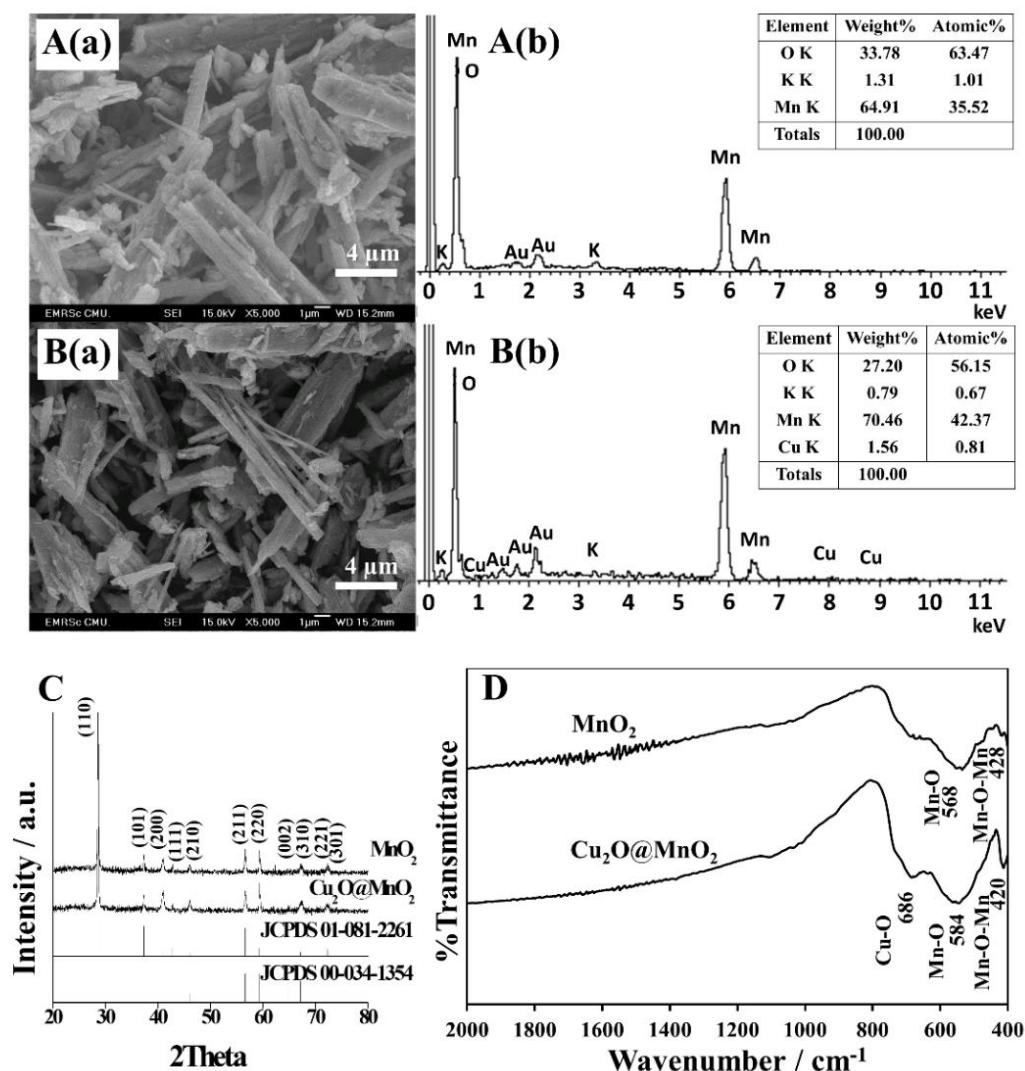
Figure 27 SEM images (A(a), B(a)) and EDX spectra (A(b), B(b)), XRD patterns (C) and FTIR spectra (D) of synthesized materials MnO_2 compared to $Cu_2O@MnO_2$.

4.1.2 Cyclic voltammetric study

The bare GCE

The bare GCE was operated in 0.1 M phosphate buffer solution pH 7.2 (a) compared to the presence of 0.5 mM H_2O_2 (b) using cyclic voltammetry. The results showed the obtained cyclic voltammograms which there is no difference both absence and presence of H_2O_2 as presented in Figure 28. This suggested that the bare GCE without the modification of its own surface has clearly limited ability for H_2O_2 sensing.
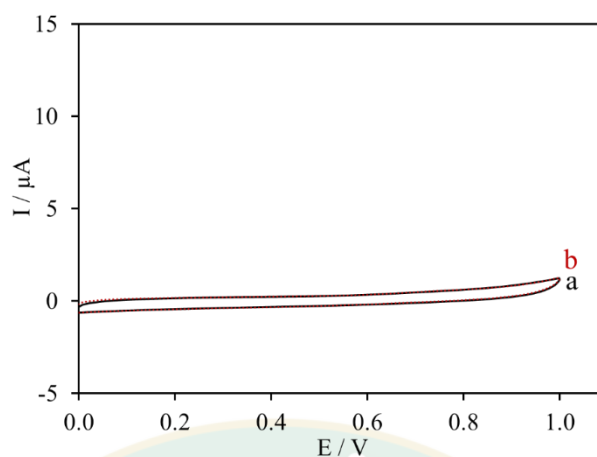
Figure 28 Cyclic voltammograms of the bare GCE in 0.1 M phosphate buffer solution pH 7.2 containing 0 mM (a) and 0.5 mM (b) H_2O_2.

The CHIT-MnO$_2$/GCE

In Figure 29, the CHIT-MnO$_2$/GCE was operated in 0.1 M phosphate buffer solution pH 7.2 (a) compared to the presence of 0.5 mM H_2O_2 (b) by using cyclic voltammetry. The results showed the obtained cyclic voltammograms which the curve of H_2O_2 oxidation reaction (b) obviously noticed from 0.7 to 1.0 V compared to the blank solution (a). This suggested that CHIT-MnO$_2$ modified onto GCE enhanced the electron transfer process onto the electrode surface for H_2O_2 sensing.
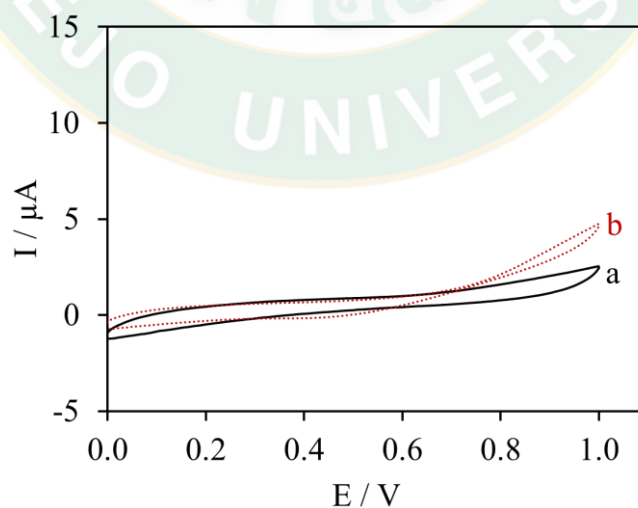
Figure 29 Cyclic voltammograms of the CHIT-MnO$_2$/GCE in 0.1 M phosphate buffer solution pH 7.2 containing 0 mM (a) and 0.5 mM (b) H_2O_2.

The CHIT- $Cu_2O@MnO_2$ /GCE

The CHIT- $Cu_2O@MnO_2$/GCE was operated in 0.1 M phosphate buffer solution pH 7.2 (a) compared to the presence of 0.5 mM H_2O_2 (b) by using cyclic voltammetry as shown in Figure 30. The results showed the obtained cyclic voltammograms which the curve of H_2O_2 oxidation reaction (b) obviously increased from 0.6 to 1.0 V compared to the blank solution (a). Additionally, the obtained current response was very high with about 12 times of the bare GCE signal from the electro-mediator behavior of synthesized $Cu_2O@MnO_2$ onto the working electrode surface. This indicated that CHIT- $Cu_2O@MnO_2$ modified onto GCE effectively enhanced the electron transfer process onto the electrode surface and provided the possibility to detect H_2O_2 concentration at lower level.
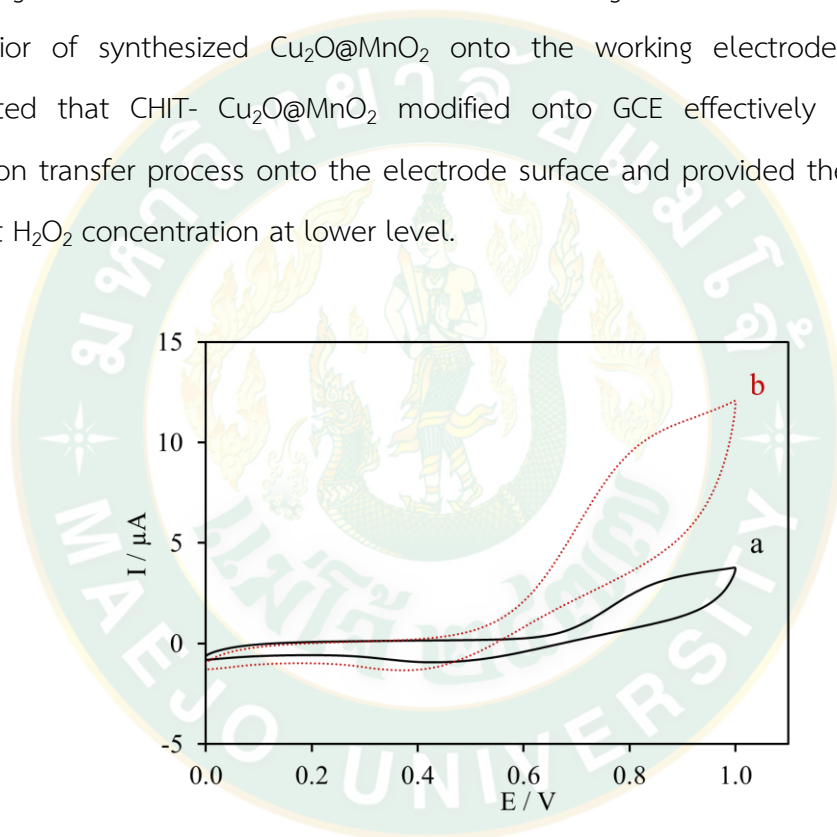
Figure 30 Cyclic voltammograms of the CHIT-$Cu_2O@MnO_2$/GCE in 0.1 M phosphate buffer solution pH 7.2 containing 0 mM (a) and 0.5 mM (b) H_2O_2.

Therefore, the CHIT- $Cu_2O@MnO_2$/GCE was selected for the further work which then was operated in 0.1 M phosphate buffer solution pH 7.2 containing 0.0, 1.0, 1.5 and 2.0 mM H_2O_2, respectively, by using cyclic voltammetry from 0.0 to 1.0 V at 50 mVs^{-1} as presented in Figure 31. The results showed that the current response of H_2O_2 oxidation reaction curve at 0.8 V clearly increased with respect to higher

H_2O_2 concentrations. This suggested that this method can be applied for H_2O_2 quantitative analysis.
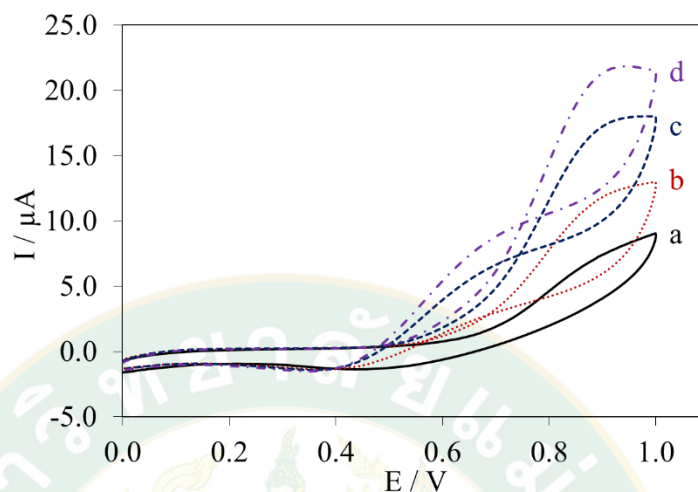
Figure 31 Cyclic voltammograms of the CHIT- $Cu_2O@MnO_2$/GCE in 0.1 M phosphate

buffer solution pH 7.2 containing 0.0 (a), 1.0 (b), 1.5 (c) and 2.0 mM (d) H_2O_2 at

50 mVs^{-1} scan rate.

Following to cyclic votammetric study of each different modified electrode compared to the bare GCE, it was obvious that synthesized $Cu_2O@MnO_2$ of the CHIT-$Cu_2O@MnO_2$/GCE enhanced H_2O_2 oxidation reaction and electrons transfer process onto the working electrode surface which is 3 times higher than CHIT-MnO_2/GCE and 12 times higher than the bare GCE. The mechanism of this method can be briefly discussed in few steps. Firstly, the working electrode in the system was applied potential from a potentiostat instrument. After that, H_2O_2 oxidation reaction occured and provided electrons to the working electrode surface resulting in electron flow in the area which the synthesized $Cu_2O@MnO_2$ onto the electrode surface acted as an electro-mediator as illustrated in Figure 32.
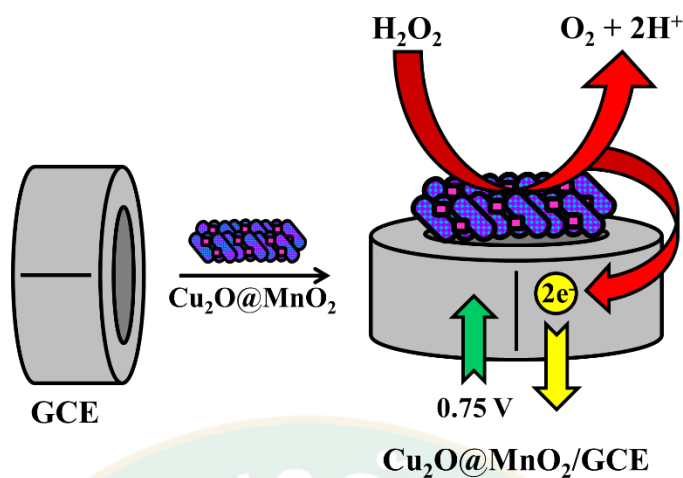
Figure 32 Schematic illustration of the simple step fabrication of enzyme-free H_2O_2 sensor and its proposed electrochemical reaction.

In order to study its electrochemical behavior and explain its kinetics, the $Cu_2O@MnO_2$/GCE was also operated in the 2 mM $K_3Fe(CN)_6$ containing 0.1 M KCl at various scan rates in the range of 25 to 150 mV s^{-1} as shown in the cyclic voltammograms in Figure 33. Following the obtained linear relationships between peak current responses and the square root of the scan rates as shown in the inset of Figure 33 it was provided a diffusion controlled quasi-reversible process of associated redox processes. Moreover, the kinetic parameters such as charge transfer rate constant (K_s), diffusion coefficient value (D), electroactive surface area (A_e) and surface concentration (γ) can be calculated as 0.56 s^{-1}, 1.65 x 10^{-5} cm^2 s^{-1}, 0.12 mm^2 and 1.04 x 10^{-8} mol cm^{-2}, respectively. K_s value was calculated using the Laviron equation, D and A_e values obtained by Randles-Sevcik equations (Çelik Kazıcı et al., 2018; Moonla et al., 2017)(Çelik Kazıcı et al., 2018; Moonla et al., 2017)(Çelik Kazıcı et al., 2018; Moonla et al., 2017) while γ gained using Brown - Anson model.
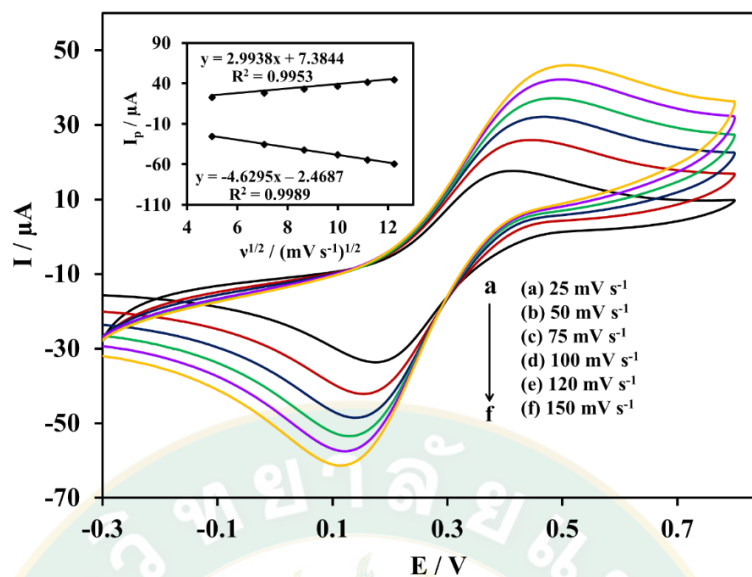
Figure 33 Cyclic voltammograms of the $Cu_2O@MnO_2$/GCE at various scan rates; 25 (a) 50 (b) 75 (c) 100 (d) 120 (e) and 150 (f) mV s^{-1} in 2 mM $K_3Fe(CN)_6$ containing 0.1 M KCl. The inset shows the relation between current response and square root of scan rate (25 - 150 mV s^{-1}).

Charge transfer rate constant, K_s

The Calculation of charge transfer rate constant (K_s) was carried out as 0.56 s^{-1} by using the following equations:

$$K_s = mnFv/ RT \quad .... (11)$$

where m is the peak-to-peak separation (0.2882 V), F is the Faraday constant (96,485 C mol^{-1}), v is the scan rate (50 mV s^{-1}), n is the number of transferred electrons (1), R is the gas constant (8.314 J mol^{-1} K^{-1}), T is the room temperature (298.15 K).

Diffusion coefficient value, D

The Calculation of diffusion coefficient value (D) was carried out as 1.65×10^{-5} cm^2 s^{-1} by using the following equations:

$$I_p = (2.69 \times 10^5) \, n^{3/2}AD^{1/2}Cv^{1/2} .... (12)$$

Where ν is the scan rate (50 mV s^{-1}), n is the number of transferred electrons (1), I$_p$ is the peak current response of the electrode (34.54 µA), A is the surface area of the electrode (7.065 x 10^{-2} cm^2), D is the diffusion coefficient (cm^2 s^{-1}), C is the bulk concentration (2 mM).

Electroactive surface area, A$_e$

Calculation of electroactive surface area (A$_e$) was carried out as 0.12 mm^2 by using the following equations:

$$A_e = S / (2.99 \times 10^5)n^{3/2}CD^{1/2} \quad\ldots\ldots\ldots\ldots(13)$$

where n is the number of transferred electrons (1), A_e is the electroactive surface area of the electrode (mm^2), D is the diffusion coefficient (1.65 x 10^{-5} cm^2 s^{-1}), C is the bulk concentration (2 mM), S is the slope of the straight line (2.9938 x 10^{-6}).

Surface concentration, γ

Calculation of electroactive surface area (A$_e$) was carried out as 1.04 x 10^{-8} mol cm^{-2} by using the following equations:

$$I_p = n^2F^2\,\gamma\,A\nu / 4RT \quad\ldots\ldots\ldots\ldots\ldots\ldots\ldots(14)$$

where F is the Faraday constant (96,485 C mol^{-1}), v is the scan rate (50 mV s^{-1}), n is the number of transferred electrons (1), R is the gas constant (8.314 J mol^{-1} K^{-1}), T is the room temperature (298.15 K), I_p is the peak current response of the electrode (34.54 µA), A is the surface area of the electrode (7.065 x 10^{-2} cm^2) and γ is the surface concentration (mol cm^{-2}).

The electrochemical impedance spectroscopy (EIS) of different modified electrodes was recorded as shown in Figure 34. The results showed that the bare GCE (a) provided the lowest value among all obtained resistances. However, the bare GCE (a) was inappropriate for H$_2$O$_2$ sensing compared to the other three different modified electrodes including of CHIT/GCE (b), CHIT-MnO$_2$/GCE (c) and CHIT-Cu$_2$O@MnO$_2$/ GCE (d). The results showed that the CHIT/GCE (b) provided the highest resistance. In

contrast to CHIT-MnO$_2$/GCE (c) and CHIT-Cu$_2$O@MnO$_2$/ GCE (d), the resistance decreased which the resistance of the CHIT-Cu$_2$O@MnO$_2$/GCE (d) was lower than the CHIT-MnO$_2$/GCE's (c). This also corresponded to 4.1.2 cyclic voltametric study. Thus, the CHIT-Cu$_2$O@MnO$_2$/GCE was suitable for the further work.

Table 5 Electrode impedance values

Electrodes	Z' / Ω
bare GCE	9,560
CHIT/GCE	12,358
CHIT-MnO$_2$/GCE	14,630
CHIT-Cu$_2$O@MnO$_2$/GCE	11,950
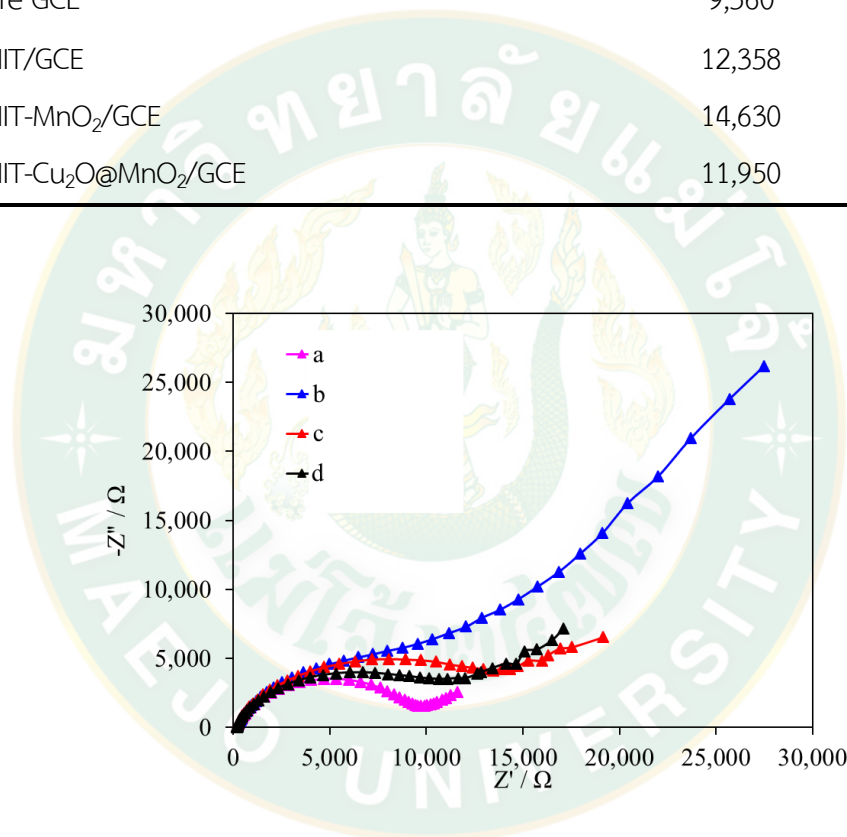
Figure 34 Nyquist diagram of electrochemical impedance spectra recorded from 0.01 to 10^5 Hz for 10.00 mM [Fe(CN)$_6$]$^{3-}$ in 0.1 M PBS pH 7.8 containing 0.10 M KCl at different modified electrodes: bare GCE (a), CHIT/GCE (b), CHIT-MnO$_2$/GCE (c) and CHIT-Cu$_2$O@MnO$_2$/GCE (d).

4.1.3 Applied potential

The Cu$_2$O@MnO$_2$/ GCE was studied by spiking 0.5 mM H$_2$O$_2$ at various applied potentials in the range of 0.60 to 0.90 V corresponding to H$_2$O$_2$ oxidation reaction

curve. As shown in Figure 36 the best current response was obtained at 0.75 V compared to the others at different potentials. So, the applied potential value of 0.75 V was chosen for the further work.
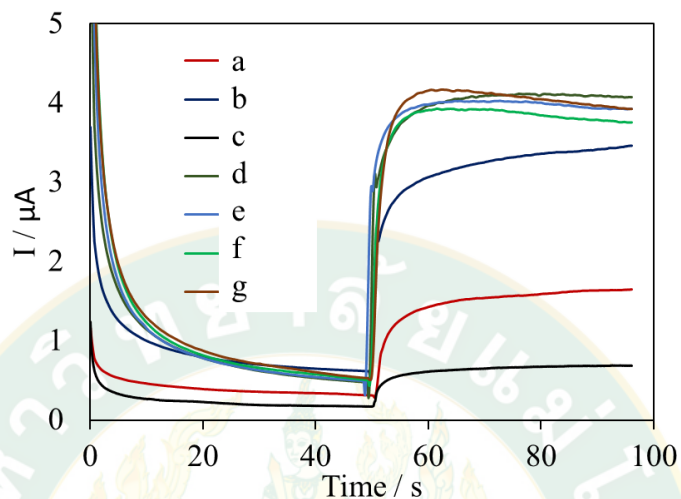
Figure 35 Amperogram at various applied potentals at 0.60 V (a), 0.65 V (b), 0.70 V (c), 0.75 V (d), 0.80 V (e), 0.85 V (f) and 0.90 V (g) in 0.1 M PBS pH 7.2 containing 0.5 mM H_2O_2.
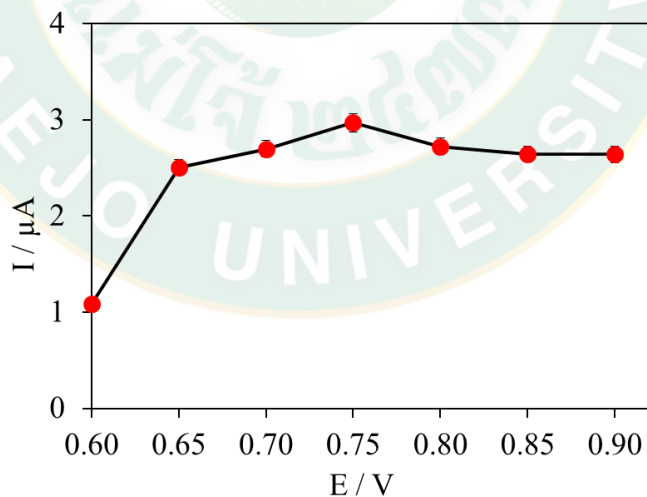
Figure 36 The influence of applied potential on the $Cu_2O@MnO_2$/GCE in 0.1 M PBS pH 7.2 containing 0.5 mM H_2O_2.

4.1.4 pH effect of the electrolyte solution

The current response can be affected by the pH of electrolyte solution in the experimental system leading to the difference in activity and stability of the modified electrode. To obtain a proper pH solution (0.1 M PBS), the current response of the $Cu_2O@MnO_2/GCE$ was investigated in the pH solution range from 6.0 to 8.0 in Figure 38 The results showed that the current response linearly increased at pH from 6.0 to 7.0 and dominantly increased at pH 7.2. After that, the current response slightly decreased at higher pH from 7.4 to 8.0. Therefore, a 0.1 M PBS solution of pH 7.5 was determined suitable for this experiment.
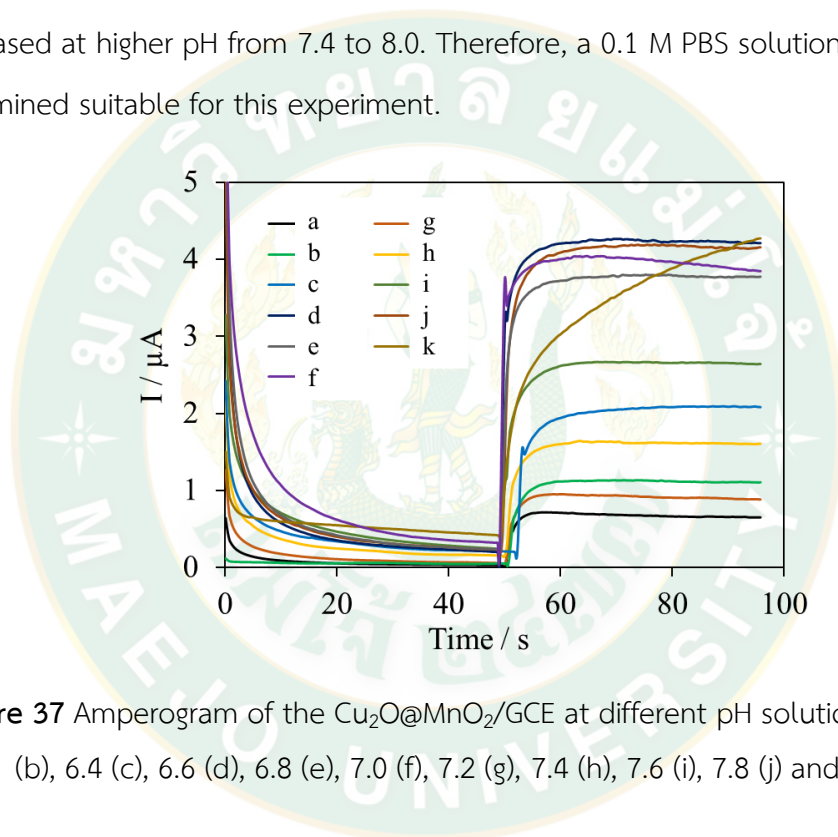
Figure 37 Amperogram of the $Cu_2O@MnO_2/GCE$ at different pH solution 6.0 (a), 6.2 (b), 6.4 (c), 6.6 (d), 6.8 (e), 7.0 (f), 7.2 (g), 7.4 (h), 7.6 (i), 7.8 (j) and 8.0 (k).
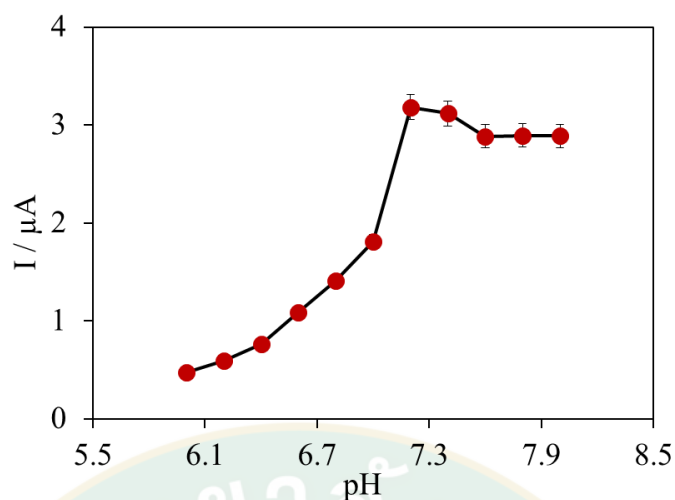
Figure 38 The influence of pH loading on the Cu$_2$O@MnO$_2$/GCE in 0.1 M PBS pH 7.2 containing 0.5 mM H$_2$O$_2$.

4.1.5 Effect of Cu$_2$O@MnO$_2$ concentration

The effect of Cu$_2$O@MnO$_2$ concentration on the electrochemical performance of the sensor was examined from 0 to 7 mg mL^{-1}. As can be seen in Figure 40 the current response increased from 0 to 4 mg mL^{-1} of Cu$_2$O@MnO$_2$ composite materials and it hardly changed from 4 to 5 mg mL^{-1}. Then, the current response clearly decreased at higher concentrations because of increasing resistance and decreasing electron transfer onto the electrode surface from the effect of the high resistance of composite materials at high thickness (Jeon et al., 2018; Liu and Ju, 2002; Zamfir et al., 2016)(Jeon et al., 2018; Liu and Ju, 2002; Zamfir et al., 2016)(Jeon et al., 2018; Liu and Ju, 2002; Zamfir et al., 2016) Thus, 4 mg mL^{-1} of Cu$_2$O@MnO$_2$ was used for the further study.
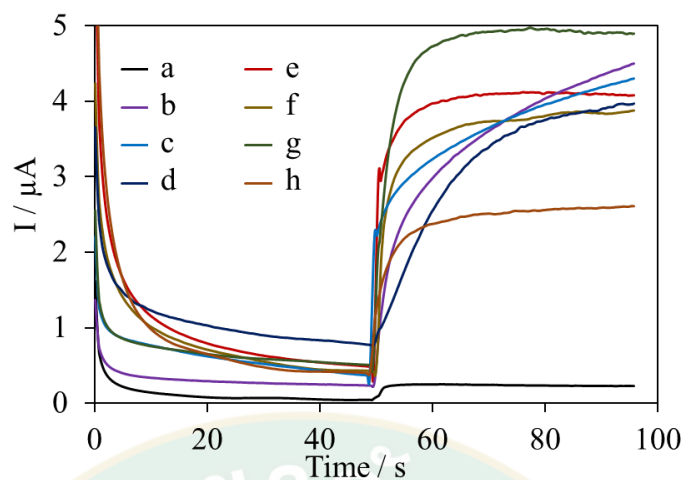
Figure 39 Amperogram at different $Cu_2O@MnO_2$ concentration 0.0 (a), 1.0 (b), 2.0 (c), 3.0 (d), 4.0 (e), 5.0 (f), 6.0 (g) and 7.0 mg mL^{-1} (h) in 0.1M PBS pH 7.2 containing 0.5 mM H_2O_2.
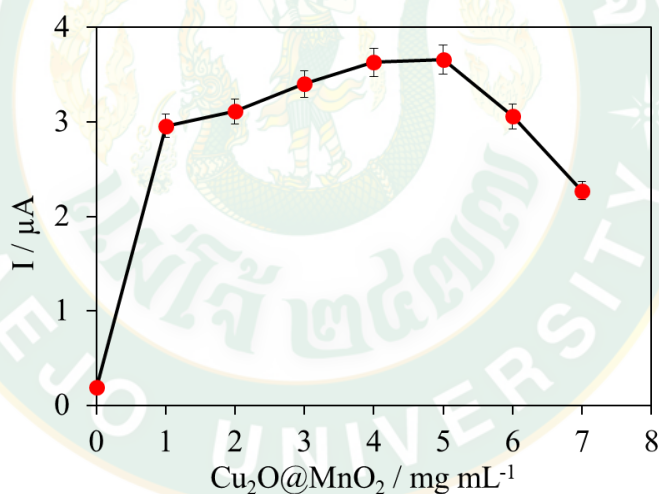
Figure 40 The influence of $Cu_2O@MnO_2$ concentration on the $Cu_2O@MnO_2$/GCE in 0.1M PBS pH 7.2 containing 0.5 mM H_2O_2 using the amperometric technique.

4.1.6 Amperometric H_2O_2 determination

To investigate the ability of H_2O_2 detection, the $Cu_2O@MnO_2$/GCE sensor was operated towards H_2O_2 addition for the study of linearity using the amperometric technique at the obtained optimal condition as discussed in topic Optimization of experimental parameters. Figure 41 presents the amperometric response of the

modified electrode with successive addition of H_2O_2 into 0.1 M PBS pH 7.2 at 0.75 V under continuous stirring (A) and the linear relation of response current and H_2O_2 concentration (B). The results showed that the current response of the sensor proportionally increased with increasing H_2O_2 concentration with a short time response less than 3 s of steady-state current resulting from high conductivity and excellent synergetic electrocatalyst acting of the $Cu_2O@MnO_2$ composite materials.

The developed sensor provided a wide linear range for the H_2O_2 oxidation reaction from 0.5 µM to 20 mM with a good sensitivity of 256.33 µA mM^{-1} cm^{-2}. The limit of detection (LOD) was calculated to be 63 nM (S/N=3) which suggested that the synthesized $Cu_2O@MnO_2$ composite materials greatly enhanced the performance of the sensor for quantitative H_2O_2 analysis.
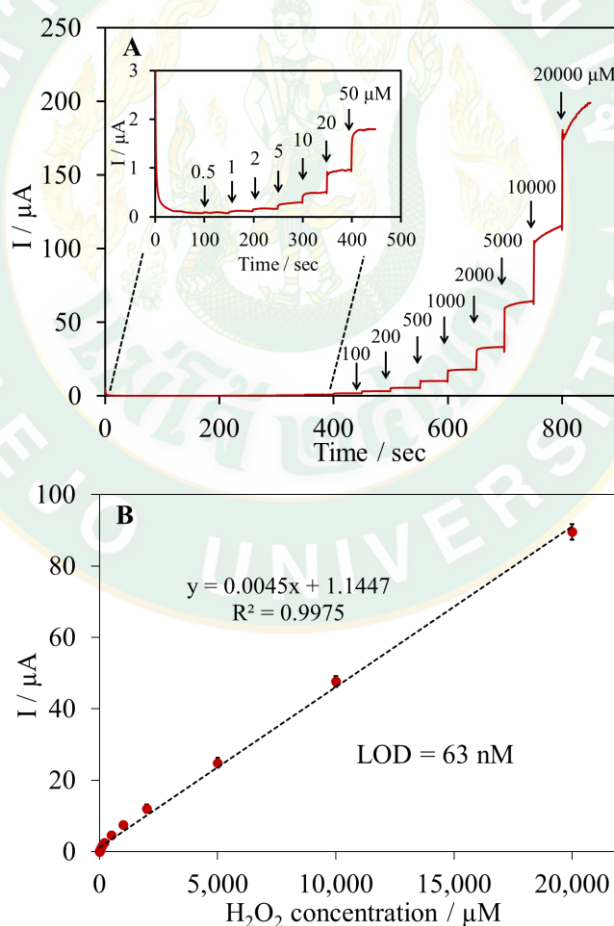
Figure 41 (A) Amperometric response of the modified electrode towards H_2O_2 addition from 0.5 to 20,000 µM in 0.1 M PBS pH 7.2. (B) A calibration curve between response current of the $Cu_2O@MnO_2$/GCE and H_2O_2 concentration.

4.1.7 Repeatability

The CHIT-Cu$_2$O@MnO$_2$/GCE was repetitively operated only one electrod in 0.1 M phosphate buffer solution pH 7.2 by spiking 5.0 mM H$_2$O$_2$ with applying amperometric technique for 7 times. The results showed acceptable % relative standard deviation as ± 0.82 lower than 5% presented in Table 6.

Table 6 Repeatability of the CHIT-Cu$_2$O@MnO$_2$/GCE.

No.	Current response (μA)
1	20.50
2	20.51
3	20.52
4	20.62
5	20.79
6	20.91
7	20.91
Average	20.68
Standard deviation	±0.17
% Relative standard deviation	±0.82

4.1.8 Reproducibility

All 7 CHIT-Cu$_2$O@MnO$_2$/GCE were tested in 0.1 M phosphate buffer solution pH 7.2 by spiking 0.5 mM H$_2$O$_2$ with applying amperometric technique. The results showed acceptable % relative standard deviation as 2.83 lower than 5% presented in Table 7.

Table 7 Reproducibility of the CHIT-Cu$_2$O@MnO$_2$/GCE.

No.	Current reponse (µA)
1	3.39
2	3.51
3	3.29
4	3.33
5	3.51
6	3.38
7	3.57
Average	3.43
Standard deviation	±0.09
% Relative standard deviation	±2.83

4.1.9 Operation time

The operation time of the CHIT-$Cu_2O@MnO_2$/GCE was repetitively evaluated in 0.1 M phosphate buffer solution pH 7.2 by spiking 5.0 mM H_2O_2 with applying amperometric technique until the current response lower than 50% of the first obtained current response. Following to the obtained result of this method, the operation time of CHIT-$Cu_2O@MnO_2$/GCE was higher than 100 operation times as presented in Figure 42 and Table 8
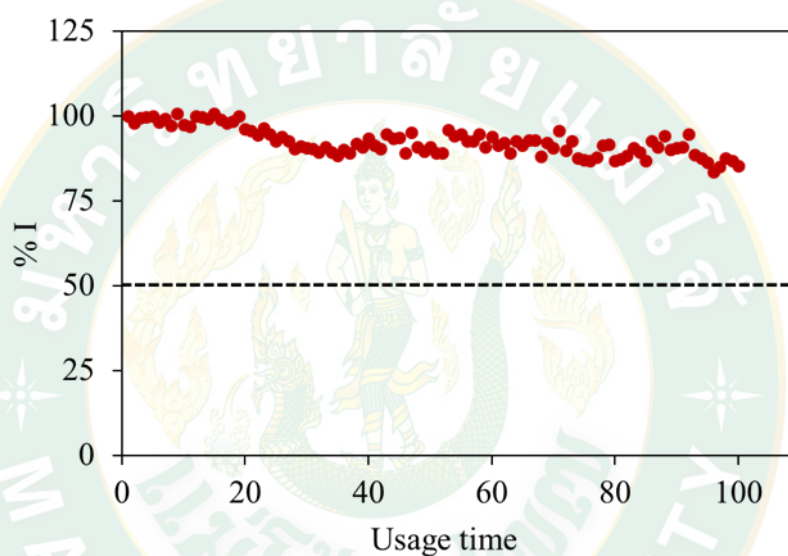
Figure 42 The operation time.

Table 8 The operation time of the H_2O_2 sensor at optimal condition.

Operation time (n)	I (µA)	%I	Operation time (n)	I (µA)	%I
1	23.03	100.00	29	20.98	91.10
2	22.56	97.96	30	20.86	90.58
3	22.88	99.34	31	20.78	90.23
4	22.98	99.78	32	20.59	89.41
5	23.01	99.91	33	20.91	90.80
6	22.58	98.05	34	20.55	89.23
7	22.87	99.31	35	20.31	88.19
8	22.36	97.11	36	20.73	90.00
9	23.21	100.78	37	20.49	88.97
10	22.44	97.44	38	21.13	91.73
11	22.31	96.87	39	20.92	90.82
12	23.03	99.99	40	21.51	93.38
13	22.98	99.78	41	21.01	91.25
14	22.86	99.26	42	20.79	90.29
15	23.21	100.78	43	21.81	94.69
16	22.80	99.00	44	21.51	93.38
17	22.54	97.87	45	21.56	93.64
18	22.68	98.48	46	20.51	89.05
19	23.00	99.87	47	21.91	95.13
20	22.15	96.18	48	20.91	90.81
21	22.03	95.66	49	20.91	90.81
22	21.73	94.36	50	20.85	90.67
23	22.22	96.48	51	20.51	89.08
24	21.79	94.62	52	20.53	89.13
25	21.35	92.71	53	22.08	95.87
26	21.61	93.83	54	21.68	94.12
27	21.33	92.62	55	21.81	94.69
28	20.82	90.39	56	21.32	92.56

Table 8 The operation time of the H_2O_2 sensor at optimal condition (continued).

Operation time (n)	I (µA)	%I	Operation time (n)	I (µA)	%I
57	21.30	92.50	79	21.10	91.62
58	21.81	94.69	80	19.99	86.79
59	20.91	90.80	81	20.08	87.19
60	21.61	93.82	82	20.34	88.32
61	21.02	91.27	83	20.86	90.57
62	21.21	92.08	84	20.60	89.45
63	20.53	89.13	85	19.99	86.79
64	21.35	92.71	86	21.30	92.49
65	21.02	91.25	87	20.94	90.95
66	21.41	92.95	88	21.68	94.15
67	21.39	92.88	89	20.73	90.01
68	20.29	88.10	90	20.86	90.57
69	21.21	92.09	91	20.95	90.96
70	20.86	90.57	92	21.82	94.74
71	22.00	95.53	93	20.42	88.69
72	20.69	89.84	94	20.16	87.53
73	21.30	92.49	95	19.87	86.28
74	20.16	87.53	96	19.25	83.60
75	20.08	87.18	97	19.56	84.94
76	20.00	86.84	98	20.14	87.45
77	20.22	87.80	99	20.00	86.84
78	21.06	91.45	100	19.64	85.27

4.1.10 Effect of interferences

The CHIT-Cu$_2$O@MnO$_2$/GCE was examined in 0.1 M phosphate buffer solution pH 7.2 in the presence of 0.1 mM H$_2$O$_2$ compared to the presence of different possible interfering species such as ascorbic acid, ethanol, glucose, sucrose and uric acid by using amperometry to obtain their minimal affecting concentrations (S/N=3) as presented in Figure 43 and Table 10.

Table 9 Interference effect on the H$_2$O$_2$ sensor.

Interfering species	Concentration (mg mL^{-1})	Background signal (µA)	Signal (µA)	S/N	Results
Ascorbic acid	0.500	0.058	0.047	0.810	Not interfere
(C$_6$H$_8$O$_6$)	1.250	0.059	0.202	3.423	Interfere
	2.500	0.057	0.23	4.035	Interfere
	3.750	0.057	0.402	7.051	Interfere
Ethanol	0.0038	0.037	0.030	0.810	Not interfere
(C$_2$H$_6$O)	0.0095	0.041	0.023	0.560	Not interfere
	0.0190	0.04	0.021	0.525	Not interfere
	0.0280	0.039	0.023	0.589	Not interfere
	0.0380	0.042	0.028	0.666	Not interfere
glucose	1.000	0.420	0.030	0.071	Not interfere
(C$_6$H$_{12}$O$_6$)	2.500	0.430	0.023	0.053	Not interfere
	5.000	0.040	0.021	0.525	Not interfere
	7.500	0.460	0.023	0.050	Not interfere
	10.000	0.042	0.028	0.666	Not interfere
sucrose	0.400	0.038	0.009	0.236	Not interfere
(C$_{12}$H$_{22}$O$_{11}$)	1.000	0.021	0.001	0.047	Not interfere
	2.000	0.021	0.002	0.095	Not interfere
	3.000	0.035	0.010	0.285	Not interfere
	4.000	0.035	0.010	0.285	Not interfere

Table 9 Interference effect on the H_2O_2 sensor (continued).

Interfering species	Concentration (mg mL^{-1})	Background signal (µA)	Signal (µA)	S/N	Results
Uric acid	0.0002	0.012	0.001	0.083	Not interfere
($C_5H_4N_4O_3$)	0.0005	0.015	0.005	0.333	Not interfere
	0.0010	0.012	0.003	0.250	Not interfere
	0.0015	0.014	0.012	0.857	Not interfere
	0.002	0.014	0.002	0.142	Not interfere
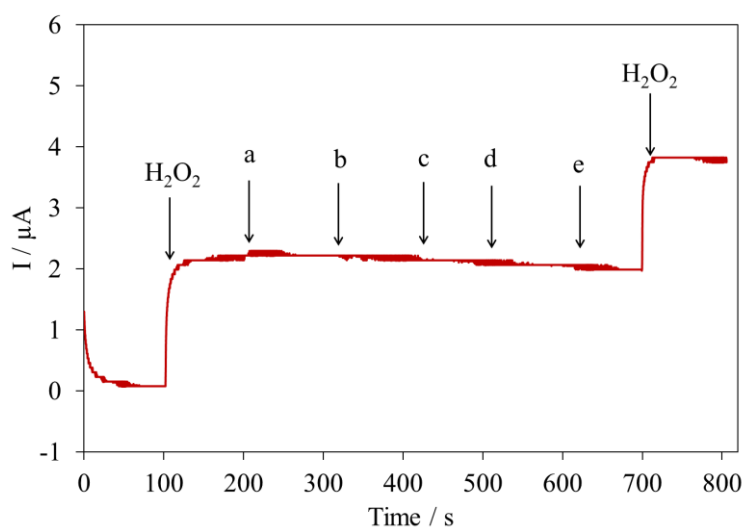
Figure 43 Interference effect on the $Cu_2O@MnO_2$/GCE by spiking 0.1 mM H_2O_2 (0.017 mg mL^{-1}) compared to 0.50 mg mL^{-1} ascorbic acid (a), 0.038 mg mL^{-1} ethanol (b), 10.00 mg mL^{-1} glucose (c), 4.00 mg mL^{-1} sucrose (d) and 0.002 mg mL^{-1} uric acid (e), respectively.

Table 10 Effect on interferences.

Interfering species	Minimal affecting concentration (mg mL^{-1})
Ascorbic acid ($C_6H_8O_6$)	1.25
Ethanol (C_2H_6O)	2.00%
glucose ($C_6H_{12}O_6$)	10.00
sucrose ($C_{12}H_{22}O_{11}$)	4.00
Uric acid ($C_5H_4N_4O_3$)	0.002

4.1.11 Sample analysis

The $Cu_2O@MnO_2$/GCE was applied to detect hydrogen peroxide concentration in 6 samples by standard addition method with applying amperometric technique at the optimal condition. Each sample was added various H_2O_2 concentrations including of 0, 50 and 500 μM, respectively. Then, these prepared sample solutions were spiked into 0.1 M phosphate buffer solution pH 7.2 for analysis. Each obtained current response was plotted with added standard H_2O_2 concentration by using regression method which H_2O_2 concentration in each sample was gained by extrapolating x-axis as presented in Table 4.5. After that, the prepared 250 μM H_2O_2 solution was added in each 25 μl sample for calculation of recovery percentage. The results showed H_2O_2 concentration between 26.50 to 50.45 μM of 5 samples with acceptable % recovery from 98.13 to 103.64 in Table 11

Table 11 H_2O_2 measurement in various samples

Sample	H_2O_2 in sample (μM)	H_2O_2 added (μM)	Increased H_2O_2 (μM)	Recovery (%)
Wound care solution 1	26.50	250	251.64	100.66
Wound care solution 2	38.40	250	253.17	101.27
Mouthwash 1	ND	250	ND	ND
Mouthwash 2	26.89	250	252.94	101.18
Hair dye 1	50.45	250	259.10	103.64
Hair dye 2	36.50	250	245.33	98.13

4.2 Choline biosensor

4.2.1 SEM-EDX and UV-Vis characterization of synthesized composite materials

The synthesized materials modified onto GCE surface were first characterized by using Field Emission Scanning Electron Microscope-Energy Dispersive X-ray spectrometer (SEM-EDX) and also Ultraviolet-Visible spectrophotometer (UV-Vis) for ZrO_2@AuNPs as shown in Figure 44. SEM images showed clear different shapes between ZrO_2@AuNPs (Figure 4.15A) and Cu_2O@MnO_2 in the free space cavity of ZrO_2@AuNPs (Figure 44 B) with a Cu_2O@MnO_2 diameter of 90-200 nm (square box in Figure 44 B) and 30-50 nm for ZrO_2@AuNPs (circle in Figure 44 B). The cross-section of the optimal modified electrode was examined, and presented a thickness of 46.5 μm as shown in Figure 44 C. Additionally, the prepared ZrO_2@AuNPs (Figure 44 Dc) was analyzed and compared to 1.0% gold chloride ($HAuCl_4$) solution (Figure 44 Da) and zirconium oxides (ZrO_2) solution (Figure 4.15 Db) by using UV-Vis technique. The UV-Vis Spectra exhibited absorption curves between 287 – 291 nm (Figure 44 Da-c) related to the absorption of the $AuCl_4^-$, ZrO_2, and ZrO2@AuNPs were mixed in water, whereas the dominant absorption peak at 529 nm (Figure 44 Dc) was related to the ZrO_2@AuNP. This phenomenon is primary confirmed that the nanoparticle sized of ZrO_2 and AuNP were formed. EDX was also applied to confirm the successful composition modification of each element at the modified surface, and provided the spectrum peak with the percent weight of C, O, Mn, Cu, Zr, and Au, at 6.65, 23.29, 29.75, 5.01, 22.68, and 12.62 % respectively (Figure 44 E).
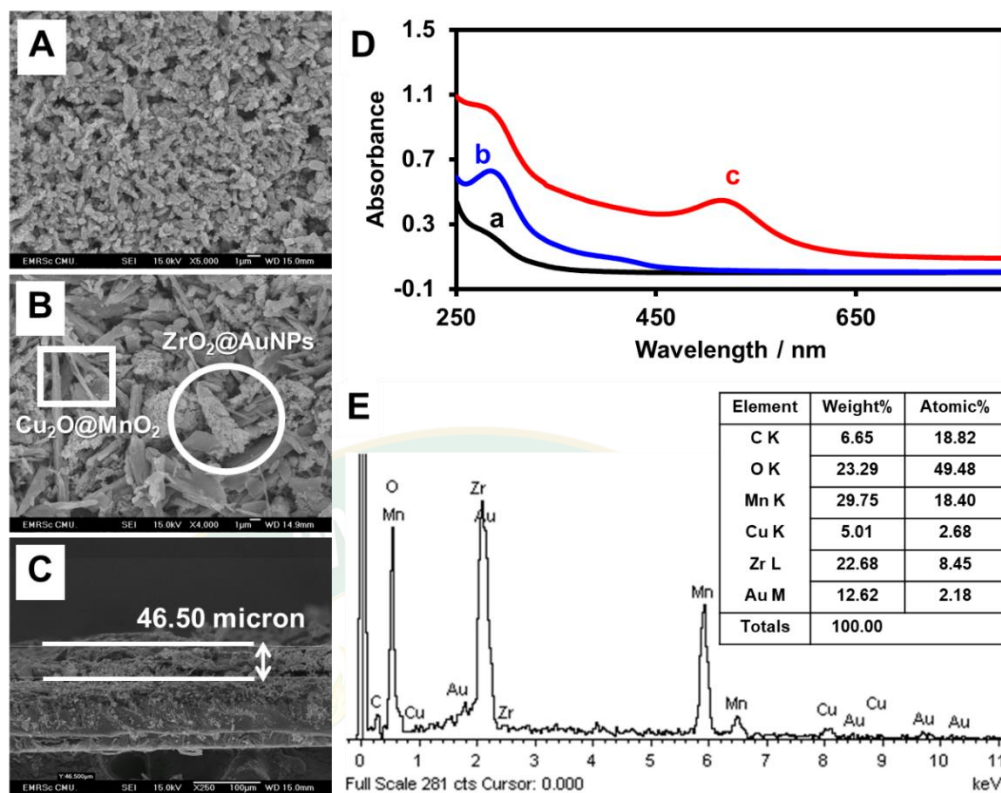
Figure 44 Scanning electron microscope (SEM) images of ZrO_2@AuNPs (A) COx/Cu_2O@MnO_2/ZrO_2@AuNPs/GCE surface (B) and the cross-section of the optimal modified electrode (C). Ultraviolet-visible spectra (D) of 1.0% $HAuCl_4$ solution (a) ZrO_2 (b) and ZrO_2@AuNPs (c), respectively. Energy Dispersive X-ray (EDX) spectrum (E) of the COx/Cu_2O@MnO_2/ZrO_2@ AuNPs/GCE.

4.2.2 Cyclic voltammetric study

The COx/CHIT/GCE

The COx/CHIT/GCE was operated in 0.1 M phosphate buffer solution pH 7.8 compared to the presence of 0.0 (a), 1.0 (b) and 2.5 mM (c) choline by using cyclic voltammetry. The results showed the obtained cyclic voltammograms which there is no difference both absence and presence of choline as presented in Figure 45. This might be because of non-conductivity property of CHIT polymer film which limited the electron transfer process onto the electrode surface. However, CHIT polymer film is biocompatible and flexible to enhance the robustness for modification onto the

electrode surface which this point can be improved by applying interesting conducting material for further modification.
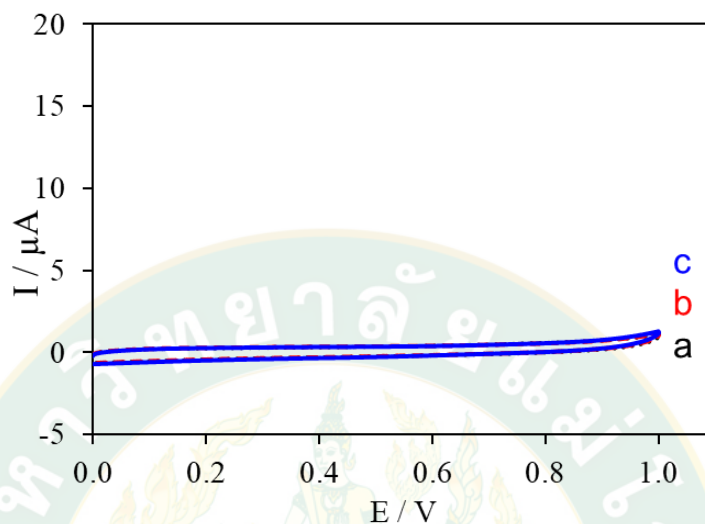
Figure 45 Cyclic voltammograms of the COx/CHIT/GCE in 0.1 M phosphate buffer solution pH 7.8 containing 0.0 (a), 1.0 (b) and 2.5 mM (c) choline.

The COx/ZrO$_2$@AuNPs/GCE

The COx/ZrO$_2$@AuNPs/GCE was operated in 0.1 M phosphate buffer solution pH 7.8 compared to the presence of 0.0 (a), 1.0 (b) and 2.5 mM (c) choline by using cyclic voltammetry in Figure 46. The results showed the obtained cyclic voltammograms which the curve of the byproduct H$_2$O$_2$ oxidation reaction (b, c) unclearly increased compared to the blank solution (a). Thus, this method needed to be improved by applying additional interesting conducting material for further modification.
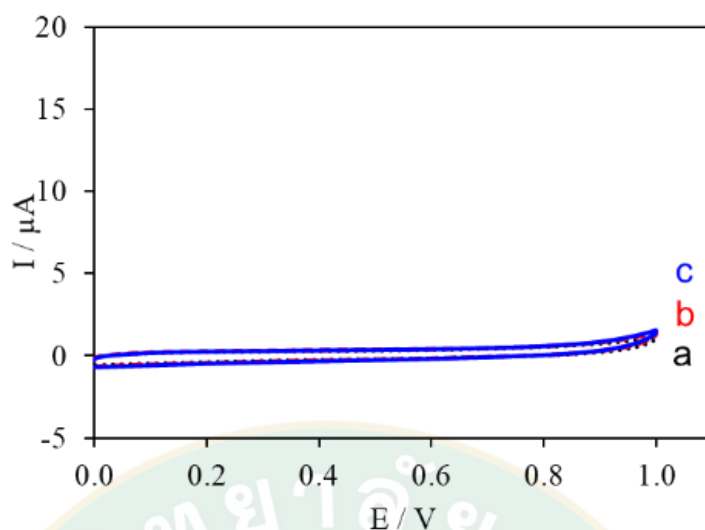
Figure 46 Cyclic voltammograms of the COx/CHIT-ZrO$_2$@AuNPs/GCE in 0.1 M phosphate buffer solution pH 7.8 containing 0.0 (a), 1.0 (b) and 2.5 mM (c) choline.

The COx/CHIT-Cu$_2$O@MnO$_2$/GCE

In Figure 47, the COx/CHIT-Cu$_2$O@MnO$_2$/GCE was operated in 0.1 M phosphate buffer solution pH 7.8 compared to the presence of 0.0 (a), 1.0 (b) and 2.5 mM (c) choline by using cyclic voltammetry. The results showed the obtained cyclic voltammograms which the curve of the byproduct H$_2$O$_2$ oxidation reaction (b, c) obviously increased with increasing choline concentration from 0.6 to 1.0 V compared to the blank solution (a). This suggested that CHIT- Cu$_2$O@MnO$_2$ modified onto GCE enhanced the electron transfer process onto the electrode surface for choline analysis.
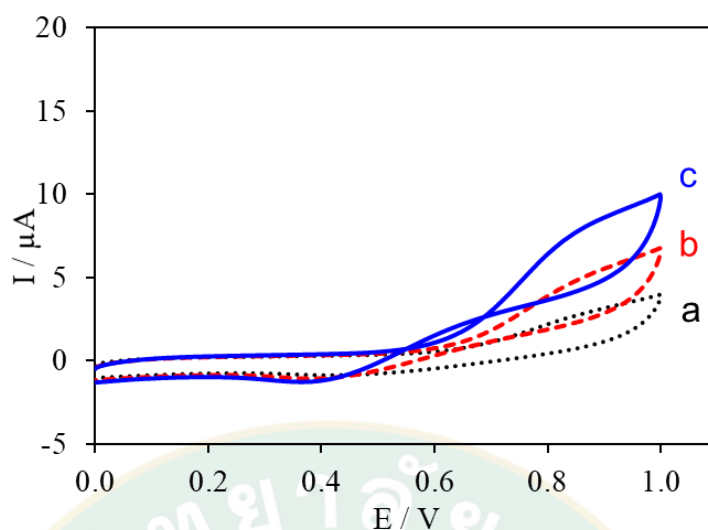
Figure 47 Cyclic voltammograms of the COx/CHIT-Cu$_2$O@MnO$_2$/GCE in 0.1 M phosphate buffer solution pH 7.8 containing 0.0 (a), 1.0 (b) and 2.5 mM (c) choline.

The COx/Cu$_2$O@MnO$_2$-CHIT-ZrO$_2$@AuNPs/GCE

The COx/Cu$_2$O@MnO$_2$-CHIT-ZrO$_2$@AuNPs/GCE was operated in 0.1 M phosphate buffer solution pH 7.8 compared to the presence of 0.0 (a), 1.0 (b) and 2.5 mM (c) choline by using cyclic voltammetry as shown in Figure 48. The results showed the obtained cyclic voltammograms which the curve of the byproduct H$_2$O$_2$ oxidation reaction (b, c) obviously increased with respect to choline concentration from 0.45 to 1.0 V compared to the blank solution (a). Additionally, the obtained current response was very higher than the COx/CHIT-Cu$_2$O@MnO$_2$/GCE resulting from the electro-mediator behavior of synthesized Cu$_2$O@MnO$_2$ onto the working electrode surface. This suggested that the synergetic of Cu$_2$O@MnO$_2$ and ZrO$_2$@AuNPs modified onto GCE effectively enhanced the electron transfer process onto the electrode surface. Therefore, the COx/Cu$_2$O@MnO$_2$-CHIT-ZrO$_2$@AuNPs/GCE was selected for the further work.
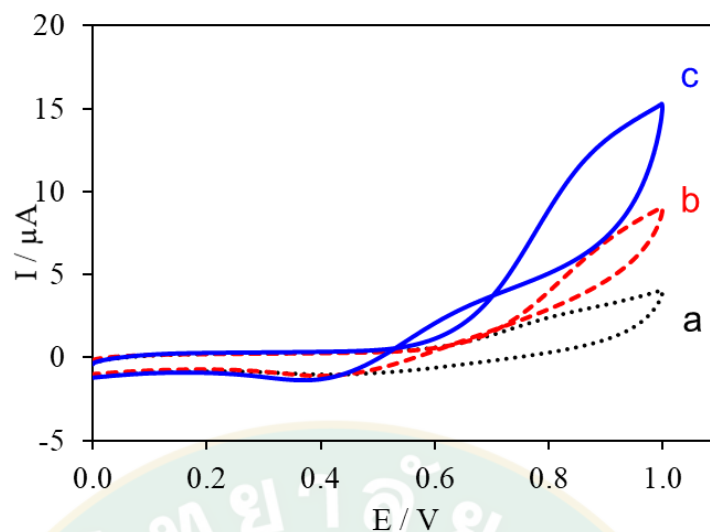
Figure 48 Cyclic voltammograms of the COx/Cu$_2$O@MnO$_2$-CHIT-ZrO$_2$@AuNPs/GCE in 0.1 M phosphate buffer solution pH 7.8 containing 0.0 (a), 1.0 and 2.5 mM (c) choline.

Therefore, the COx/Cu$_2$O@MnO$_2$-CHIT-ZrO$_2$@AuNPs/GCE was selected for the further work which then was operated in 0.1 M phosphate buffer solution pH 7.8 containing 0.0, 0.5, 1.0, 2.0 and 4.0 mM choline, respectively, by using cyclic voltammetry from 0.0 to 1.0 V at 50 mVs^{-1} in Figure 49. The results showed that the current response of H$_2$O$_2$ oxidation reaction curve at 0.8 V clearly increased with increasing choline concentrations. This suggested that this method can be applied for choline quantitative analysis.
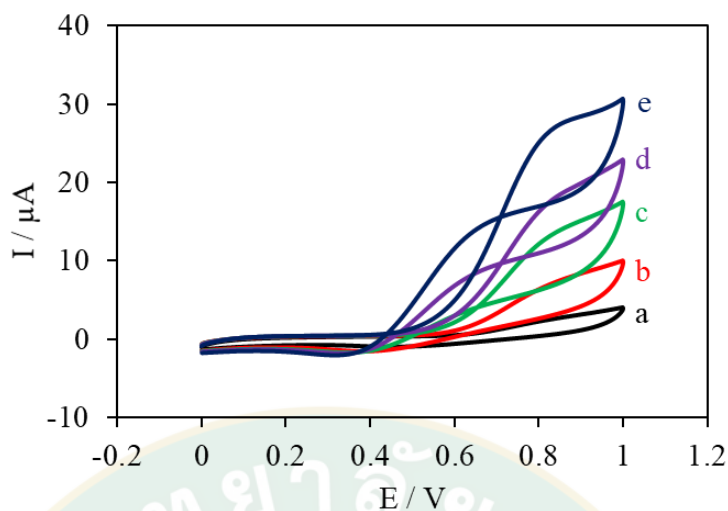
Figure 49 Cyclic voltammograms of the COx/Cu$_2$O@MnO$_2$-CHIT-ZrO$_2$@AuNPs/GCE in 0.1 M phosphate buffer solution pH 7.8 containing 0.0 (a), 0.5 (b), 1.0 (c) 2.0 (d) and 4.0 mM choline at 50 mVs^{-1} scan rate.

The effect of various potential scan rates (10 to 80 mV s^{-1}) in the oxidation response of the COx/Cu$_2$O@MnO$_2$/ZrO$_2$@AuNPs/GCE was tested in order to study its electrochemical behavior and kinetics, as presented in the cyclic voltammograms (Figure 4.21). The oxidation current increased linearly with the potential scan rate and provided the linear relationship between peak current responses and the square root of the scan rates (Figure 50), suggesting that the associated oxidation process of the modified electrode is a diffusion-controlled process. In addition to the kinetic parameters, charge transfer rate constant (K_s) can be calculated by using the Laviron equation, diffusion coefficient value (D) and electroactive surface area (A_e) gained by Randles-Sevcik equations, while surface concentration (γ) obtained by using Brown-Anson model equal to 0.97 s^{-1}, 4.50×10^{-6} cm^2 s^{-1}, 0.24 mm^2 and 0.54×10^{-8} mol cm^{-2}, for K_s, D, A_e, and γ respectively.
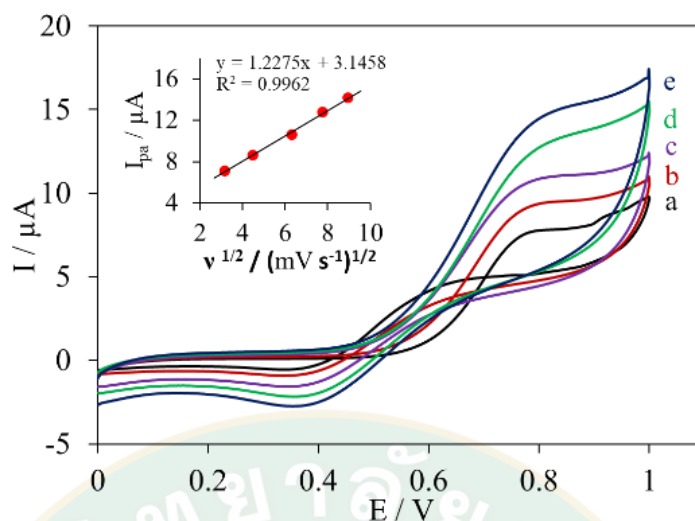
Figure 50 Cyclic voltammograms of Effect of various potential scan rates (E) on the
electrochemical response of the $COx/Cu_2O@MnO_2/ZrO_2@AuNPs/GCE$
in 0.1 M PBS pH 7.8 containing 2.0 µM choline at scan rate of 10 (a),
20 (b), 40 (c), 60 (d), and 80 (e) mV s^{-1}.

Charge transfer rate constant, K_s

The Calculation of charge transfer rate constant (K_s) was carried out as 0.97 s^{-1}
by using the following equations:

$$K_s = mnF\nu / RT ....(15)$$

where m is the peak-to-peak separation (0.50 V), F is the Faraday constant
(96,485 C mol^{-1}), ν is the scan rate (50 mV s^{-1}), n is the number of transferred
electrons (1), R is the gas constant (8.314 J mol^{-1} K^{-1}), T is the room temperature
(298.15 K).

Diffusion coefficient value, D

The Calculation of diffusion coefficient value (D) was carried out as 4.50 x 10^{-6}
cm^2 s^{-1} by using the following equations:

$$I_p = (2.69 \times 10^5) \, n^{3/2}AD^{1/2}C\nu^{1/2}............(16)$$

Where ν is the scan rate (50 mV s^{-1}), n is the number of transferred electrons
(1), I_p is the peak current response of the electrode (18.04 µA), A is the surface area

of the electrode (7.065×10^{-2} cm^2), D is the diffusion coefficient (cm^2 s^{-1}), C is the bulk concentration (2 mM).

Electroactive surface area, A_e

The Calculation of electroactive surface area (A_e) was carried out as 0.10 mm^2 by using the following equations:

$$A_e = S \,/\, (2.99 \times 10^5)n^{3/2}CD^{1/2} \quad\text{.................(17)}$$

where n is the number of transferred electrons (1), A_e is the electroactive surface area of the electrode (mm^2), D is the diffusion coefficient (4.50×10^{-6} cm^2 s^{-1}), C is the bulk concentration (2 mM), S is the slope of the straight line (1.2275×10^{-6}).

Surface concentration, γ

The Calculation of electroactive surface area (A_e) was carried out as 0.54×10^{-8} mol cm^{-2} by using the following equations:

$$I_p = n^2F^2\gamma A\mathbf{v} \,/\, 4RT \quad\text{.................(18)}$$

where F is the Faraday constant (96,485 C mol^{-1}), $\mathbf{v}$ is the scan rate (50 mV s^{-1}), n is the number of transferred electrons (1), R is the gas constant (8.314 J mol^{-1} K^{-1}), T is the room temperature (298.15 K), I_p is the peak current response of the electrode (18.04 μA), A is the surface area of the electrode (7.065×10^{-2} cm^2) and γ is the surface concentration (mol cm^{-2}).

The electrochemical impedance spectroscopy (EIS) of different modified electrodes was recorded as shown in Figure 51. The results showed different EIS spectra of each modified electrode consisting of a semicircle at a high frequency range and a line at a low frequency range. These results demonstrated that all of the obtained modified electrode processes were controlled by electron transfer at high frequency and by diffusion at low frequency. Compared to the bare GCE (Figure 51 a), the diameter of the semicircle increased with the modified ZrO$_2$@AuNPs/GCE (Figure 51 b) related to the

limited electrochemical activity of ZrO_2 itself. In contrast to the $Cu_2O@MnO_2$ /ZrO_2@AuNPs (Figure 51 c), the diameter of the semicircle decreased due to their synergistic property. However, the diameter decreased when COx was immobilized onto $Cu_2O@MnO_2/ZrO_2@$ AuNPs/GCE (Figure 51 d) resulting from the inherent insulator of the enzyme. As a result, it can be concluded that the electron transfer through the prepared $Cu_2O@MnO_2/ZrO_2@$AuNPs composite material layer on to GCE surface is facile owing to their electrocatalytic effects.
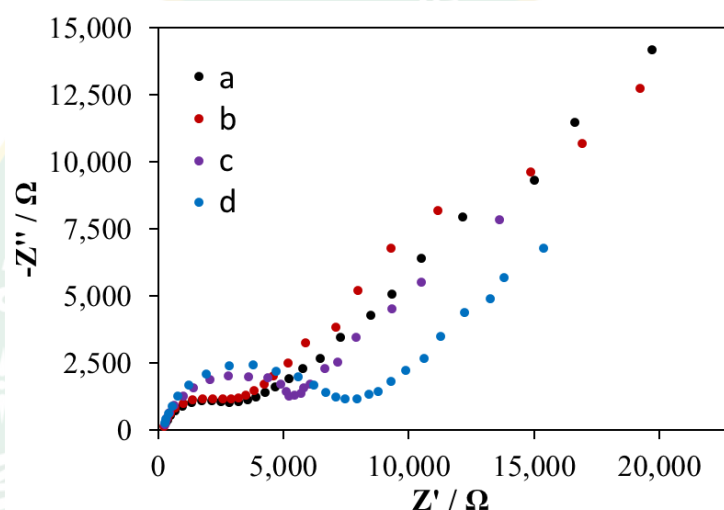
Figure 51 Nyquist diagram of electrochemical impedance spectra (F) recorded from 0.01 to 10^5 Hz for 10.00 mM $[Fe(CN)_6]^{3-}$ in 0.1 M PBS pH 7.8 containing 0.10 M KCl at different modified electrodes: bare GCE (a) ZrO_2@AuNPs/GCE (b) $Cu_2O@MnO_2/ZrO_2$@AuNPs/GCE (c) and COx/$Cu_2O@MnO_2/ZrO_2$@AuNPs/GCE (d).

Table 12 Electrode impedance values

Electrodes	Z'/Ω
bare GCE	3,210
ZrO_2@AuNPs/GCE	3,214
$Cu_2O@MnO_2/ZrO_2@$ AuNPs/GCE	5,342
COx/$Cu_2O@MnO_2/ZrO_2$@AuNPs/GCE	7,750

Following cyclic voltammetric study, the result presented such dominant ability of the COx/Cu$_2$O@MnO$_2$/ZrO$_2$@AuNPs/GCE to enhance the catalytic reaction of choline oxidase to choline which each obtained current response value related to choline concentration. Additionally, this modified electrode provided the current response much more than the bare GCE as 15 times. The mechanism for choline analysis was illustrated in Figure 52. The modified electrode, COx/Cu$_2$O@MnO$_2$/ZrO$_2$@AuNPs/ GCE, was dipped into 0.1 M phosphate buffer solution pH 7.8 in the presence of choline. The working electrode in the system was applied the potential from the potentiostat instrument. Then, choline was catalyzed by choline oxidase and provided H$_2$O$_2$ and betaine aldehyde. After that the byproduct H$_2$O$_2$ oxidation reaction happened and provided the electron to the working electrode surface resulting in electron flow in the area with the synergetic of Cu$_2$O@MnO$_2$ and ZrO$_2$@AuNPs onto the electrode surface as an electro-mediator.
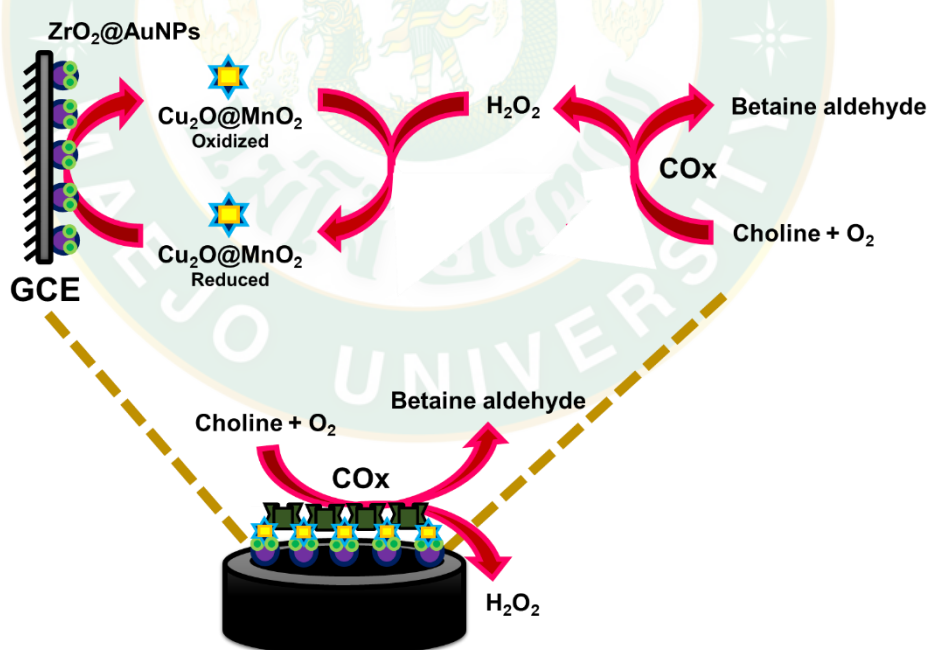
Figure 52 Schematic illustrating the proposed mechanism of choline detection, possible formed enzyme choline oxidase (COx) and synthesized composite materials of ZrO$_2$@AuNPs, and Cu$_2$O@MnO$_2$ onto the glassy carbon electrode (GCE) surface.

4.2.3 Applied potential

To obtain the maximum current response of the $COx/Cu_2O@MnO_2/ZrO_2@$ AuNPs/GCE biosensor for choline measurement, the significant parameters including operating potential, pH of the supporting electrolyte, temperature, enzyme loading, $ZrO_2@AuNPs$ content and the amount in mass of $Cu_2O@MnO_2$ composites were optimized by applying an amperometric technique. The effect of the applied potential on the biosensor performance was tested in 0.1 M PBS pH 7.4. As presented in Figure 54, the current response of 0.25 mM choline was studied at various positive potential values from 0.65 to 0.90 V vs. Ag/AgCl reference electrode. The obtained current response increased from 0.65 to 0.75 V. After that, the response decreased for more positive potentials which almost remained constant from 0.80 to 0.90 V. As a result, a potential value of 0.75 V was selected as the applied potential for further experiment
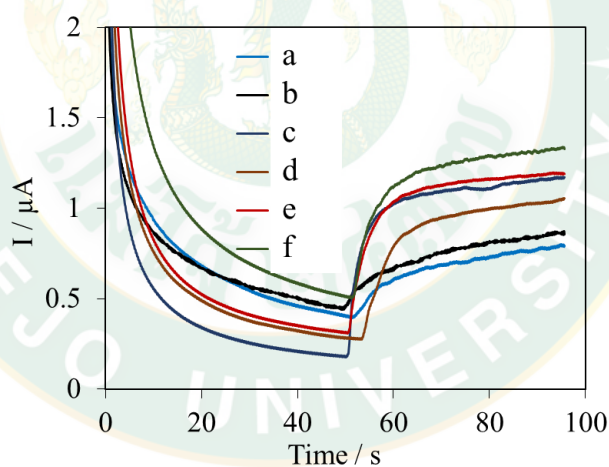
Figure 53 Amperogram at various applied potentals at 0.65 V (a), 0.70 V (b), 0.75 V (c), 0.80 V (d), 0.85 V (e) and 0.90 V (f) in 0.1 M PBS containing 0.25 mM choline
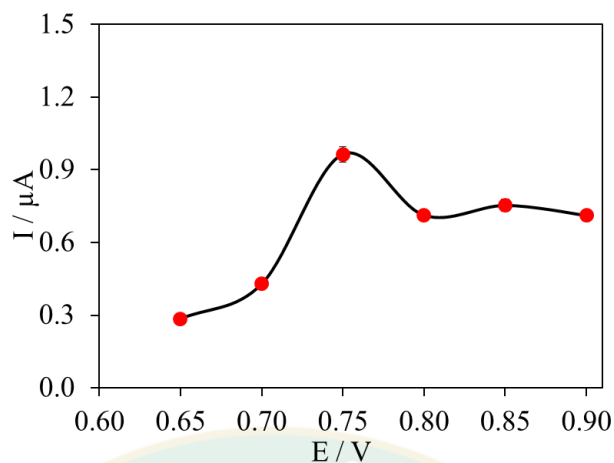
Figure 54 The influence of applied potential on GCE in 0.1 M PBS containing 0.25 mM choline by using amperometry.

4.2.4 pH effect of the electrolyte solution

The influence of the pH loading on the developed amperometric choline biosensor was operated over the range from 6.8 to 8.0 in 0.1 M PBS at fixed applied potential of 0.75 V in Figure 56. The current response increased with increasing pH value from 6.8 to 7.8 and then notoriously decreased at pH 8.0. As the optimum pH 7.8 reported in agreement with that specified by the supplier of the enzyme and also corresponded to previous reports (Doretti et al., 2000; Shimomura et al., 2009), this pH value was thus chosen for further study
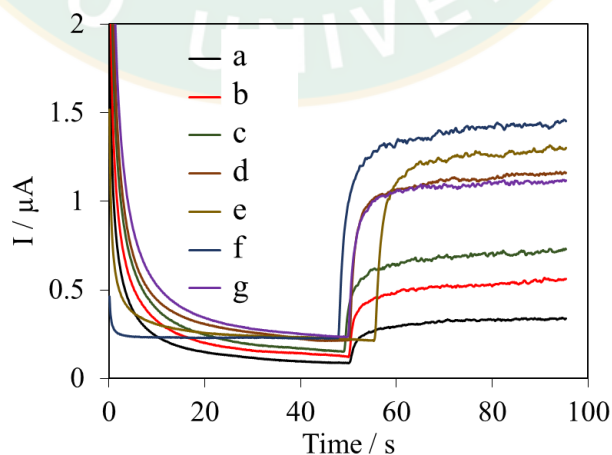
Figure 55 Amperogram in different pH of 0.1 PBS solution at 6.8 (a), 7.0 (b), 7.2 (c), 7.4 (d), 7.6 (e), 7.8 (f) and 8.0 (g) in 0.25 mM choline.
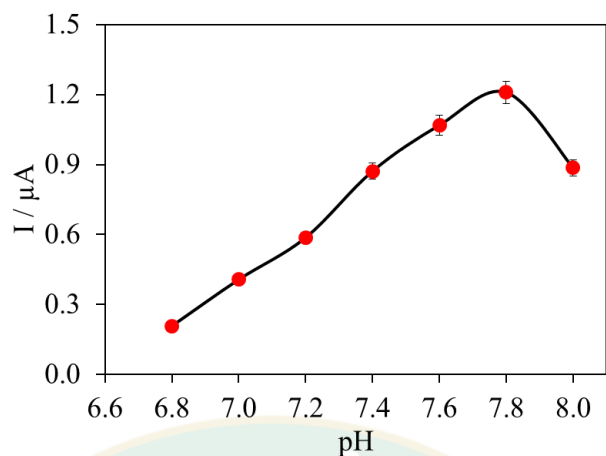
Figure 56 The influence of pH in 0.1 M PBS containing 0.25 mM choline .

4.2.5 Effect of temperature

In Figure 58, the effect of temperature was studied in the range of 30 to 50 degree celsius, which was performed in 0.1 M PBS pH 7.8 at 0.75 V. The amperometric response increased from 30 to 40 degrees Celsius, where the highest current response was obtained, then decreased at higher temperature. Hence, the temperature of 40 degrees Celsius was selected which was related to the earlier literatures (Kok et al., 2001; Razola et al., 2003).
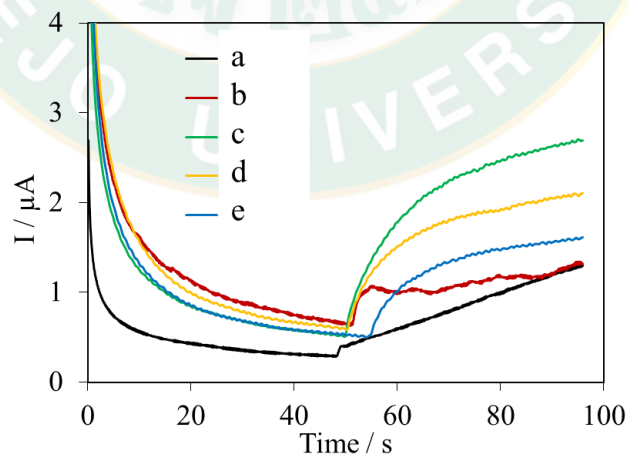
Figure 57 Amperogram at different temperature 30 (a), 35 (b), 40 (c), 45 (d) and 50 ^{o}C (e) in 0.1 M PBS containing 0.25 mM choline.
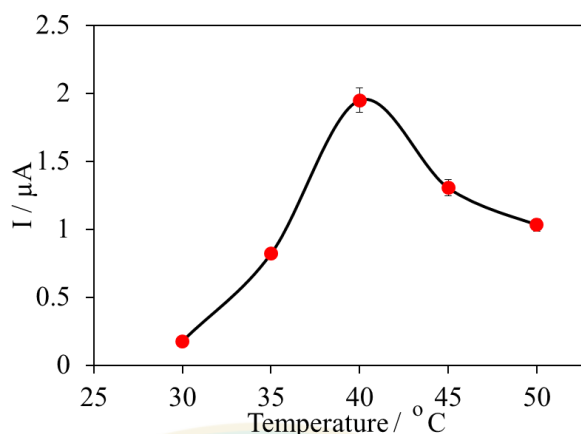
Figure 58 The influence of temperature on GCE in 0.1 M PBS containing 0.25 mM choline by using amperometry.

4.2.6 Effect of enzyme concentration

The enzyme loading had great influence on the biosensor response as well. The fabricated choline biosensor immobilized with different COx loadings, from 0.20 to 2.5 U, was thus investigated while the amount of modified composite materials, $ZrO_2@AuNPs$ and $Cu_2O@MnO_2$, were fixed at optimal applied potential, pH and temperature as shown in **Figure *60*** The influence of enzyme loading on GCE in 0.1 M PBS containing 0.25 mM It can be clearly noticed that the current response improved as the amount of COx increased to 1.0 U and then it was almost stable above this concentration. Therefore, the COx loading as 1.0 U was suitable for this experiment.
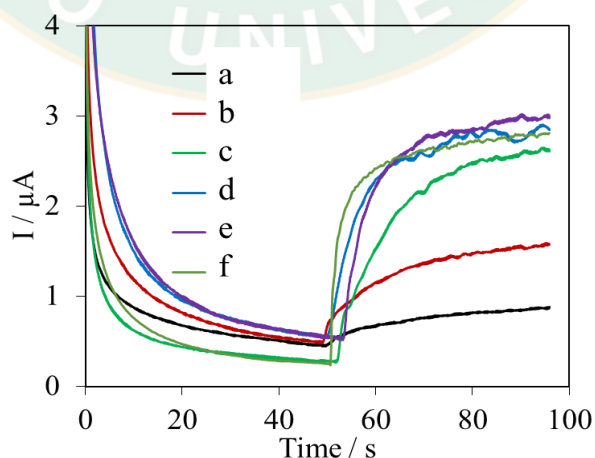
Figure 59 Amperogram at different COx loadings 0.25 (a), 0.5 (b), 1.0 (c), 1.5 (d), 2.0 (e) and 2.5 units (f) in 0.1 M PBS containing 0.25 mM choline.
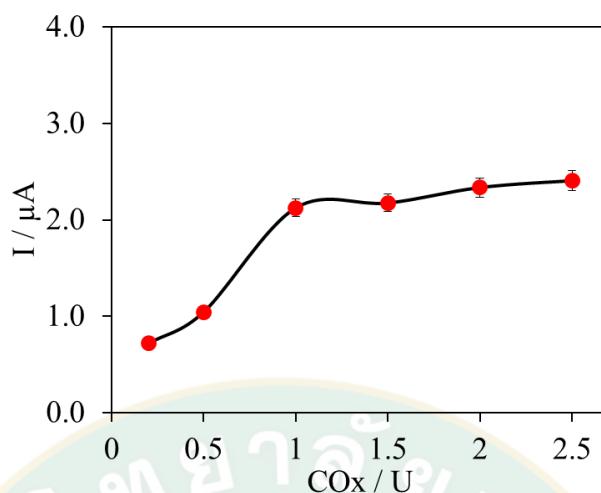
Figure 60 The influence of enzyme loading on GCE in 0.1 M PBS containing 0.25 mM

4.2.7 Effect of ZrO$_2$@AuNPs concentration

The effect of ZrO$_2$@AuNPs concentration modified onto the working electrode surface was studied by using amperemetry as showed in Figure 62. The results showed that the current response obviously increased with increasing ZrO$_2$@AuNPs concentration from 0 to 10.0 mg mL^{-1}. After that, the current response was stable. Thus, 10.0 mg mL^{-1} ZrO$_2$@AuNPs was selected for the further experiment.
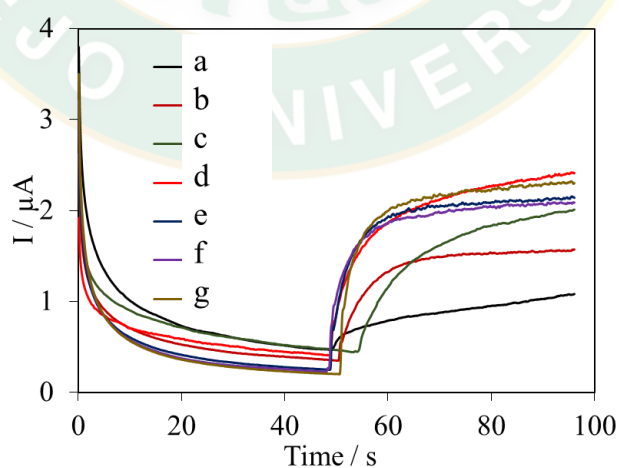
Figure 61 Amperogram at different ZrO$_2$@AuNPs concentration 0.0 (a), 2.5 (b), 5.0 (c), 10 (d), 20 (e) 30 (f) and 40 mg mL^{-1} (g) in 0.1 M PBS containing 0.25 mM choline.
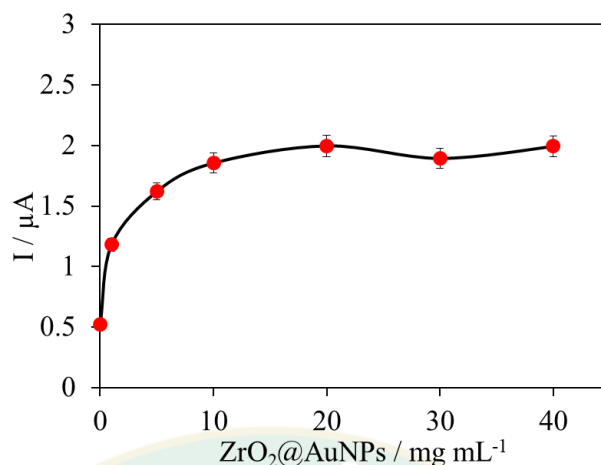
Figure 62 The influence of ZrO_2@AuNPs content on GCE in 0.1 M PBS containing 0.25 mM choline

4.2.8 Effect of Cu_2O@MnO_2 concentration

The effect of Cu_2O@MnO_2 concentration modified onto the working electrode surface was studied by using amperemetry as well in Figure 64. The results showed that the current response obviously increased with increasing Cu_2O@MnO_2 concentration. However, the current response clearly decreased when Cu_2O@MnO_2 concentration was higher than 5.0 mg mL^{-1} resulting from the modified material's thickness which affected electron transfer process onto the electrode surface. Thus, 5.0 mg mL^{-1} Cu_2O@MnO_2 was chosen for this method.
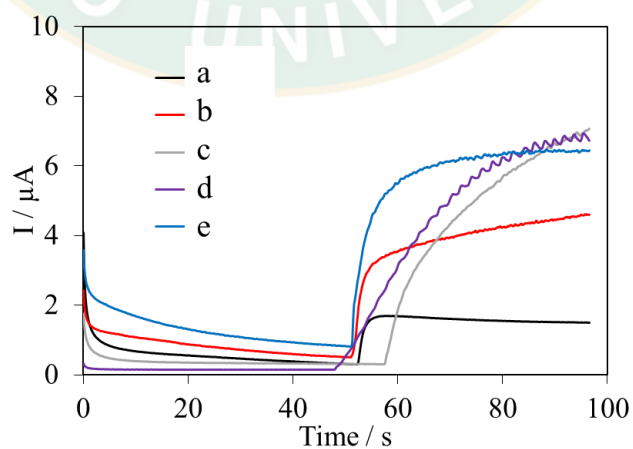
Figure 63 Amperogram at different Cu_2O@MnO_2 concentration 0.0 (a), 1.0 (b), 2.5 (c), 5.0 (d) and 10.0 (e) in 0.1 M PBS containing 0.25 mM choline.
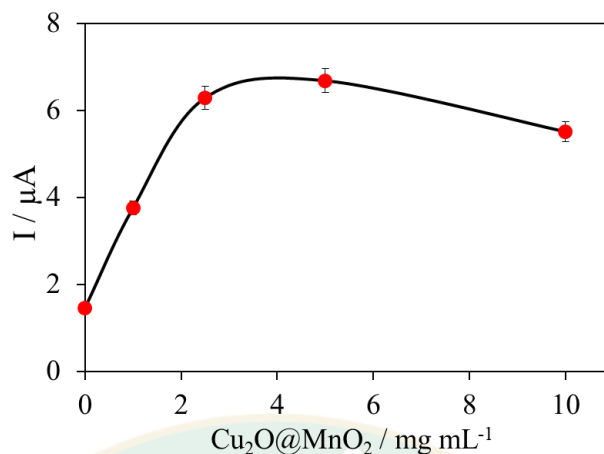
Figure 64 The influence of quantity of $Cu_2O@MnO_2$ composites on GCE in 0.1 M PBS containing 0.25 mM choline by using amperometry.

4.2.9 Linearity

Linearity performance of the $COx/Cu_2O@MnO_2/ZrO_2@AuNPs/GCE$ biosensor for choline detection was tested by applying amperometry under the optimized conditions described in section 3.3. A potential of 0.75 V was applied to this biosensor owing to its highest current response. As presented in Figure 65, the modified electrode provided amperometric responses proportionally increasing with choline addition from 0.5 to 1,000.0 µM into 0.1 M PBS pH 7.8, reaching rapidly 90.0% of the steady-state current in an average time less than 3s (for 0.5 to 750.0 µM choline) and in 35s at the highest concentration (1,000.0 µM choline). This fast response at widely concentration of choline d u e to the high conductivity and synergetic electrocatalyst acting of the modified $Cu_2O@MnO_2$ and $ZrO_2@AuNPs$ composite materials layers onto the electrode surface. Additionally, the calibration curve shown in Figure 66 indicated that the developed biosensor had a wide linear response to choline concentration with good sensitivity (97.4 µA cm^{-2} mM^{-1}) and low detection limit (0.3 µM, S/N= 3). This phenomenon suggested that our modified materials greatly improved the electron transfer process leading to the effective performance of the biosensor for quantitative choline detection.
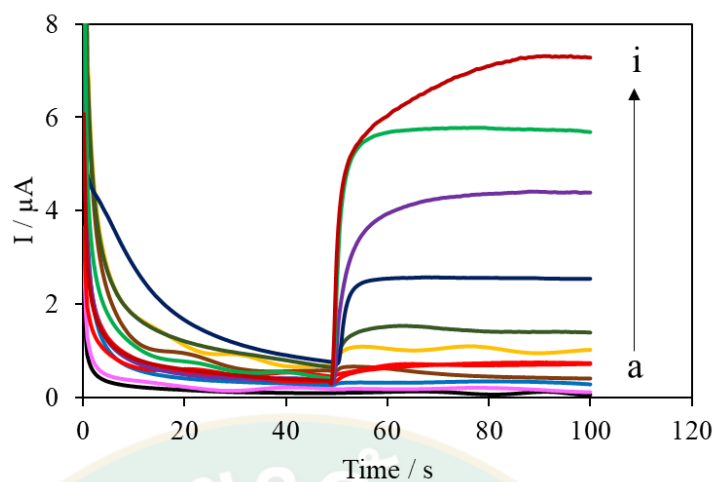
Figure 65 Amperometric response of the modified electrode towards choline

addition and calibration curve
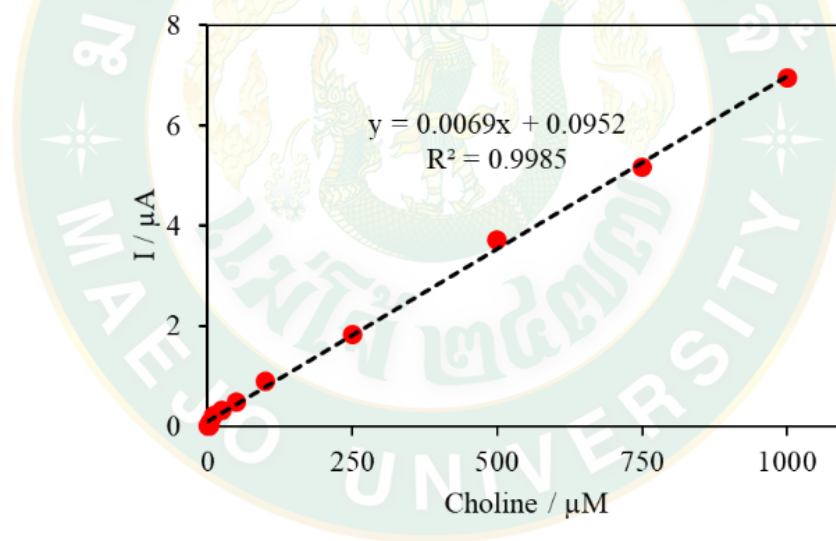
Figure 66 Amperometric response calibration curve between response current of the

modified electrode and choline concentration from 0.5 to 1,000.0 μM in 0.1 M PBS

pH 7.8.

4.2.10 Repeatability

The COx/ Cu$_2$O@MnO$_2$/ZrO$_2$@AuNPs/GCE was repetitively operated in 0.1 M phosphate buffer solution pH 7.8 by spiking 0.1 mM choline with applying amperometric technique for 7 times. The results showed acceptable % relative standard deviation as ±2.22 as presented in Table 13.

Table 13 Repeatability of the COx/Cu$_2$O@MnO$_2$/ZrO$_2$@AuNPs/GCE

No.	Current response (μA)
1	0.83
2	0.78
3	0.83
4	0.80
5	0.80
6	0.80
7	0.81
Average	0.81
Standard deviation	±0.18
% Relative standard deviation	±2.22

4.2.11 Reproducibility

All 5 Cox/Cu$_2$O@MnO$_2$/ ZrO$_2$@AuNPs/ GCEs were tested in 0.1 M phosphate buffer solution pH 7.8 by spiking 0.25 mM choline with applying amperometric technique. The results showed acceptable % relative standard deviation as ± 3.13 lower than 5% presented in Table 14.

Table 14 Reproducibility of $COx/Cu_2O@MnO_2/ZrO_2@AuNPs/GCE$

No.	Current response (µA)
1	1.64
2	1.65
3	1.60
4	1.60
5	1.53
Average	1.60
Standard deviation	±0.05
% Relative standard deviation	±3.13

4.2.12 Operation time

The operation time of the $COx/Cu_2O@MnO_2/ZrO_2@AuNPs/GCE$ was repetitively evaluated in 0.1 M phosphate buffer solution pH 7.8 by spiking 0.1 mM choline with applying amperometric technique until the current response lower than 50% of the first obtained current response. Following to the obtained result of this method, the operation time of $COx/Cu_2O@MnO_2/ZrO_2@AuNPs/GCE$ can be continuously used for 29 times as presented in Figure 67 and Table 15
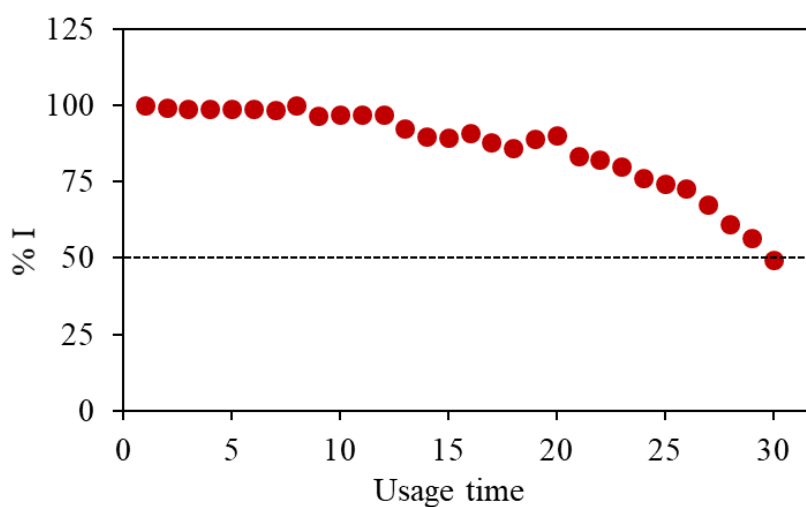
Figure 67 The operation time

Table 15 The operation time of the choline biosensor at optimal condition

Operation time (n)	I (µA)	%I	Operation time (n)	I (µA)	%I
1	0.821	100.00	16	0.754	91.85
2	0.825	100.49	17	0.730	88.92
3	0.820	99.87	18	0.714	86.96
4	0.822	100.12	19	0.738	89.92
5	0.821	100.00	20	0.748	91.18
6	0.820	99.87	21	0.693	84.45
7	0.818	99.63	22	0.681	83.02
8	0.821	100	23	0.663	80.75
9	0.800	99.55	24	0.634	77.83
10	0.803	97.89	25	0.617	75.24
11	0.804	97.97	26	0.603	73.54
12	0.803	97.89	27	0.559	68.08
13	0.766	93.41	28	0.507	61.85
14	0.746	90.93	29	0.482	57.29
15	0.742	90.42	30	0.428	49.93

4.2.13 Effect of Interferences

The COx/ $Cu_2O@MnO_2$/ $ZrO_2@AuNPs$/ GCE was examined in 0.1 M phosphate buffer solution pH 7.8 in the presence of 0.052 mg mL^{-1} choline compared to the presence of different possible interfering species such as amoxicillin, ascorbic acid, aspirin, caffeine, dopamine, glucose, sucrose and uric acid by using amperometry to obtain their minimal affecting concentrations (Signal to Noise = 3, S/N=3) as presented in Figure 68**Error! Reference source not found.** and Table 17.

Table 16 Interference effect on the choline biosensor

Interfering species	Concentration (mg mL^{-1})	Background signal (µA)	Signal (µA)	S/N	results
Amoxicillin ($C_{16}H_{19}N_3O_5S$)	0.200	0.013	0.015	1.150	inactive
	0.500	0.015	0.018	1.200	inactive
	1.000	0.015	0.020	1.330	inactive
	1.500	0.016	0.016	1.000	inactive
	2.000	0.016	0.040	2.500	inactive
Ascorbic acid ($C_6H_8O_6$)	0.600	0.011	0.020	1.818	inactive
	1.500	0.011	0.020	1.818	inactive
	3.000	0.012	0.030	2.500	inactive
	4.500	0.011	0.050	4.545	active
	6.000	0.011	0.120	10.909	active
Aspirin ($C_9H_8O_4$)	0.200	0.009	0.024	2.666	inactive
	0.500	0.010	0.005	0.500	inactive
	1.000	0.009	0.016	1.777	inactive
	1.500	0.009	0.041	4.555	active
	2.000	0.010	0.064	6.400	active
Caffeine ($C_8H_{10}N_4O_2$)	0.030	0.010	0.022	0.012	inactive
	0.080	0.010	0.025	0.015	inactive
	0.160	0.010	0.012	0.002	inactive
	0.240	0.010	0.015	0.005	inactive
	0.360	0.010	0.016	0.006	inactive
Dopamine ($C_8H_{11}NO_2$)	0.008	0.012	0.020	1.666	inactive
	0.020	0.012	0.030	2.500	inactive
	0.040	0.012	0.050	4.166	active
	0.060	0.012	0.080	6.666	active
	0.080	0.012	0.060	5.000	active

Table 16 Interference effect on the choline biosensor (continued)

Interfering species	concentration (mg mL^{-1})	Background signal (µA)	Signal (µA)	S/N	results
Glucose	0.200	0.010	0.000	0.000	inactive
(C$_6$H$_{12}$O$_6$)	0.500	0.010	0.000	0.000	inactive
	1.000	0.010	0.000	0.000	inactive
	1.500	0.010	0.000	0.000	inactive
	2.000	0.010	0.000	0.000	inactive
Sucrose	0.200	0.010	0.000	0.000	inactive
(C$_{12}$H$_{22}$O$_{11}$)	0.500	0.010	0.000	0.000	inactive
	1.000	0.010	0.000	0.000	inactive
	1.500	0.010	0.000	0.000	inactive
	2.000	0.010	0.000	0.000	inactive
Uric acid	0.120	0.011	0.011	1.000	inactive
(C$_5$H$_4$N$_4$O$_3$)	0.300	0.011	0.032	2.909	inactive
	0.600	0.011	0.067	6.090	active
	0.900	0.011	0.099	9.000	active
	1.200	0.011	0.117	10.636	active
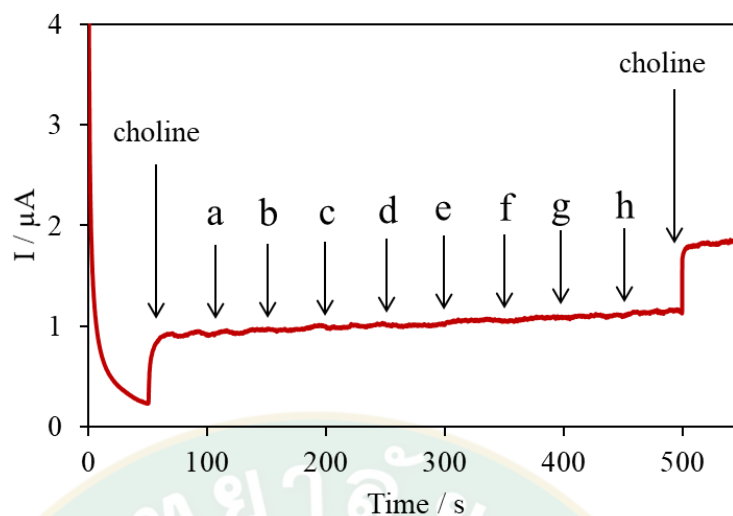
Figure 68 Interference effect on the modified electrode study (C) by spiking 0.052 mg mL^{-1} choline compared to 2.00 mg mL^{-1} amoxicillin (a) 3.00 mg mL^{-1} ascorbic acid (b) 1.00 mg mL^{-1} aspirin (c) 0.36 mg mL^{-1} caffeine (d) 0.02 mg mL^{-1} dopamine (e) 2.00 mg mL^{-1} glucose (f) 2.00 mg mL^{-1} sucrose (g) and 0.30 mg mL^{-1} uric acid (h).

Table 17 Effect of interferences

Interfering species	Minimal affecting concentration (mg mL^{-1})
Amoxicillin ($C_{16}H_{19}N_3O_5S$)	2.000
Ascorbic acid ($C_6H_8O_6$)	3.000
Aspirin ($C_9H_8O_4$)	1.000
Caffeine ($C_8H_{10}N_4O_2$)	0.360
Dopamine ($C_8H_{11}NO_2$)	0.020
Glucose ($C_6H_{12}O_6$)	2.000
Sucrose ($C_{12}H_{22}O_{11}$)	2.000
Uric acid ($C_5H_4N_4O_3$)	0.300

4.2.14 Choline analysis in real human blood samples

The COx/ Cu$_2$O@MnO$_2$/ ZrO$_2$@AuNPs/ GCE was applied to detect choline concentration in 6 blood samples by standard addition method with applying amperometric technique at the optimal condition as presented in Table 18. The results showed choline concentration between 2.6 to 18.5 µM of samples with acceptable % recovery from 97.1 to 103.9 which 5 samples were in normal choline level (5 to 20 µM) in human blood.

Table 18 Choline measurement in prepared human blood samples

Samples (n = 3)	Choline in blood (µM)	Choline added (µM)	Increased choline (µM)	Recovery (%)
Whole blood 1	18.5 ± 0.22	150.0	152.5 ± 2.61	101.70
Whole blood 2	9.9 ± 0.12	150.0	155.9 ± 1.88	103.90
Whole blood 3	2.6 ± 0.04	150.0	145.6 ± 2.11	97.10
Whole blood 4	5.8 ± 0.09	150.0	151.7 ± 1.24	101.10
Whole blood 5	18.1 ± 0.21	150.0	153.9 ± 1.76	102.70
Whole blood 6	9.8 ± 0.13	150.0	150.6 ± 1.02	100.40

CHAPTER 5

CONCLUSIONS

5.1 Hydrogen peroxide sensor

In this research, a novel, efficient, enzyme-free hydrogen peroxide sensor utilizing a modified $Cu_2O@MnO_2$ composite material was fabricated. The developed H_2O_2 sensor exhibited a wide linear range from 0.5 µM to 20 mM with a low detection limit of 63 nM (S/N= 3) and good sensitivity of 256.33 µA mM^{-1} cm^{-2}. The $Cu_2O@MnO_2$ /GCE sensor showed excellent electrochemical and satisfied kinetic performances. Also, it presented high stability, repeatability, and reproducibility. The results suggested that the simple, successful synthesis of $Cu_2O@MnO_2$ as a new platform was useful for construction of H_2O_2 sensor. This proposed method is considered for application for the development of enzyme-free H_2O_2 sensors and enzyme-based biosensors as well.

5.2 Choline biosensor

A novel sensitive and selective amperometric biosensor for choline detection has been successfully developed. The synthesized $Cu_2O@MnO_2$ and $ZrO_2@AuNPs$ synergistically enhance the performance of biosensors. The $COxCu_2O@MnO_2$/ $ZrO_2@AuNPs$/GCE presented a wide linear range, good sensitivity, high stability and selectivity. The proposed method also provided a low detection limit of choline determination comparable to earlier reported literatures. This choline biosensor based on synergistic synthesized $Cu_2O@MnO_2$ and $ZrO_2@AuNPs$ composite materials was used for the first time for choline analysis in human blood samples which exhibited acceptable quantitative measurement of choline.

REFERENCES

Ackerstaff, E., Pflug, B. R., Nelson, J. B. & Bhujwalla, Z. M. 2001. Detection of Increased Choline Compounds with Proton Nuclear Magnetic Resonance Spectroscopy Subsequent to Malignant Transformation of Human Prostatic Epithelial Cells. **Cancer Research**, 61(9), 3599.

Anjum, S., Liu, Z., Gao, W., Qi, W., Gilani, M. R. H. S., Ahmad, M., Aziz ur, R. & Xu, G. 2015. Non-enzymatic hydrogen peroxide sensor by electroreduction of p-nitrophenyl aldehyde in the presence of nitrous acid on glassy carbon electrode. **Journal of Electroanalytical Chemistry**, 750(1), 74-78.

Asif, M., Haitao, W., Shuang, D., Aziz, A., Zhang, G., Xiao, F. & Liu, H. 2017. Metal oxide intercalated layered double hydroxide nanosphere: With enhanced electrocatalyic activity towards H_2O_2 for biological applications. **Sensors and Actuators B: Chemical**, 239(1), 243-252.

Bai, Y.-H., Du, Y., Xu, J.-J. & Chen, H.-Y. 2007. Choline biosensors based on a bi-electrocatalytic property of MnO_2 nanoparticles modified electrodes to H_2O_2. **Electrochemistry Communications**, 9(10), 2611-2616.

Balık, M., Bulut, V. & Erdogan, I. Y. 2018. Optical, structural and phase transition properties of Cu_2O, CuO and Cu_2O/CuO: Their photoelectrochemical sensor applications. **International Journal of Hydrogen Energy**.

Barnard, J. P. & Stinson, M. W. 1999. Influence of environmental conditions on hydrogen peroxide formation by Streptococcus gordonii. **Infection and immunity**, 67(12), 6558-6564.

Bolat, E. Ö., Tığ, G. A. & Pekyardımcı, Ş. 2017. Fabrication of an amperometric acetylcholine esterase-choline oxidase biosensor based on MWCNTs-Fe_3O_4NPs-CS nanocomposite for determination of acetylcholine. **Journal of Electroanalytical Chemistry**, 785(1), 241-248.

Boujakhrout, A., Díez, P., Sánchez, A., Martínez-Ruíz, P., Pingarrón, J. M. & Villalonga, R. 2016. Gold nanoparticles-decorated silver-bipyridine nanobelts for the construction of mediatorless hydrogen peroxide biosensor. **Journal of Colloid**

and Interface Science, 482(1), 105-111.

Çelik Kazıcı, H., Caglar, A., Aydogmus, T., Aktas, N. & Kivrak, H. 2018. Microstructured prealloyed Titanium-Nickel powder as a novel nonenzymatic hydrogen peroxide sensor. **Journal of Colloid and Interface Science***, 530(1), 353-360.*

Chaisuksant, R., Chomsook, T., Manthong, N. & Kalcher, K. 2016. Low Cost Hydrogen Peroxide Sensor from Manganese Oxides Modified Pencil Graphite Electrode. **Procedia Chemistry***, 20(1), 81-84.*

Chen, C.-H., Njagi, E. C., Chen, S.-Y., Horvath, D. T., Xu, L., Morey, A., Mackin, C., Joesten, R. & Suib, S. L. 2015. Structural Distortion of Molybdenum-Doped Manganese Oxide Octahedral Molecular Sieves for Enhanced Catalytic Performance. **Inorganic Chemistry***, 54(21), 10163-10171.*

Chen, C., Hong, X., Xu, T., Chen, A., Lu, L. & Gao, Y. 2016. Hydrogen peroxide biosensor based on the immobilization of horseradish peroxidase onto a poly(aniline-co-N-methylthionine) film. **Synthetic Metals***, 212(1), 123-130.*

Chen, J., Gao, Y., Ma, Q., Hu, X., Xu, Y. & Lu, X. 2018. Turn-off fluorescence sensor based on the 5,10,15,20-(4-sulphonatophenyl) porphyrin (TPPS4)-Fe2+ system: Detecting of hydrogen peroxide (H_2O_2) and glucose in the actual sample. **Sensors and Actuators B: Chemical***, 268(1), 270-277.*

Chen, W., Deng, F., Xu, M., Wang, J., Wei, Z. & Wang, Y. 2018. GO/Cu_2O nanocomposite based QCM gas sensor for trimethylamine detection under low concentrations. **Sensors and Actuators B: Chemical***, 273(1), 498-504.*

Deng, K., Zhou, J. & Li, X. 2013. Noncovalent nanohybrid of ferrocene with chemically reduced graphene oxide and its application to dual biosensor for hydrogen peroxide and choline. **Electrochimica Acta***, 95(1), 18-23.*

Doretti, L., Ferrara, D., Lora, S., Schiavon, F. & Veronese, F. M. 2000. Acetylcholine biosensor involving entrapment of acetylcholinesterase and poly(ethylene glycol)-modified choline oxidase in a poly(vinyl alcohol) cryogel membrane. **Enzyme and Microbial Technology***, 27(3), 279-285.*

Dunphy, R. & Burinsky, D. J. 2003. Detection of choline and acetylcholine in a pharmaceutical preparation using high-performance liquid chromatography/electrospray ionization mass spectrometry. **Journal of**

Pharmaceutical and Biomedical Analysis, 31(5), 905-915.

Gimeno, P., Bousquet, C., Lassu, N., Maggio, A.-F., Civade, C., Brenier, C. & Lempereur, L. 2015. High-performance liquid chromatography method for the determination of hydrogen peroxide present or released in teeth bleaching kits and hair cosmetic products. *Journal of Pharmaceutical and Biomedical Analysis*, 107(1), 386-393.

Holm, P. I., Ueland, P. M., Kvalheim, G. & Lien, E. A. 2003. Determination of Choline, Betaine, and Dimethylglycine in Plasma by a High-Throughput Method Based on Normal-Phase Chromatography–Tandem Mass Spectrometry. *Clinical Chemistry*, 49(2), 286.

Honda, K., Miyaguchi, K., Nishino, H., Tanaka, H., Yao, T. & Imai, K. 1986. High-performance liquid chromatography followed by peroxyoxalate chemiluminescence detection of acetylcholine and choline utilizing immobilized enzymes. *Analytical Biochemistry*, 153(1), 50-53.

Hu, X., Goud, K. Y., Kumar, V. S., Catanante, G., Li, Z., Zhu, Z. & Marty, J. L. 2018. Disposable electrochemical aptasensor based on carbon nanotubes- V_2O_5-chitosan nanocomposite for detection of ciprofloxacin. *Sensors and Actuators B: Chemical*, 268(1), 278-286.

Hurdis, E. C. & Romeyn, H. 1954. Accuracy of Determination of Hydrogen Peroxide by Cerate Oxidimetry. *Analytical Chemistry*, 26(2), 320-325.

Jeon, B.-H., Yang, D.-H., Lee, C.-S., Kim, Y.-D. & Shin, J. S. 2018. Fabrication of silver nanoparticles in titanium dioxide/poly(vinyl alcohol) alternate thin films: A nonenzymatic hydrogen peroxide sensor application. *Electrochimica Acta*.

Kiani Shahvandi, S., Ahmar, H. & Tabatabaei Rezaei, S. J. 2018. Palladium nanoparticles immobilized on polymer-functionalized magnetic nanoparticles for the determination of hydrogen peroxide. *Surfaces and Interfaces*, 12(1), 71-77.

Kogularasu, S., Govindasamy, M., Chen, S.-M., Akilarasan, M. & Mani, V. 2017. 3D graphene oxide-cobalt oxide polyhedrons for highly sensitive non-enzymatic electrochemical determination of hydrogen peroxide. *Sensors and Actuators B: Chemical*, 253(1), 773-783.

Kok, F. N., Bozoglu, F. & Hasirci, V. 2001. Immobilization of acetylcholinesterase and choline oxidase in/on pHEMA membrane for biosensor construction. **Journal of Biomaterials Science, Polymer Edition**, 12(11), 1161-1176.

Li, B., Chen, J.-B., Xiong, Y., Yang, X., Zhao, C. & Sun, J. 2018. Development of turn-on fluorescent probes for the detection of H_2O_2 vapor with high selectivity and sensitivity. **Sensors and Actuators B: Chemical**, 268(1), 475-484.

Li, D., Meng, L., Dang, S., Jiang, D. & Shi, W. 2017. Hydrogen peroxide sensing using Cu_2O nanocubes decorated by Ag-Au alloy nanoparticles. **Journal of Alloys and Compounds**, 690(1), 1-7.

Li, S.-J., Zhang, J.-C., Li, J., Yang, H.-Y., Meng, J.-J. & Zhang, B. 2018. A 3D sandwich structured hybrid of gold nanoparticles decorated MnO_2/graphene-carbon nanotubes as high performance H_2O_2 sensors. **Sensors and Actuators B: Chemical**, 260(1), 1-11.

Li, Y., Zhang, Y., Zhong, Y. & Li, S. 2015. Enzyme-free hydrogen peroxide sensor based on Au@Ag@C core-double shell nanocomposites. **Applied Surface Science**, 347(1), 428-434.

Lin, C.-Y. & Chang, C.-T. 2015. Iron oxide nanorods array in electrochemical detection of H_2O_2. **Sensors and Actuators B: Chemical**, 220(695-704.

Lin, M., Chen, B., Wu, X., Qian, J., Fei, L., Lu, W., Chan, L. W. H. & Yuan, J. 2016. Controllable in situ synthesis of epsilon manganese dioxide hollow structure/RGO nanocomposites for high-performance supercapacitors. **Nanoscale**, 8(4), 1854-1860.

Liu, S.-Q. & Ju, H.-X. 2002. Renewable reagentless hydrogen peroxide sensor based on direct electron transfer of horseradish peroxidase immobilized on colloidal gold-modified electrode. **Analytical Biochemistry**, 307(1), 110-116.

Luo, L., Li, F., Zhu, L., Zhang, Z., Ding, Y. & Deng, D. 2012. Non-enzymatic hydrogen peroxide sensor based on MnO_2-ordered mesoporous carbon composite modified electrode. **Electrochimica Acta**, 77(1), 179-183.

Markunas, P. C. & Riddick, J. A. 1952. Titrimetry in Glacial Acetic Acid. **Analytical Chemistry**, 24(2), 312-313.

Marquette, C. A., Degiuli, A., Blum, L., x & c, J. 2003. Electrochemiluminescent

biosensors array for the concomitant detection of choline, glucose, glutamate, lactate, lysine and urate. **Biosensors and Bioelectronics**, 19(5), 433-439.

Moonla, C., Preechaworapun, A. & Tangkuaram, T. 2017. A Single Drop Fabrication of the Cholesterol Biosensor Based on Synthesized $NiFe_2O_4$NPs Dispersed on PDDA-CNTs. **Electroanalysis**, 29(12), 2698-2707.

Mutyala, S. & Mathiyarasu, J. 2016. A reagentless non-enzymatic hydrogen peroxide sensor presented using electrochemically reduced graphene oxide modified glassy carbon electrode. **Materials Science and Engineering: C**, 69(1), 398-406.

Näther, N., Juárez, L. M., Emmerich, R., Berger, J., Friedrich, P. & Schöning, M. J. 2006. Detection of Hydrogen Peroxide (H(2)O(2)) at Exposed Temperatures for Industrial Processes. **Sensors (Basel, Switzerland)**, 6(4), 308-317.

Nestor, P. J., Scheltens, P. & Hodges, J. R. 2004. Advances in the early detection of Alzheimer's disease. **Nature Medicine**, 10(1), 34.

Nitsch, R. M., Blusztajn, J. K., Pittas, A. G., Slack, B. E., Growdon, J. H. & Wurtman, R. J. 1992. Evidence for a membrane defect in Alzheimer disease brain. **Proceedings of the National Academy of Sciences**, 89(5), 1671.

Ohkawa, R., Kurano, M., Sakai, N., Kishimoto, T., Nojiri, T., Igarashi, K., Hosogaya, S., Ozaki, Y., Dohi, T., Miyauchi, K., Daida, H., Aoki, J., Okubo, S., Ikeda, H., Tozuka, M. & Yatomi, Y. 2018. Measurement of plasma choline in acute coronary syndrome: importance of suitable sampling conditions for this assay. **Scientific reports**, 8(1), 4725-4725.

Ouiram, T., Moonla, C., Preechaworapun, A. & Tangkuaram, T. 2019. Enzyme-free $Cu_2O@MnO_2$/GCE for hydrogen peroxide sensing. **Electroanalysis**, 31(7), 1356-1362.

Penry, J. T. & Manore, M. M. 2008. Choline: An Important Micronutrient for Maximal Endurance-Exercise Performance? **International Journal of Sport Nutrition and Exercise Metabolism**, 18(2), 191-203.

Pourfaraj, R., Kazemi, S. Y., Fatemi, S. J. & Biparva, P. 2018. Synthesis of **α**- and **β**-CoNi binary hydroxides nanostructures and luminol chemiluminescence study for H_2O_2 detection. **Journal of Photochemistry and Photobiology A:**

Chemistry, 364(1), 534-541.

Qi, C. & Zheng, J. 2015. Novel nonenzymatic hydrogen peroxide sensor based on Fe$_3$O$_4$/PPy/Ag nanocomposites. **Journal of Electroanalytical Chemistry,** 747(1), 53-58.

Qin, X., Wang, H., Miao, Z., Li, J. & Chen, Q. 2015. A novel non-enzyme hydrogen peroxide sensor based on catalytic reduction property of silver nanowires. **Talanta,** 139(56-61.

Qu, F., Yang, M., Jiang, J., Shen, G. & Yu, R. 2005. Amperometric biosensor for choline based on layer-by-layer assembled functionalized carbon nanotube and polyaniline multilayer film. **Analytical Biochemistry,** 344(1), 108-114.

Rahman, M. A., Park, D.-S. & Shim, Y.-B. 2004. A performance comparison of choline biosensors: anodic or cathodic detections of H$_2$O$_2$ generated by enzyme immobilized on a conducting polymer. **Biosensors and Bioelectronics,** 19(12), 1565-1571.

Razola, S. S., Pochet, S., Grosfils, K. & Kauffmann, J. M. 2003. Amperometric determination of choline released from rat submandibular gland acinar cells using a choline oxidase biosensor. **Biosensors and Bioelectronics,** 18(2), 185-191.

Reddy, G. R. K., Hyder, M. & Kumar, P. S. 2017. Facile Preparation of High-Performance Copper Oxide Sensors for Electroanalysis of Hydrogen Peroxide. **Materials Today: Proceedings,** 4(13), 12457-12469.

Ren, X., Tang, F., Liao, R. & Zhang, L. 2009. Using gold nanorods to enhance the current response of a choline biosensor. **Electrochimica Acta,** 54(28), 7248-7253.

Řičný, J., Tuček, S. & Vinš, I. 1992. Sensitive method for HPLC determination of acetylcholine, choline and their analogues using fluorometric detection. **Journal of Neuroscience Methods,** 41(1), 11-17.

Roushani, M. & Dizajdizi, B. Z. 2015. Development of nonenzymatic hydrogen peroxide sensor based on catalytic properties of copper nanoparticles/Rutin/MWCNTs/IL/Chit. **Catalysis Communications,** 69(1), 133-

137.

Salehabadi, A. & Enhessari, M. (2019). Chapter 11 - Application of (mixed) metal oxides-based nanocomposites for biosensors. In V. Grumezescu และA. M. Grumezescu (Eds.), **Materials for Biomedical Engineering** (Vol. 1, pp. 357-396): Elsevier.

Sekar, N. C., Ge, L., Mousavi Shaegh, S. A., Ng, S. H. & Tan, S. N. 2015. A mediated turnip tissue paper-based amperometric hydrogen peroxide biosensor. **Sensors and Actuators B: Chemical**, 210(1), 336-342.

Shimomura, T., Itoh, T., Sumiya, T., Mizukami, F. & Ono, M. 2009. Amperometric determination of choline with enzyme immobilized in a hybrid mesoporous membrane. **Talanta**, 78(1), 217-220.

Shu, Y., Xu, J., Chen, J., Xu, Q., Xiao, X., Jin, D., Pang, H. & Hu, X. 2017. Ultrasensitive electrochemical detection of H2O2 in living cells based on ultrathin MnO_2 nanosheets. **Sensors and Actuators B: Chemical**, 252(1), 72-78.

Sinhamahapatra, A., Jeon, J.-P., Kang, J., Han, B. & Yu, J.-S. 2016. Oxygen-Deficient Zirconia (ZrO_2-x): A New Material for Solar Light Absorption. **Scientific Reports**, 6(1), 27218.

Song, H., Zhao, H., Zhang, X., Xu, Y., Cheng, X., Gao, S. & Huo, L. 2019. 3D hierarchical hollow hydrangea-like Fe^{3+}@Ɛ-MnO_2 microspheres with excellent electrochemical performance for dopamine and hydrogen peroxide. **Biosensors and Bioelectronics**, 133(1), 250-257.

Stadler, H. & Nesselhut, T. 1986. Simple and rapid measurement of acetylcholine and choline by HPLC and enzymatic-electrochemical detection. **Neurochemistry International**, 9(1), 127-129.

Su, Y., Guo, H., Wang, Z., Long, Y., Li, W. & Tu, Y. 2018. Au@Cu_2O core-shell structure for high sensitive non-enzymatic glucose sensor. **Sensors and Actuators B: Chemical**, 255(1), 2510-2519.

Tizfahm, J., Aghazadeh, M., Maragheh, M. G., Ganjali, M. R., Norouzi, P. & Faridbod, F. 2016. Electrochemical preparation and evaluation of the supercapacitive performance of MnO_2 nanoworms. **Materials Letters**, 167(1), 153-156.

Van Zoonen, P., Gooijer, C., Velthorst, N. H., Frei, R. W., Wolf, J. H., Gerrits, J. & Flentge, F. 1987. HPLC detection of choline and acetylcholine in serum and urine by an immobilized enzyme reactor followed by chemiluminescence detection. **Journal of Pharmaceutical and Biomedical Analysis**, 5(5), 485-492.

Vukojević, V., Djurdjić, S., Ognjanović, M., Fabián, M., Samphao, A., Kalcher, K. & Stanković, D. M. 2018. Enzymatic glucose biosensor based on manganese dioxide nanoparticles decorated on graphene nanoribbons. **Journal of Electroanalytical Chemistry**, 823(1), 610-616.

Wang, J. 1999. Electroanalysis and Biosensors. **Analytical Chemistry**, 71(12), 328-332.

Wang, J., Liu, G. & Lin, Y. 2006. Amperometric choline biosensor fabricated through electrostatic assembly of bienzyme/polyelectrolyte hybrid layers on carbon nanotubes. **Analyst**, 131(4), 477-483.

Wang, M., Jiang, X., Liu, J., Guo, H. & Liu, C. 2015. Highly sensitive H_2O_2 sensor based on Co3O4 hollow sphere prepared via a template-free method. **Electrochimica Acta**, 182(1), 613-620.

Wang, M., Kang, M., Guo, C., Fang, S., He, L., Jia, C., Zhang, G., Bai, B., Zong, W. & Zhang, Z. 2015. Electrochemical biosensor based on Cu/Cu_2O nanocrystals and reduced graphene oxide nanocomposite for sensitively detecting ractopamine. **Electrochimica Acta**, 182(1), 668-675.

Wang, W., Guo, H. T., Gao, J. P., Dong, X. H. & Qin, Q. X. 2000. XPS, UPS and ESR studies on the interfacial interaction in Ni-ZrO_2 composite plating. **Journal of Materials Science**, 35(6), 1495-1499.

Wen, X., Long, M. & Tang, A. 2017. Flake-like Cu_2O on TiO_2 nanotubes array as an efficient nonenzymatic H_2O_2 biosensor. **Journal of Electroanalytical Chemistry**, 785(1), 33-39.

Wise, D. D., Barkhimer, T. V., Brault, P.-A., Kirchhoff, J. R., Messer, W. S. & Hudson, R. A. 2002. Internal standard method for the measurement of choline and acetylcholine by capillary electrophoresis with electrochemical detection. **Journal of Chromatography B**, 775(1), 49-56.

Wu, B., Ou, Z., Ju, X. & Hou, S. 2011. Carbon Nanotubes/Gold Nanoparticles Composite Film for the Construction of a Novel Amperometric Choline

Biosensor. **Journal of Nanomaterials**, 2011(1), 6.

Wu, L., Zhang, X., Wang, M., He, L. & Zhang, Z. 2018. Preparation of Cu_2O/CNTs composite and its application as sensing platform for detecting nitrite in water environment. **Measurement**, 128(1), 189-196.

Yan, Q., Wang, Z., Zhang, J., Peng, H., Chen, X., Hou, H. & Liu, C. 2012. Nickel hydroxide modified silicon nanowires electrode for hydrogen peroxide sensor applications. **Electrochimica Acta**, 61(1), 148-153.

Yáñez-Sedeño, P. & Pingarrón, J. M. 2005. Gold nanoparticle-based electrochemical biosensors. **Analytical and Bioanalytical Chemistry**, 382(4), 884-886.

Yang, M., Yang, Y., Yang, Y., Shen, G. & Yu, R. 2004. Bienzymatic amperometric biosensor for choline based on mediator thionine in situ electropolymerized within a carbon paste electrode. **Analytical Biochemistry**, 334(1), 127-134.

Yang, Y., Yang, H., Yang, M., liu, Y., Shen, G. & Yu, R. 2004. Amperometric glucose biosensor based on a surface treated nanoporous ZrO_2/Chitosan composite film as immobilization matrix. **Analytica Chimica Acta**, 525(2), 213-220.

Yang, Y., Zhao, J., Qin, L., Yin, Y. & He, L. 2016. Synthesis of ordered bowl-like Cu-Cu_2O array film for non-enzymatic hydrogen peroxide sensor. **Materials Letters**, 179(1), 27-29.

Yin, H., Cui, Z., Wang, L. & Nie, Q. 2016. In situ reduction of the Cu/Cu_2O/carbon spheres composite for enzymaticless glucose sensors. **Sensors and Actuators B: Chemical**, 222(1), 1018-1023.

Yu, C.-C., Chen, M.-H., Lu, C.-H., Huang, Y.-C., Chen, H.-L., Tsai, N.-W., Wang, H.-C., Yang, I.-H., Li, S.-H. & Lin, W.-C. 2016. Altered Striatocerebellar Metabolism and Systemic Inflammation in Parkinson’s Disease. **Oxidative Medicine and Cellular Longevity**, 2016(1), 12.

Yu, C., Cui, J., Wang, Y., Zheng, H., Zhang, J., Shu, X., Liu, J., Zhang, Y. & Wu, Y. 2018. Porous HKUST-1 derived CuO/Cu_2O shell wrapped $Cu(OH)_2$ derived CuO/Cu_2O core nanowire arrays for electrochemical nonenzymatic glucose sensors with ultrahigh sensitivity. **Applied Surface Science**, 439(1), 11-17.

Yu, Z., Li, H., Zhang, X., Liu, N. & Zhang, X. 2015. NiO/graphene nanocomposite for determination of H_2O_2 with a low detection limit. **Talanta**, 144(1), 1-5.

Zamfir, L.-G., Rotariu, L., Marinescu, V. E., Simelane, X. T., Baker, P. G. L., Iwuoha, E. I. & Bala, C. 2016. Non-enzymatic polyamic acid sensors for hydrogen peroxide detection. **Sensors and Actuators B: Chemical**, 226(1), 525-533.

Zeisel, S. H. 1992. Choline: an important nutrient in brain development, liver function and carcinogenesis. **Journal of the American College of Nutrition**, 11(5), 473-481.

Zeisel, S. H. 2004. Nutritional Importance of Choline for Brain Development. **Journal of the American College of Nutrition**, 23(sup6), 621S-626S.

Zeisel, S. H. & da Costa, K.-A. 2009. Choline: an essential nutrient for public health. **Nutrition reviews**, 67(11), 615-623.

Zeisel, S. H. & daCosta, K. A. 1990. Choline: Determination using gas chromatography/mass spectrometry. **The Journal of Nutritional Biochemistry**, 1(1), 55-59.

Zhang, L., Yin, S., Hou, J., Zhang, W., Huang, H., Li, Y. & Yu, C. 2019. Detection of choline and hydrogen peroxide in infant formula milk powder with near infrared upconverting luminescent nanoparticles. **Food Chemistry**, 270(1), 415-419.

Zhang, R. & Chen, W. 2017. Recent advances in graphene-based nanomaterials for fabricating electrochemical hydrogen peroxide sensors. **Biosensors and Bioelectronics**, 89(1), 249-268.

Zhang, X., Bi, X., Di, W. & Qin, W. 2016. A simple and sensitive $Ce(OH)CO_3/H_2O_2$/TMB reaction system for colorimetric determination of H2O2 and glucose. **Sensors and Actuators B: Chemical**, 231(1), 714-722.

Zhang, Z., Wang, X. & Yang, X. 2011. A sensitive choline biosensor using Fe_3O_4 magnetic nanoparticles as peroxidase mimics. **Analyst**, 136(23), 4960-4965.

Zhou, J., Min, M., Liu, Y., Tang, J. & Tang, W. 2018. Layered assembly of NiMn-layered double hydroxide on graphene oxide for enhanced non-enzymatic sugars and hydrogen peroxide detection. **Sensors and Actuators B: Chemical**, 260(1), 408-417.

APPENDIX

APPENIX A

PUBLICATION

Full Paper

Enzyme-free Cu$_2$O@MnO$_2$/GCE for Hydrogen Peroxide Sensing

Tik Ouiram,[a] Chochanon Moonla,[a] Anchana Preechaworapun,[b] and Tanin Tangkuaram*[c]

Abstract: A novel composite material of copper (I) oxide at manganese (IV) oxide (Cu$_2$O@MnO$_2$), was synthesized and applied for modification on the glassy carbon electrode (GCE) surface (Cu$_2$O@MnO$_2$/GCE) as a hydrogen peroxide (H$_2$O$_2$) sensor. The composite material was characterized regarding its structural and morphological properties, using field emission scanning electron microscopy (FE-SEM), energy-dispersive X-ray spectroscopy (EDX), X-ray diffraction (XRD) and Fourier transform infrared spectroscopy (FTIR). The Cu$_2$O@MnO$_2$/GCE showed an excellent electrocatalytic response to the oxidation of H$_2$O$_2$ which provided a 0.56 s^{-1} charge transfer rate constant (K_s), 1.65×10^{-5} cm^2 s^{-1} diffusion coefficient value (D), 0.12 mm^2 electroactive surface area (A_e) and 1.04×10^{-8} mol cm^{-2} surface concentration (γ). At the optimal condition, the constructed sensor exhibited a wide linear range from 0.5 μM to 20 mM with a low limit of detection (63 nM, (S/N = 3) and a good sensitivity of 256.33 μA mM^{-1} cm^{-2}. It also presented high stability ($\Delta I_{response} \pm 15\%$, n = 100), repeatability (1.25 % RSD, n = 10) and reproducibility (3.55 % RSD, n = 10). The results indicated that the synthesized Cu$_2$O@MnO$_2$ was successfully used as a new platform for H$_2$O$_2$ sensing.

Keywords: Hydrogen peroxide sensor · Composite materials · Cu$_2$O@MnO$_2$

1 Introduction

Throughout the past few decades, the development of devices for hydrogen peroxide (H$_2$O$_2$) measurement has been increasingly interesting because hydrogen peroxide plays an important role in environmental, industrial and clinical uses [1]. Moreover, it is a byproduct of a large number of oxidase enzymes such as glucose oxidase, cholesterol oxidase, cholinesterase and lactase in biochemical reactions [2]. Accordingly, there is a huge demand and thus multiple attempts to enhance H$_2$O$_2$ determination to be rapid, efficient and low-cost. Up to now, various analytical techniques for H$_2$O$_2$ detection have been reported such as chemiluminescence [3], chromatography [4], colorimetry [5], fluorescence [6], spectrophotometry [7] and titrimetry [8]. However, electrochemistry has superior advantages in terms of excellent selectivity, high sensitivity, stability, instrumentation cost, efficiency and ease of operation [9].

Enzyme-based biosensors have been widely developed and applied, owing to their excellent sensitivity and high selectivity [10], in the last few years. However, the poor intrinsic stability of enzymes significantly affects their biological function and lifetime usage of enzyme-based biosensors [11]. In addition, immobilization techniques, denaturation, and storage stability effecting the biological activity of enzymes restrict their applications [12]. In order to overcome these issues, enzyme-free sensors have been designed with modified materials towards the goal of minimizing the drawbacks of traditional enzymatic sensors [13]. Recently, metal oxide materials such as Co [14], Ni [15], Fe [16], Cu [17] and Mn [18] have been used in sensor applications due to their attractive dominant properties including large surface area, long-term stability, catalytic efficiency and excellent conductivity [19]. Also, their metal oxide composite materials outstandingly enhance the electrochemical performances of the sensor [20].

Among various metal oxides, cuprous oxide (Cu$_2$O), an easily-obtained, intrinsic p-type semiconductor with a band gap of 2.17 eV [21], has been used in many applications such as photovoltaic [22], photocatalysis and solar cells [23]. It has also been applied in electrochemical sensing [24] and related fields because of its electrocatalytic activity, low environmental impact, and low cost. Unfortunately, these interesting particular properties are limited by its inherent poor conductivity which can affect to the charge transfer of sensor [25]. For example, manganese dioxide (MnO$_2$), an important transition metal oxide, has been used as a modified material for batteries, supercapacitors, and sensors [26] due to its advantages of excellent catalytic activity, abundant availability, absorp-

[a] T. Ouiram, C. Moonla
Applied Chemistry Program, Faculty of Science, Maejo University, Chiang Mai 50290, Thailand
[b] A. Preechaworapun
Chemistry Program, Faculty of Science and Technology, Pibulsongkram Rajabhat University, Phitsanulok 65000, Thailand
[c] T. Tangkuaram
Chemistry Program, Faculty of Science, Maejo University, Chiang Mai 50290, Thailand
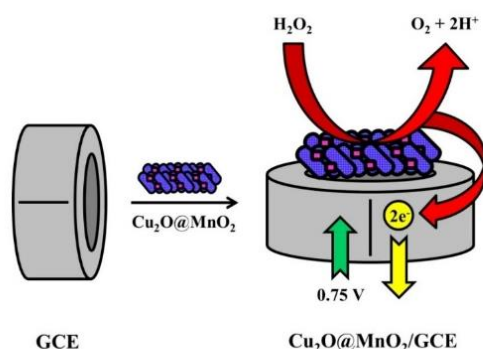E-mail: tanin.tang@gmail.com

Full Paper

Fig. 1. Schematic illustration of the simple step fabrication of enzyme-free H_2O_2 sensor and its proposed electrochemical reaction.

tion ability, low toxicity and low cost [1b,27]. However, the challenging issue remains owing to poor conductivity of MnO_2. Thus, for the first time, the novel synergetic $Cu_2O@MnO_2$ composite materials modified GCE surface for enhancement of enzyme-free H_2O_2 sensing was developed as shown in Figure 1. Moreover, the simple and direct drop casting of $Cu_2O@MnO_2$ was presented.

2 Experimental

2.1 Materials

Analytical grade reagents and solvents without further purification process and Ultra-high purity water (UHP) by Milli-Q Advantage A10 Water Purification System (France) were used for all experiments in this research. Ascorbic acid, chitosan (CHIT), copper (II) sulfate pentahydrate, ethanol, glucose, manganese (II) sulfate monohydrate, potassium hexacyanoferrate (III), potassium permanganate, sucrose, and uric acid were purchased from Sigma-Aldrich Co. LLC (St. Louis, USA). Hydrogen peroxide (30 %) was provided by Merck (Darmstadt, Germany). Nitric acid was purchased from QRëc, New Zealand. A Glutaraldehyde solution (GA) (50.0 %) was obtained from Fluka (St. Louis, USA). Dipotassium hydrogen orthophosphate was purchased from Fisher Scientific (New Hampshire, USA) and potassium dihydrogen orthophosphate was provided by Rankem (Haryana, India). A Potassium chloride solution (3 M) was obtained from Metrohm (Herisau, Switzerland).

A Field Emission Scanning Electron Microscope (JEOL JSM-6335F, USA), X-ray diffractometer (Rigaku MiniFlex II, Japan) and a Fourier Transform Infrared Spectrometer (PerkinElmer model Spectrum RX I, Perkin-Elmer, England) were used for characterization of the synthesized $Cu_2O@MnO_2$ composite materials compared to the synthesized MnO_2 particles. CH instruments (CH 1230, USA) were used for all electrochemical measure-

ments. A Ag/AgCl electrode (3 M KCl) as a reference electrode, GCE (3 mm diameter) as a working electrode and Pt wire electrode (2 mm diameter) as a counter electrode were operated as a three-electrode system using cyclic voltammetric (CV) and amperometric techniques in 5 mL of 0.05 M phosphate buffer solution (PBS, pH 7.2) at room temperature.

2.2 Synthesis of $Cu_2O@MnO_2$

The $Cu_2O@MnO_2$ composite materials was synthesized using the single-step reflux method which was adjusted from the earlier report [28]. First, a 0.32 M $KMnO_4$ solution was prepared and then $CuSO_4 \cdot 5H_2O$ was added into 100 mL of the 0.32 M $KMnO_4$ solution (stoichiometric ratio of Cu : Mn as 1 : 5) – Solution A. After that, 50 mL of a 0.88 M $MnSO_4$ solution was prepared and then 8.5 mL HNO_3 was added – Solution B. Solution B was added drop-wise into Solution A under continuous stirring. This resulted in the formation of a dark precipitate. The resultant slurry was refluxed at 120 degrees Celsius for 12 hours, then washed and dried at 120 degrees Celsius for 12 hours. Finally, the obtained $Cu_2O@MnO_2$ powder was kept in a desiccator at room temperature for further work. The MnO_2 powder was also synthesized, without adding $CuSO_4 \cdot 5H_2O$ into solution A, using the same method of $Cu_2O@MnO_2$ synthesis.

2.3 Preparation of the $Cu_2O@MnO_2/GCE$ Sensor

The synthesized $Cu_2O@MnO_2$ composite materials powder was added and sonicated in 0.5 % CHIT crosslinked 0.5 % glutaraldehyde (stoichiometric ratio of CHIT:GA as 1 : 200) solution, respectively. Afterward, 20 μL of well-dispersed $Cu_2O@MnO_2$ composite materials was dropped onto the clean glassy carbon electrode surface and dried under room temperature. The complete $Cu_2O@MnO_2/GCE$ as the H_2O_2 sensor was kept in a desiccator at room temperature. The MnO_2/GCE sensor was constructed using the same procedure as the aforementioned.

3 Results and Discussion

3.1 Characterization of Synthesized Materials

To characterize and confirm the synthesized materials, MnO_2 and $Cu_2O@MnO_2$ were studied and compared using various techniques. The SEM images of MnO_2 and $Cu_2O@MnO_2$ are shown in Figure 2 A(a) and 2B(a), respectively. The MnO_2 showed rod shape with a diameter of 2 μm while the $Cu_2O@MnO_2$ showed the mixture of the rod (diameter 1 μm) and flake (wide 5 μm) shapes. Also, the difference between MnO_2 and $Cu_2O@MnO_2$ and their qualitative compositions was confirmed with the presence of elements such as manganese, potassium, and oxygen from MnO_2 EDX pattern (Figure 2. A(b)) while the copper was additionally added in $Cu_2O@MnO_2$ (Figure 2. B(b)).
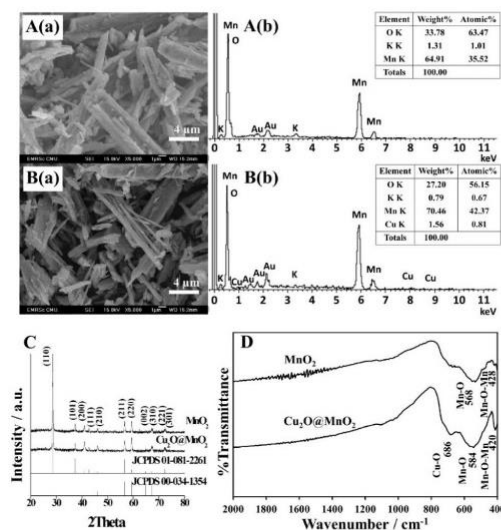
Full Paper

Fig. 2. SEM images (A(a), B(a)), EDX spectra (A(b), B(b)), XRD patterns (C) and FTIR spectra (D) of synthesized materials MnO_2 compared to $Cu_2O@MnO_2$.

Fig. 3. Cyclic voltammograms of the bare GCE (A) MnO_2/GCE (B) and $Cu_2O@MnO_2$/GCE (C) in 0.05 M PBS pH 7.2 (a) and in 0.05 M PBS containing 0.5 mM H_2O_2 (b) at a scan rate of 50 mV s^{-1}.

Additionally, XRD patterns (Figure 2C) presented structural and morphological features as the crystalline natures of MnO_2 and $Cu_2O@MnO_2$. The XRD pattern of MnO_2 was indexed as (110), (101), (200), (111), (210), (211), (220), (002), (310), (221) and (301) planes of tetragonal MnO_2 crystal system (JCPDS no. 01-081-2261). Compared to the synthesized $Cu_2O@MnO_2$, the presence of cubic Cu_2O crystal phase of the composite materials was confirmed corresponding to the planes (110), (111), (200), (220) and (311) (JCPDS no.00-034-1354). The FTIR result of MnO_2 and $Cu_2O@MnO_2$ are shown in Figure 2D. The bands of the MnO_2 spectrum at 568 and 428 cm^{-1} could be attributed to Mn–O and Mn–O–Mn lattice vibration, respectively. Compared to $Cu_2O@MnO_2$, the bands of the spectrum at 686, 584 and 420 cm^{-1} corresponded to Cu(I)–O, Mn–O and Mn–O–Mn, respectively, which was in good agreement with previous reports [29].

3.2 Electrochemical Behavior of the Modified Electrodes

To study the electrochemical performance, the cyclic voltammetric technique or CV was utilized to consider the electrocatalytic activity and properties of synthesized composite materials modified onto GCE surface. The CV was operated in the absence and presence of 0.5 mM H_2O_2 in 0.05 M PBS pH 7.2, and in the potential range from 0 to 1.0 V. Figure 3 showed the cyclic voltammograms of two different kinds of modified electrodes, MnO_2/GCE and $Cu_2O@MnO_2$/GCE compared to bare GCE. In Figure 3 A, the bare GCE yielded similar cyclic voltammograms with both absence (a) and presence (b) of

H_2O_2. In contrast to the MnO_2/GCE in Figure 3B, it presented a cyclic voltammogram with obviously different curves of H_2O_2 oxidation (b) about 0.70 to 1.0 V, and obtained the current height of 4.73 μA at +0.90 V compared to a cyclic voltammogram with the absence of H_2O_2 (a) with the current at 2.53 μA, measured at the same potential. It can be suggested that the synthesized MnO_2 acts as an electrocatalytic mediator resulting in enhancement of electron transfer from H_2O_2 electrochemical reaction onto the working electrode surface corresponding to earlier reports [30]. However, when the GCE modified with $Cu_2O@MnO_2$ as the $Cu_2O@MnO_2$/GCE was operated at the same condition, it exhibited a dominant H_2O_2 oxidation curve (Figure 3 C, b) from 0.60 to 1.0 V. The obtained current from $Cu_2O@MnO_2$/GCE was highest for 12.89 μA at 0.90 V and compared to a small oxidation curve of absence H_2O_2 (Figure 3 C, a). The current ratio of $Cu_2O@MnO_2$/GCE over Cu_2O/GCE for H_2O_2 oxidation property is 2.73 times. These electrocatalytic oxidation phenomena result from the manganese (IV) that can oxidize H_2O_2 to O_2 at the positive potential. From these results, it was assumed that the Cu_2O supported an electrocatalytic property of MnO_2 as the novel bimetallic $Cu_2O@MnO_2$ composite materials in a synergetic way due to its significant catalytic activity as well [31].

In order to study its electrochemical behavior and explain its kinetics, the $Cu_2O@MnO_2$/GCE was also operated in the 2 mM $K_3Fe(CN)_6$ containing 0.1 M KCl at various scan rates in the range of 25 to 150 mV s^{-1} as shown in the cyclic voltammograms in Figure 4. Following to the obtained linear relationships between peak current responses and the square root of the scan rates as shown in the inset of Figure 4, it was provided a diffusion-controlled quasi-reversible process of associated redox processes [32]. Moreover, the kinetic parameters such as charge transfer rate constant (K_s), diffusion coefficient value (D), electroactive surface area (A_e) and surface concentration (γ) can be calculated as 0.56 s^{-1}, 1.65×10^{-5} cm^2 s^{-1}, 0.12 mm^2 and 1.04×10^{-8} mol cm^{-2}, respectively. K_s value was calculated using the Laviron equation [33], D and A_e values obtained by Randles-Sevcik equations [34], while γ gained using Brown – Anson model [35].

Full Paper
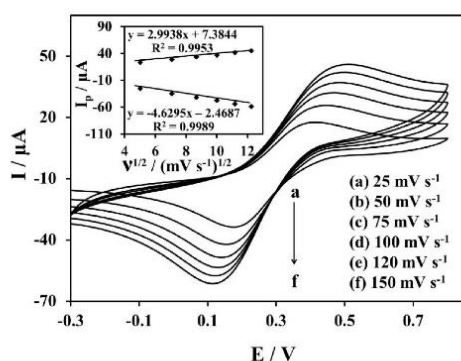
Fig. 4. Cyclic voltammograms of the $Cu_2O@MnO_2$/GCE at various scan rates; 25 (a) 50 (b) 75 (c) 100 (d) 120 (e) and 150 (f) mV s^{-1} in 2 mM $K_3Fe(CN)_6$ containing 0.1 M KCl. The inset shows the relationship plot between the current response versus the square root of scan rate (25–150 mV s^{-1}).

3.3 Optimization of Experimental Parameters

To obtain the maximum efficient performance of the fabricated $Cu_2O@MnO_2$/GCE sensor for H_2O_2 detection towards the oxidation reaction, it is very important to optimize the experimental condition by examination of major factors such as the applied potential, pH and the concentration of $Cu_2O@MnO_2$. The applied potential is one of the important factors which must be considered because it can affect the electrochemical properties of the developed sensor, especially sensitivity and selectivity, for H_2O_2 amperometric determination. Thus, the $Cu_2O@MnO_2$/GCE was studied by spiking 0.5 mM H_2O_2 at various applied potentials in the range of 0.60 to 0.90 V corresponding to H_2O_2 oxidation reaction curve. As

shown in Figure 5 A, the best current response was obtained at 0.75 V compared to the others at different potentials. So, the applied potential value of 0.75 V was chosen for further work. Besides the applied potentials, the current response can be affected by the pH of electrolyte solution in the experimental system leading to the difference in activity and stability of the modified electrode [36]. To obtain a proper pH solution (0.05 M PBS), the current response of the $Cu_2O@MnO_2$/GCE was investigated in the pH solution range from 6.0 to 8.0 in Figure 5B. The results showed that the current response linearly increased at pH from 6.0 to 7.0 and dominantly increased at pH 7.2. After that, the current response slightly decreased at higher pH from 7.4 to 8.0. Therefore, a 0.05 M PBS solution of pH 7.2 was determined suitable for this experiment.
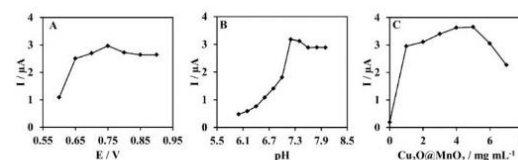
Fig. 5. The influence of applied potential (A) pH loading (B) and $Cu_2O@MnO_2$ concentration (C) on the $Cu_2O@MnO_2$/GCE in 0.05 M PBS pH 7.2 containing 0.5 mM H_2O_2 using the amperometric technique.

Moreover, the effect of $Cu_2O@MnO_2$ concentration on the electrochemical performance of the sensor was examined from 0 to 7 mg mL^{-1}. As can be seen in Figure 5 C, the current response increased from 0 to 4 mg mL^{-1} of $Cu_2O@MnO_2$ composite materials and it hardly changed from 4 to 5 mg mL^{-1}. Then, the current

Table 1. Comparison of H_2O_2 sensors.

Sensors	Detection techniques	Voltage/ V	LOD/ nM	Linearity/ mM	K_s/ s^{-1}	Sensitivity/ $\mu A\,mM^{-1}cm^{-2}$	Ref.
MnO_2/GO/GCE	BA	−0.30	800	0.005–0.6	NA	38.2	[39]
Mn-complex/SWCNTs/GCE	BA	−0.30	200	0.001–1.5	48.84	692	[40]
Chit-MWNTs/Hb/Au@Au$_2$S$_2$O$_3$/ GCE	BA	−0.30	3,200	0.04–0.72	1.30	NA	[41]
RF/RuOx/GCE	BA	−0.41	150	0.00015–3	16.8	4,458.60	[42]
GR-AuNRs/GCE	BA	−0.55	10,000	0.03–5	NA	389.2	[43]
rGO/Fe$_2$O$_3$/GCE	BA	−0.60	6,000	0.05–9	0.52	NA	[44]
MNPs/MWFNTs-GS/GCE	BA	−0.24	800	0.002–8.44	NA	206.3	[45]
MB/GQDs-CS/GCE	BA	−0.60	700	0.001–11.78	2.87	1,287.90	[46]
N-SEGN/GCE	BA	−0.40	880	0.01–2.225	NA	231.3	[47]
$Cu_2O@MnO_2$/GCE	BA	0.75	63	0.0005–20	0.56	256.33	TW

AuNRs = Gold nanorods, BA = Batch amperometry, Chit = Chitosan, CS = Chitosan, GCE = Glassy carbon electrode, GO = Graphene oxide, GQDs = Graphene quantum dots, GR = Graphene, GS = Graphene, Hb = Hemoglobin, K_s = charge transfer rate constant, LOD = Limit of detection, MB = Methylene blue, MNPs = MnO_2 nanoparticles, MWCNTs = Multi-walled carbon nanotubes, MWFNTs = Multi-walled fullerene nanotubes, NA = Not available, N-SEGN = Nitrogen-doped graphene nanosheet, RF = Riboflavin, rGO = Reduced graphene oxide, RuOx = Ruthenium oxide, SWCNTs = Single wall carbon nanotubes, TW = This work.

Full Paper

response clearly decreased at higher concentrations because of increasing resistance and decreased electron transfer onto the electrode surface from the effect of the high resistance of composite materials at high thickness [37]. Thus, 4 mg mL^{-1} of Cu$_2$O@MnO$_2$ was used for further study.

3.4 Amperometric H$_2$O$_2$ Determination

To investigate the H$_2$O$_2$ detection, the Cu$_2$O@MnO$_2$/GCE sensor was operated with H$_2$O$_2$ addition for the study of linearity using the amperometric technique at the obtained optimal condition as discussed in section 3.3. Figure 6 presents the amperometric response of the modified electrode with successive addition of H$_2$O$_2$ into 0.05 M PBS pH 7.2 at 0.75 V under continuous stirring (A) and the linear relation of response current and H$_2$O$_2$ concentration (B). The results showed that the current response of the sensor proportionally increased with increasing H$_2$O$_2$ concentration with a short time response less than 3 s of steady-state current resulting from high conductivity and excellent synergetic electrocatalyst acting of the Cu$_2$O@MnO$_2$ composite materials.

Fig. 6. (A) Amperometric response of the modified electrode towards H$_2$O$_2$ addition from 0.5 to 20,000 μM in 0.05 M PBS pH 7.2. (B) A calibration curve between the response current of the Cu$_2$O@MnO$_2$/GCE and H$_2$O$_2$ concentration (n = 3).

The developed sensor provided a wide linear range for the H$_2$O$_2$ oxidation reaction from 0.5 μM to 20 mM with a good sensitivity of 256.33 μA mM^{-1} cm^{-2}. The limit of detection (LOD) was calculated to be 63 nM (S/N = 3) which suggested that the synthesized Cu$_2$O@MnO$_2$ composite materials greatly enhanced the performance of the sensor for quantitative H$_2$O$_2$ analysis.

3.5 Repeatability, Reproducibility Stability, and Selectivity Studies

In order to study the repeatability, the Cu$_2$O@MnO$_2$/GCE sensor was examined by calculation of relative standard deviation (%RSD) from ten obtained amperometric current response values of the same modified electrode to 5 mM H$_2$O$_2$ measurements. Also, the reproducibility was examined. Ten independent modified electrodes were operated and its %RSD was calculated via the same procedure. This method demonstrated excellent repeatability and good reproducibility of 1.25 and 3.55 %RSD, respectively, which were comparable to previous reports [38]. Under the same conditions, the Cu$_2$O@MnO$_2$/GCE was also tested to investigate its stability, the data is presented in the supplemental files (Table S1 and Figure S1). The results demonstrated that the sensor preserved 85 % of its initial current response over 100 usage times. The interference effect of the proposed method was also studied by an amperometric technique which presented good selectivity without interference from normal electroactive species such as ascorbic acid, ethanol, glucose, sucrose and uric acid as shown in supplementary (Figure S2). These investigations pointed out the novel robust and efficient platform of Cu$_2$O@MnO$_2$ for H$_2$O$_2$ sensing applications. Additionally, this method was comparable to the earlier literature as shown in Table 1. Finally, this sensor has been successfully applied to detect H$_2$O$_2$ in various samples, data presented in Table 2. This method showed potential usage as a H$_2$O$_2$ sensor as it showed a % recovery of 100 ± 3.64 %.

Table 2. The test of Cu$_2$O@MnO$_2$/GCE for H$_2$O$_2$ measurement in various samples.

Sample	H$_2$O$_2$ detected/μM	H$_2$O$_2$ added/μM	Increased H$_2$O$_2$/μM	% Recovery
Wound care solution 1	26.50	250	251.64	100.66
Wound care solution 2	38.40	250	253.17	101.27
Mouthwash 1	ND	250	249.20	99.68
Mouthwash 2	26.89	250	252.94	101.18
Hair dye 1	50.45	250	259.10	103.64
Hair dye 2	36.50	250	245.33	98.13

ND = Not detectable.

Full Paper

4 Conclusions

In this research, a novel, efficient, enzyme-free hydrogen peroxide sensor utilizing a modified $Cu_2O@MnO_2$ composite material was fabricated. The developed H_2O_2 sensor exhibited a wide linear range from 0.5 μM to 20 mM with a low detection limit of 63 nM (S/N=3) and good sensitivity of 256.33 $\mu A\,mM^{-1}\,cm^{-2}$. The $Cu_2O@MnO_2/$ GCE sensor showed excellent electrochemical and satisfactory kinetic performances. Also, it presented high stability, repeatability, and reproducibility. The results suggested that the simple, successful synthesis of $Cu_2O@MnO_2$ as a new platform was useful for construction of H_2O_2 sensor. This proposed method is considered for application in the development of enzyme-free H_2O_2 sensors and enzyme-based biosensors as well.

References

[1] a) R. Zhang, W. Chen, *Biosens. Bioelectron.* **2017**, *89*, 249–268; b) J. Chen, Y. Gao, Q. Ma, X. Hu, Y. Xu, X. Lu, *Sens. Actuators B* **2018**, *268*, 270–277; c) M. Roushani, B. Z. Dizajdizi, *Catal. Commun.* **2015**, *69*, 133–137.
[2] a) Y. Li, Y. Zhang, Y. Zhong, S. Li, *Appl. Surf. Sci.* **2015**, *347*, 428–434; b) S. Mutyala, J. Mathiyarasu, *Mater. Sci. Eng. C* **2016**, *69*, 398–406; c) S. Kiani Shahvandi, H. Ahmar, S. J. Tabatabaei Rezaei, *Surf. Interfaces* **2018**, *12*, 71–77.
[3] R. Pourfaraj, S. Y. Kazemi, S. J. Fatemi, P. Biparva, *J. Photochem. Photobiol. A* **2018**, *364*, 534–541.
[4] P. Gimeno, C. Bousquet, N. Lassu, A.-F. Maggio, C. Civade, C. Brenier, L. Lempereur, *J. Pharm. Biomed. Anal.* **2015**, *107*, 386–393.
[5] X. Zhang, X. Bi, W. Di, W. Qin, *Sens. Actuators B* **2016**, *231*, 714–722.
[6] B. Li, J.-B. Chen, Y. Xiong, X. Yang, C. Zhao, J. Sun, *Sens. Actuators B* **2018**, *268*, 475–484.
[7] D. Navadeepthy, A. Rebekah, C. Viswanathan, N. Ponpandian, *Mater. Res. Bull.* **2017**, *95*, 1–8.
[8] E. C. Hurdis, H. Romeyn, *Anal. Chem.* **1954**, *26*, 320–325.
[9] a) S. Anjum, Z. Liu, W. Gao, W. Qi, M. R. H. S. Gilani, M. Ahmad, R. Aziz ur, G. Xu, *J. Electroanal. Chem.* **2015**, *750*, 74–78; b) C. Qi, J. Zheng, *J. Electroanal. Chem.* **2015**, *747*, 53–58.
[10] a) C. Chen, X. Hong, T. Xu, A. Chen, L. Lu, Y. Gao, *Synth. Met.* **2016**, *212*, 123–130; b) N. C. Sekar, L. Ge, S. A. Mousavi Shaegh, S. H. Ng, S. N. Tan, *Sens. Actuators B* **2015**, *210*, 336–342; c) A. Boujakhrout, P. Díez, A. Sánchez, P. Martínez-Ruíz, J. M. Pingarrón, R. Villalonga, *J. Colloid Interface Sci.* **2016**, *482*, 105–111.
[11] a) Q. Yan, Z. Wang, J. Zhang, H. Peng, X. Chen, H. Hou, C. Liu, *Electrochim. Acta* **2012**, *61*, 148–153; b) X. Qin, H. Wang, Z. Miao, J. Li, Q. Chen, *Talanta* **2015**, *139*, 56–61.
[12] S. Kogularasu, M. Govindasamy, S.-M. Chen, M. Akilarasan, V. Mani, *Sens. Actuators B* **2017**, *253*, 773–783.
[13] a) J. Zhou, M. Min, Y. Liu, J. Tang, W. Tang, *Sens. Actuators B* **2018**, *260*, 408–417; b) C. Zhang, R. Zhang, X. Gao, C. Cheng, L. Hou, X. Li, W. Chen, *ACS Omega* **2018**, *3*, 96–105; c) C. Zhang, L. Li, J. Ju, W. Chen, *Electrochim. Acta* **2016**, *210*, 181–189; d) J. Ju, W. Chen, *Anal. Chem.* **2015**, *87*, 1903–1910.
[14] a) M. Wang, X. Jiang, J. Liu, H. Guo, C. Liu, *Electrochim. Acta* **2015**, *182*, 613–620; b) M. Liu, S. He, W. Chen, *Nanoscale* **2014**, *6*, 11769–11776.
[15] Z. Yu, H. Li, X. Zhang, N. Liu, X. Zhang, *Talanta* **2015**, *144*, 1–5.
[16] C.-Y. Lin, C.-T. Chang, *Sens. Actuators B* **2015**, *220*, 695–704.
[17] Y. Yang, J. Zhao, L. Qin, Y. Yin, L. He, *Mater. Lett.* **2016**, *179*, 27–29.
[18] R. Chaisuksant, T. Chomsook, N. Manthong, K. Kalcher, *Procedia Chem.* **2016**, *20*, 81–84.
[19] G. R. K. Reddy, H. Hyder, P. S. Kumar, *Mater. Today* **2017**, *4*, 12457–12469.
[20] a) M. Asif, W. Haitao, D. Shuang, A. Aziz, G. Zhang, F. Xiao, H. Liu, *Sens. Actuators B* **2017**, *239*, 243–252; b) X. Wen, M. Long, A. Tang, *J. Electroanal. Chem.* **2017**, *785*, 33–39.
[21] a) M. Balık, V. Bulut, I. Y. Erdogan, *Int. J. Hydrogen Energy* **2018**; b) Y. Su, H. Guo, Z. Wang, Y. Long, W. Li, Y. Tu, *Sens. Actuators B* **2018**, *255*, 2510–2519.
[22] L. Wu, X. Zhang, M. Wang, L. He, Z. Zhang, *Meas. Control* **2018**, *128*, 189–196.
[23] W. Chen, F. Deng, M. Xu, J. Wang, Z. Wei, Y. Wang, *Sens. Actuators B* **2018**, *273*, 498–504.
[24] a) C. Cheng, C. Zhang, X. Gao, Z. Zhuang, C. Du, W. Chen, *Anal. Chem.* **2018**, *90*, 1983–1991; b) X. Gao, S. He, C. Zhang, C. Du, X. Chen, W. Xing, S. Chen, A. Clayborne, W. Chen, *Adv. Sci.* **2016**, *3*, 1600126–1600126; c) M. Liu, R. Liu, W. Chen, *Biosens. Bioelectron.* **2013**, *45*, 206–212.
[25] a) C. Yu, J. Cui, Y. Wang, H. Zheng, J. Zhang, X. Shu, J. Liu, Y. Zhang, Y. Wu, *Appl. Surf. Sci.* **2018**, *439*, 11–17; b) H. Yin, Z. Cui, L. Wang, Q. Nie, *Sens. Actuators B* **2016**, *222*, 1018–1023.
[26] a) Y. Shu, J. Xu, J. Chen, Q. Xu, X. Xiao, D. Jin, H. Pang, X. Hu, *Sens. Actuators B* **2017**, *252*, 72–78; b) S. He, B. Zhang, M. Liu, W. Chen, *RSC Adv.* **2014**, *4*, 49315–49323.
[27] L. Luo, F. Li, L. Zhu, Z. Zhang, Y. Ding, D. Deng, *Electrochim. Acta* **2012**, *77*, 179–183.
[28] C.-H. Chen, E. C. Njagi, S.-Y. Chen, D. T. Horvath, L. Xu, A. Morey, C. Mackin, R. Joesten, S. L. Suib, *Inorg. Chem.* **2015**, *54*, 10163–10171.
[29] a) S.-K. Li, X. Guo, Y. Wang, F.-Z. Huang, Y.-H. Shen, X.-M. Wang, A.-J. Xie, *Dalton Trans.* **2011**, *40*, 6745–6750; b) J. Liu, X. Ge, X. Ye, G. Wang, H. Zhang, H. Zhou, Y. Zhang, H. Zhao, *J. Mater. Chem. A* **2016**, *4*, 1970–1979; c) Z.-L. Wu, C.-K. Li, J.-G. Yu, X.-Q. Chen, *Sens. Actuators B* **2017**, *239*, 544–552; d) Y. Xu, D. Chen, X. Jiao, K. Xue, *J. Phys. Chem. C* **2007**, *111*, 16284–16289.
[30] a) B. Xu, M.-L. Ye, Y.-X. Yu, W.-D. Zhang, *Anal. Chim. Acta* **2010**, *674*, 20–26; b) Y. Han, J. Zheng, S. Dong, *Electrochim. Acta* **2013**, *90*, 35–43; c) H.-L. Xu, W.-D. Zhang, *Chin. Chem. Lett.* **2017**, *28*, 143–148.
[31] a) D. Li, L. Meng, S. Dang, D. Jiang, W. Shi, *J. Alloys Compd.* **2017**, *690*, 1–7; b) D. Li, L. Meng, P. Xiao, D. Jiang, S. Dang, M. Chen, *J. Electroanal. Chem.* **2017**, *791*, 23–28;

Full Paper

c) P. Yan, L. Zhong, X. Wen, A. Tang, *J. Electroanal. Chem.* **2018**, *827*, 1–9.

[32] J. G. Ayenimo, S. B. Adeloju, *Food Chem.* **2017**, *229*, 127–135.

[33] M. Sheng, Y. Gao, J. Sun, F. Gao, *Biosens. Bioelectron.* **2014**, *58*, 351–358.

[34] a) H. Çelik Kazıcı, A. Caglar, T. Aydogmus, N. Aktas, H. Kivrak, *J. Colloid Interface Sci.* **2018**, *530*, 353–360; b) C. Moonla, A. Preechaworapun, T. Tangkuaram, *Electroanalysis* **2017**, *29*, 2698–2707.

[35] A. Sharma, K. Rawat, H. B. Bohidar, P. R. Solanki, *Appl. Clay Sci.* **2017**, *146*, 297–305.

[36] a) A. Eftekhari, *Talanta* **2001**, *55*, 395–402; b) A. Liu, W. Dong, E. Liu, W. Tang, J. Zhu, J. Han, *Electrochim. Acta* **2010**, *55*, 1971–1977; c) Y. Li, J. Zhang, H. Zhu, F. Yang, X. Yang, *Electrochim. Acta* **2010**, *55*, 5123–5128.

[37] a) S.-Q. Liu, H.-X. Ju, *Anal. Biochem.* **2002**, *307*, 110–116; b) L.-G. Zamfir, L. Rotariu, V. E. Marinescu, X. T. Simelane, P. G. L. Baker, E. I. Iwuoha, C. Bala, *Sens. Actuators B* **2016**, *226*, 525–533; c) B.-H. Jeon, D.-H. Yang, C.-S. Lee, Y.-D. Kim, J. S. Shin, *Electrochim. Acta* **2018**.

[38] a) W. Hooch Antink, Y. Choi, K.-d. Seong, Y. Piao, *Sens. Actuators B* **2018**, *255*, 1995–2001; b) B. Amanulla, S. Palanisamy, S.-M. Chen, V. Velusamy, T.-W. Chiu, T.-W. Chen, S. K. Ramaraj, *J. Colloid Interface Sci.* **2017**, *487*, 370–377; c) H. Dai, D. Chen, P. Cao, Y. Li, N. Wang, S. Sun, T. Chen, H. Ma, M. Lin, *Sens. Actuators B* **2018**, *276*, 65–71.

[39] L. Li, Z. Du, S. Liu, Q. Hao, Y. Wang, Q. Li, T. Wang, *Talanta* **2010**, *82*, 1637–1641.

[40] A. Salimi, M. Mahdioun, A. Noorbakhsh, A. Abdolmaleki, R. Ghavami, *Electrochim. Acta* **2011**, *56*, 3387–3394.

[41] Y. Li, F. Huang, Z. Luo, B. Xu, X. Wang, F. Li, F. Wang, L. Huang, S. Li, Y. Li, *Electrochim. Acta* **2012**, *74*, 280–286.

[42] M. Roushani, E. Karami, A. Salimi, R. Sahraei, *Electrochim. Acta* **2013**, *113*, 134–140.

[43] P. Pang, Z. Yang, S. Xiao, J. Xie, Y. Zhang, Y. Gao, *J. Electroanal. Chem.* **2014**, *727*, 27–33.

[44] M. A. Karimi, F. Banifatemeh, A. Hatefi-Mehrjardi, H. Tavallali, Z. Eshaghia, G. Deilamy-Rad, *Mater. Res. Bull.* **2015**, *70*, 856–864.

[45] Y. Pan, Z. Hou, W. Yi, W. Zhu, F. Zeng, Y.-N. Liu, *Talanta* **2015**, *141*, 86–91.

[46] F. Mollarasouli, K. Asadpour-Zeynali, S. Campuzano, P. Yáñez-Sedeño, J. M. Pingarrón, *Electrochim. Acta* **2017**, *246*, 303–314.

[47] Y.-S. Wu, Z.-T. Liu, T.-P. Wang, S.-Y. Hsu, C.-L. Lee, *Ultrason. Sonochem.* **2018**, *42*, 659–664.

Full Paper

Enhancing a Novel Robust Multicomposite Materials Platform for Glucose Biosensors

Chochanon Moonla,[a] Chantarattana Nontapha,[b] Tik Ouiram,[a] Anchana Preechaworapun,[c] and Tanin Tangkuaram*[a]

Abstract: An effective, stable enzymatic glucose biosensor was fabricated on a glassy carbon electrode (GCE) surface using simple multicomposite materials (MCM): a solution of prepared poly(diallyldimethylammonium chloride)-capped gold nanoparticles-nickel ferrite particles-carbon nanotubes-chitosan (PDDA-AuNPs-NiFe$_2$O$_4$-CNTs-CHIT), electropolymerization of poly(*o*-phenylenediamine) (P*o*PD) and immobilization of glucose oxidase (GOx). Biocompatibility and synergy of the MCM enhanced the immobilization and the reaction of GOx and as well as the electron transfer from an oxidation reaction of hydrogen peroxide in the system. The NiFe$_2$O$_4$ was synthesized by co-precipitation and calcined at 700 °C. Characterization was carried out by field emission scanning electron microscopy (FE-SEM), energy-dispersive X-ray spectroscopy (EDX), Fourier transform infrared spectroscopy (FTIR) and X-ray diffraction (XRD) which presented both tetrahedral and octahedral metal stretching with a cubic NiFe$_2$O$_4$ crystal phase. The GOx/P*o*PD/MCM/GCE yielded a 0.77 s^{-1} charge transfer rate constant (K_s), a 2.28×10^{-6} cm^2 s^{-1} diffusion coefficient value (D), a 0.21 mm^2 electroactive surface area (A_e) and a 1.93×10^{-8} mol cm^{-2} surface concentration (γ) as determined by cyclic voltammetry. The modified electrode showed a durable operation time (n = 97, more than 50 % I), repeatability (%RSD = 0.38, n = 10), reproducibility (%RSD = 1.60, n = 10), high sensitivity (853.07 µA mM^{-1} cm^{-2}), selectivity without effects of electroactive species (aspirin, uric acid, caffeine, cholesterol, ascorbic acid and dopamine) and two linear ranges from 0.5 to 10 µM (R^2 = 0.998) and 10 to 15,000 µM (R^2 = 0.991) with a low detection limit (0.35 µM, S/N = 3). Its Michaelis-Menten constant (K_m) was calculated as 93.51 µM with 46.30 µA maximum current (I_{max}). This proposed simple method was successfully applied for glucose determination in human blood samples.

Keywords: Glucose biosensors · Multicomposite-materials · Nickel ferrite nanoparticles · Poly(*o*-phenylenediamine)

1 Introduction

Throughout recent decades, nanoscience and nanotechnology has been utilized in development of biosensors and related bioanalytical tools. Due to their desirable, unique properties, many dominant nanomaterials play important roles in applications as catalysts, optical or electroactive labels and immobilization platforms [1]. Carbon nanotubes (CNTs), originally described by Sumio Iijima in 1991, become an attractive choice for biosensor fabrication among a variety of nanomaterials resulting from its superior useful properties such as excellent chemical stability, good mechanical strength and electrical conductivity [2]. However, CNTs have a limited usage due to its low solubility in most solvents [3] though there are many strategies that attempt to solve this problem, for example, the use of surfactants [4] with sonication and polymer wrapping [5]. The use of chitosan (CHIT), a natural, biodegradable cationic polymer, as a scaffolding material has been widely used and reported in biosensing field since its matrix provides biocompatibility, effective adhesion and absorption onto electrode surfaces, high affinity in aqueous solutions and excellent nanomaterial incorporation [6]. Thus, dispersion of CNTs into a CHIT matrix can overcome these limitations and improves its mechanical and electrical properties as a functional polymer membrane. Nickel ferrite (NiFe$_2$O$_4$) is also one of the most important materials that can be used for biosensors applications due to its notable electrocatalytic property [7]. Conventional methods for NiFe$_2$O$_4$ preparation [8], such as mechanosynthesis [9], sol-gel processing [10], solvothermal processes [11], spray pyrolysis [12], hydrothermal processes [13] and microwave assisted combustion methods [14], are generally quite difficult to control its size and morphology [15]. Therefore co-precipitation is an appealing technique due to its advantages of homogeneity, small particle size, low temperature preparation and simple process [16]. According to earlier

[a] C. Moonla, T. Ouiram, T. Tangkuaram
Applied Chemistry Program, Faculty of Science, Maejo University, Chiang Mai 50290, Thailand
E-mail: tanin.tang@gmail.com
[b] C. Nontapha
Chemistry Program, Faculty of Science, Maejo University, Chiang Mai 50290, Thailand
[c] A. Preechaworapun
Chemistry Program, Faculty of Science and Technology, Pibulsongkram Rajabhat University, Phitsanulok 65000, Thailand

Full Paper

reports regarding promising materials for electrochemical detection, poly(diallydimethylammonium chloride)-capped gold nanoparticles (PDDA-AuNPs) have been extensively used for modification of electrode surfaces as various biosensors yielding excellent conductivity, high surface area and catalytic properties [17]. Besides nano-materials, poly(o-phenylenediamine) (PoPD) is an excellent permselective polymer film to H_2O_2 (the byproduct of oxidase-based biosensors) and an effective blocker of interference species [18]. It is challenging to combine all aforementioned materials in a novel platform with the appropriate ratio for efficiently cooperated-work in a synergetic way.

Diabetes mellitus has become one of the major global health concerns according to World Health Organization (WHO) that requires considerable attention. Millions of people worldwide suffer from diseases of abnormal blood glucose levels such as lower than normal blood glucose (hypoglycemia) or higher than normal glucose (hyper-glycemia) with the normal range defined as (4–7 mM) [19]. These conditions may lead to many life-threatening diabetic complications such as retina, circulatory, and kidney system disorders [20]. In order to reduce and prevent the negative effects, the diabetic patient must control their blood glucose level and maintain a daily monitor of blood glucose as well [21]. Additionally, an intimate blood glucose measurement is necessary for clinical diagnosis and treatment of diabetes mellitus [22] which makes glucose the most frequently tested, clinically-relevant analyte [23]. Thus, the continuous develop-ment of simple, accessible and effective devices to determine the glucose concentration for ordinary people is very important to contribute to fast preliminary self-diagnosis and early treatment.

Currently, the development of many different types of devices for clinical diagnosis has been reported. Since Clark and Lyons introduced the initial enzyme-based glucose sensor concept in 1962 [24], it has been a springboard for great potential and new research concepts in various fabrication and design fields of enzymatic sensors or biosensors [25]. In spite of significant efforts toward development of non-enzymatic sensors, enzyme-based biosensors are superior in selectivity and sensitivity [26]. Among the enzyme-based glucose biosensors, glu-cose oxidase (GOx), which catalyzes the glucose oxidation to gluconolactone and H_2O_2, is mainly used due to its simplicity, inexpensive cost and great pH withstanding [27]. Then, the generated byproduct, H_2O_2, is immediately reacted at the working electrode surface which provides the current response proportional to glucose concentra-tion in the system via electrochemical detection [28]. However, there are some challenging issues for GOx. Those issues include limitations regarding the operating conditions including temperature, humidity, short lifetime resulting from the denaturation of enzyme activity [29] and also electron transfer difficulty due to layer thickness between the active sites of GOx and the electrode [19]. This can lead to the ineffective performance of enzyme-based glucose biosensors. To overcome these obstacles, creative approaches have been applied to maintain and improve the biological activity of GOx [30]. One attrac-tive strategy is the use of nanomaterials, a conducting polymer and a polymer membrane which can efficiently enhance electron transfer and enzyme loading. In this research, we aim to prepare a unique platform of multi-composite materials (MCM), PDDA-AuNPs-NiFe$_2$O$_4$-CNTs-CHIT, for modification of a glassy carbon electrode and enhance the signal with the PoPD film as in Figure 1
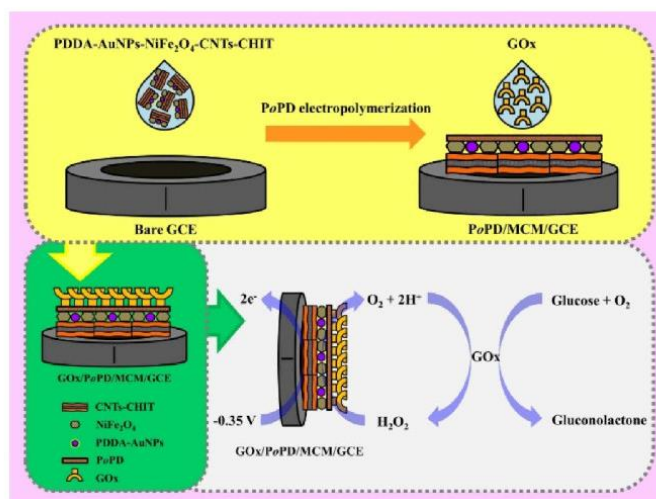

Fig. 1. Schematic illustration of the fabrication of glucose biosensors and its electrochemical reaction.

Full Paper

which provides for appropriate biocompatibility, long-term stability and high surface area for fabrication of a novel, robust, and effective glucose biosensors.

2 Experimental

2.1 Materials

Glucose oxidase (GOx) from *Aspergillus niger* (EC 1.1.3.4, 5.1 U mg^{-1}) was provided by Sigma-Aldrich Co. LLC (Mannheim, Germany). Aspirin, caffeine anhydrous, chitosan (CHIT), dopamine, gold (III) chloride trihydrate, carbon nanotube (multi-walled), poly(diallyldimethylammonium chloride) 35 wt. % solution and uric acid were purchased from Sigma-Aldrich Co. LLC (St. Louis, USA). Iron (II) sulfate heptahydrate, iron (III) nitrate nonahydrate, nickel (II) nitrate hexahydrate, and nitric acid were purchased from QRëc, New Zealand. Acetic acid, diethyl ether, and sodium hydroxide were provided by RCl Labscan (Bangkok, Thailand). Ethanol and hydrochloric acid were provided by Merck (Darmstadt, Germany). Glutaraldehyde (GA) solution (50.0 %) and *o*-phenylenediamine were obtained from Fluka (St. Louis, USA). Cholesterol was obtained from Carlo Erba (Milan, Italy). Dipotassium hydrogen orthophosphate was purchased from Fisher Scientific (New Hampshire, USA). Glucose was purchased from Ajax Finechem (New South Wales, Australia). Potassium dihydrogen orthophosphate was provided by Rankem (Haryana, India). Potassium chloride solution (3 M) was provided by Metrohm (Herisau, Switzerland).

All reagents and solvents used were analytical grades without further purification and ultra-high purity water (UHP) by Milli-Q Advantage A10 Water Purification System (France) was used for all experiments.

2.2 Synthesis of NiFe$_2$O$_4$ Particles

Nickel ferrite particles were synthesized by co-precipitation by methods adapted from earlier reports [31]. Briefly, nickel (II) nitrate hexahydrate, iron (II) sulfate heptahydrate and iron (III) nitrate nonahydrate (3:5:1 stoichiometric ratio) were dissolved in N$_2$-saturated UHP water. The pH of the solution was adjusted to 12 by a 1.5 M sodium hydroxide solution which resulted in a dark green suspension. It was heated and continuously stirred at 100 degrees Celsius for half an hour under the N$_2$-saturated atmosphere. The obtained solid was filtered and washed with N$_2$-saturated UHP water followed by an ethanol rinse. The product was dried at room temperature and calcined at 700 degrees Celsius for 2 hours. The synthesized NiFe$_2$O$_4$ powder was stored at room temperature and used for further work.

2.3 Preparation of the PDDA-AuNPs Solution

According to previously reported literature, a solution of 35 wt. % PDDA (60 μL), 0.50 M NaOH (50 μL), 1 %

HAuCl$_4$ solution (75 μL) and 10 mL UHP water were mixed and heated at 90 degrees Celsius for half an hour and resulted in the watermelon red PDDA-AuNPs solution [32].

2.4 Preparation of the MCM Solution

The MCM solution can be prepared through only a few steps. In order to create a carboxyl group of the CNT surface, the CNTs were pretreated by soaking in a mix of nitric and sulfuric acids. Then, 3 mg of CNTs-COOH, 2 mg of NiFe$_2$O$_4$ and 500 μL of the PDDA-AuNPs solution were mixed in 1 mL of 0.5 % CHIT crosslinked 0.5 % glutaraldehyde (stoichiometric ratio of CHIT:GA as 1:200). Finally, the solution was sonicated at room temperature for half an hour. It was stored at room temperature for further work.

2.5 Fabrication of the Glucose Biosensor

Firstly, 20 μL of the MCM solution was added dropwise onto a clean glassy carbon electrode surface and dried at room temperature. Then, a 1 M *o*-phenylenediamine solution was electropolymerized as a thin, light yellow film onto the modified electrode surface via cyclic voltammetry (−0.2 to 1.0 V, 15 cycles, 25 mV s^{-1}) [33]. Once dry, 20 μL of a 3 mg mL^{-1} GOx solution was immobilized and dried at room temperature. Then, the electrode surface was washed with UHP water to remove excess enzyme. Finally, the GOx/*P*oPD/MCM/GCE biosensor was kept in the refrigerator at 3–4 °C to preserve its function and lifetime.

2.6 Instrumentation

The Fourier Transform Infrared Spectrometer (FTIR) (PerkinElmer model Spectrum RX I, PerkinElmer, England) and X-ray Diffractometer (XRD) (Rigaku MiniFlex II, Japan) were used for characterization of the synthesized NiFe$_2$O$_4$ particles. Field Emission Scanning Electron Microscope (FE-SEM) (JEOL JSM-6335F, USA) was used for characterization of the synthesized NiFe$_2$O$_4$ particles, the *P*oPD film, and the modified electrode surface. The ultraviolet-visible spectrophotometer (Hitachi model U-2001, Hitachi, Japan) was used for the study of the prepared PDDA-AuNPs solution.

2.7 Electrochemical Measurements

All electrochemical measurements were performed using CH instruments (CH 1230, USA) with a three-electrode system composed of a Glassy Carbon Electrode (GCE) (3 mm diameter) as the working electrode, a Pt wire electrode (2 mm diameter) as the counter electrode and a Ag/AgCl electrode (3 M KCl) as the reference electrode. The electrochemical performance of glucose detection was assessed by cyclic voltammetric (CV) and ampero-

Full Paper

metric techniques in 5 mL of 0.05 M phosphate buffer solution (PBS, pH 7.0) at room temperature.

3 Results and Discussion

3.1 Characterization of Prepared Materials

During development of the biosensor, all materials on the modified glassy carbon electrode surface were characterized using various techniques. Nickel ferrite ($NiFe_2O_4$) particles were studied by FE-SEM, energy-dispersive x-ray spectroscopy (EDX), XRD and FTIR. The results showed that the synthesized particles were different in shape as shown in the SEM image in Figure 2A. The qualitative composition of the particles was confirmed showing the presence of iron, nickel, and oxygen from the EDX pattern (Figure 2B). Additionally, the XRD pattern presented its structural and morphological features as the crystalline nature and cubic-phase of $NiFe_2O_4$ (JCPDS no. 00-023-1119) corresponding to the planes (220), (311), (222), (400), (331), (422), (511), (440), (620), (533), (622) and (444) as seen in Figure 2C. The FTIR investigation in the wavenumber range of 400 to 1000 cm^{-1} yielded the spectrum which exhibited strong absorption peaks at 884, 836, 670 and 410 cm^{-1} as shown in Figure 2D. The higher frequency bands are related to intrinsic tetrahedral-metal stretching vibrations, while the peak at the position of 410 cm^{-1} is attributed to the Fe-O bond of octahedral-metal stretching vibrations [34]. The band around 700–900 cm^{-1} was assigned the Ni–O vibrations [35].

In addition to the $NiFe_2O_4$ particles, the PoPD film that was electro-polymerized onto the GCE surface was studied for its surface features by scanning electron microscope. In Figure 2E, the SEM images confirmed the existence of the deposited film onto the electrode surface with approximately 34-micron thickness, this higher thickness comes from PoPD (Figure 2F) for 10-micron. Moreover, the PDDA-AuNPs solution was examined by the UV-Visible spectrometer. As shown in Figure 2G, the result with the characteristic peak absorbance of gold nanoparticles at 525 nm which corresponding to the earlier reports [36] suggested that PDDA-AuNPs were successfully prepared.

3.2 Electrochemical Performance of the Modified Electrodes

In order to study of the electrochemical performance, each modified electrode compared to the bare GCE was investigated in a) N_2-saturated 0.05 M PBS pH 7.0, b) 5 mM and c) 10 mM glucose solutions using cyclic voltammetry ($E_{applied}$ of −1.0 to 1.0 V, 50 mV s^{-1}). As in Figure 3A, the cyclic voltammogram of the bare GCE was obviously indifferent due to the absence of H_2O_2 in the system. All voltammograms showed the curve at −0.80 V resulting from the O_2 reduction. In contrast to Figure 3B, the background current of each cyclic voltammogram of the GOx/GCE changed slightly, resulting from the

oxidation reaction of the presence of H_2O_2 from increasing glucose concentration, clearly in the potential range of 0.6 to 1.0 V. By comparing Figure 3C, 3D, 3E and 3F, it was evident that the more materials applied, yielded the higher background current and redox curve of the redox reaction of H_2O_2. It was observed that the GOx/PoPD/MCM/GCE (Figure 3F) showed both reduction and oxidation peak current increases in O_2 saturated PBS with increasing concentrations of glucose (0, 5, and 10 mM) and it was similar to previous reports [37]. The increase in both reduction and oxidation peaks due to the PoPD/MCM on the modified GOx/PoPD/MCM/GCE electrode was extremely redox mediated for the transformation of glucose to gluconolactone for the anodic side, while for the cathodic side may catalyze the generated H_2O_2 reduction. Compared to the GOx/MCM/GCE (Figure 3E), the MCM showed a direct electron transfer (DET) phenomenon of the GOx. These suggested that the modified MCM as a novel platform in this work can effectively enhance the current response of H_2O_2 oxidation reaction with respect to glucose concentration. The most evidence for this claim is shown in Figure 3F owing to the PoPD synergetic operation to improve electrical properties and electron transfer on both flexible rough and high surface area. Thus, the GOx/PoPD/MCM/GCE was determined suitable for application in glucose biosensors.

In order to investigate the kinetics of the GOx/PoPD/MCM/GCE, it was operated in 10 mM $K_3Fe(CN)_6$ containing 0.1 M KCl at various scan rates from 10 to 200 mV s^{-1} by cyclic voltammetry (data available in supplementary S1). The results revealed that this method was the quasi-reversible process and diffusion-controlled process in which both anodic (I_{pa}) and cathodic (I_{pc}) current responses proportionally increased with the square root of scan rate. From this study, the kinetic parameters, including charge transfer rate constant (K_s), diffusion coefficient value (D), electroactive surface area (A_e) and surface concentration (γ) can be calculated as previously reported [38] as 0.77 s^{-1}, 2.28×10^{-6} cm^2 s^{-1}, 0.21 mm^2 and 1.93×10^{-8} mol cm^{-2}, respectively. Calculations were carried out using the following equations:

$$K_s = mnFv/RT$$

$$I_p = (2.69 \times 10^5)n^{3/2}AD^{1/2}Cv^{1/2}$$

$$A_e = S/(2.99 \times 10^5)n^{3/2}CD^{1/2}$$

$$I_p = n^2F^2\gamma Av/4RT$$

where m is the peak-to-peak separation (V), F is the Faraday constant (96,485 C mol^{-1}), v is the scan rate (mV s^{-1}), n is the number of transferred electrons (1), R is the gas constant (8.314 J mol^{-1} K^{-1}), T is the room temperature (298.15 K), I_p is the peak current response of the electrode, A is the surface area of the electrode (cm^{-2}), D is the diffusion coefficient, C is the bulk concentration

Full Paper
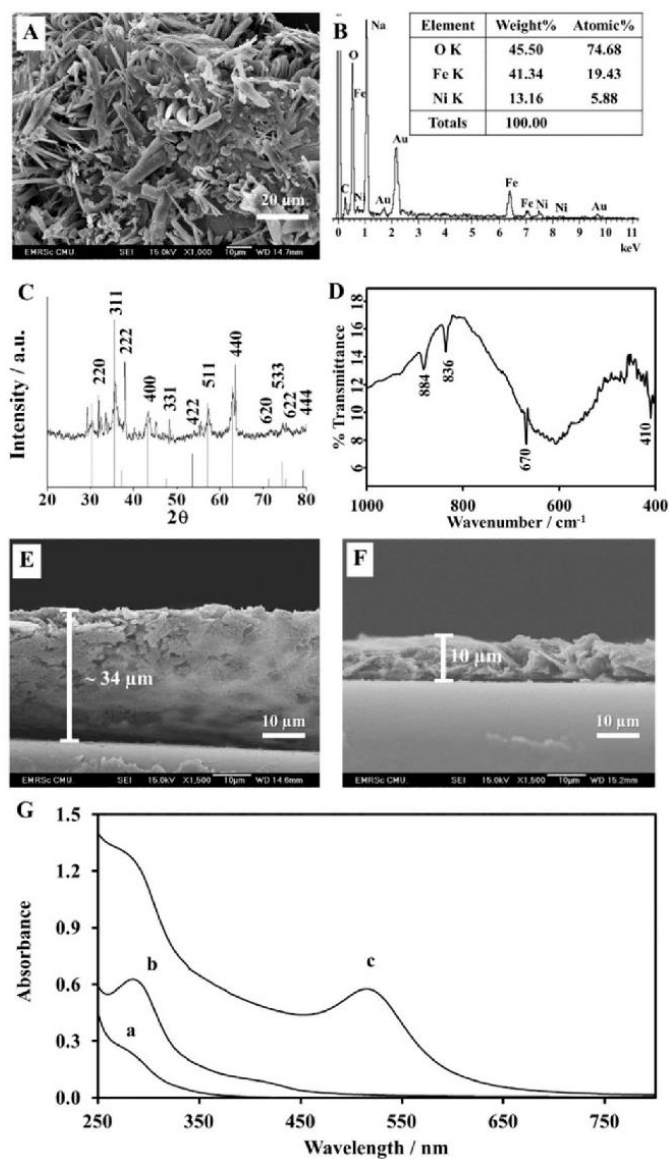
Fig. 2. SEM image (A) EDX spectrum (B) XRD pattern (C) and FT-IR spectrum (D) of NiFe$_2$O$_4$ particles. SEM images of cross section of the GOx/PoPD/MCM/GCE surface (E) and P*o*PD (F) film. UV-Vis spectra (G) of AuCl$_4^-$ (a) PDDA (b) and PDDA-AuNPs (c).

(10 mM), S is the slope of the straight line, and γ is the surface concentration (mol cm^{-2}). The related figure is presented in supplementary S1.

3.3 Optimization of Experimental Parameters

In order to obtain the maximum efficiency of fabricated glucose biosensors, it is necessary to consider the optimal condition. Thus, applied potential, pH loading, P*o*PD film cycle, and enzyme volume were studied and the qualita-

Full Paper

Fig. 3. Cyclic voltammograms of the bare GCE (A) GOx/GCE (B) GOx/CNTs-CHIT/GCE (C) GOx/NiFe$_2$O$_4$-CNTs-CHIT/GCE (D) GOx/MCM/GCE (E) and GOx/PoPD/MCM/GCE (F) in 0.05 M PBS pH 7.0 (a) containing 5 mM (b) and 10 mM (c) glucose at a scan rate of 50 mV s^{-1}.

tive effect of each material in the prepared solution including of CNTs, NiFe$_2$O$_4$ and PDDA-AuNPs were also

Fig. 4. The influence of applied potential (A) pH loading (B) PoPD film (C) and enzyme loading (D) on GCE in 0.05 M PBS containing 2 mM glucose by amperometry.
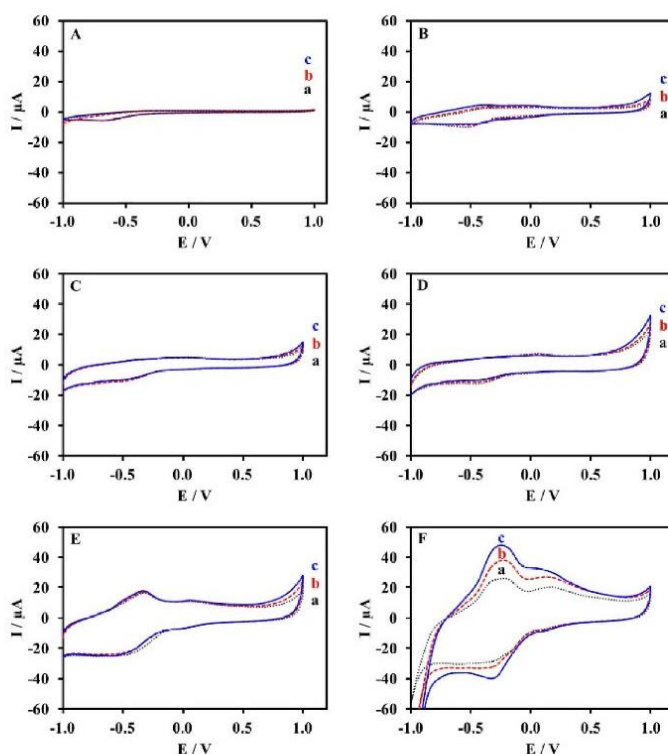
examined to gain its proper ratio in this work by amperometric technique. According to aforementioned CV study of GOx/PoPD/MCM/GCE, it was found that the oxidation reaction of H$_2$O$_2$ was in a potential range from −0.45 to −0.2 V. Therefore, this potential range was operated to gain the optimal applied potential of the system.

The results in Figure 4A showed that the current response of the H$_2$O$_2$ oxidation reaction was dominantly higher than the others at −0.35 V which was then selected for the further work. The pH of the electrolyte solution, phosphate buffer, was studied as well. This parameter is important to be considered because it affects the catalytic reaction of the enzyme and H$_2$O$_2$ reaction. In Figure 4B, the current response increased at a pH of 6.6 to 7.0. This can be explained due to the chitosan flexibility and H$_2$O$_2$ stability which are excellent at pH > 6.3 [39]. However, the current response linearly decreased at higher pH values. So, an electrolyte solution at a pH of 7.0 was determined suitable for the application. In Figure 4C, the deposition of PoPD film by electro-polymerization was
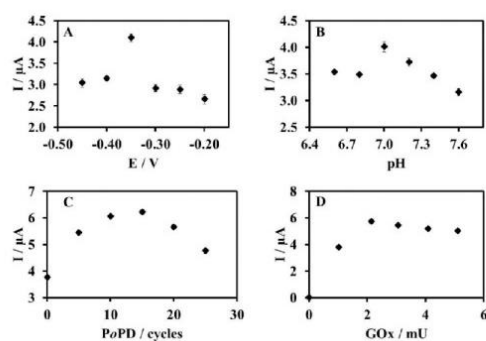
Full Paper

operated at various conditions from 0 to 25 cycles. It is evident that the current response was higher from 0 to 15 cycles and then clearly decreased due to the effect of film thickness. Therefore, 15 cycles of PoPD film deposition was selected for further study. The effect of GOx immobilization onto the electrode surface was determined in the volume range of 0 to 5 milliunits (mU) as shown in Figure 4D. The current response increased from 0 to 5 mU GOx, then moderately decreased at higher units of GOx due to reaching saturation. So, 2 mU GOx was selected for use in the glucose biosensor.

In Figure 5, the CNTs content (Figure 5A), the amount of NiFe$_2$O$_4$ (Figure 5B) and PDDA-AuNPs (Fig-
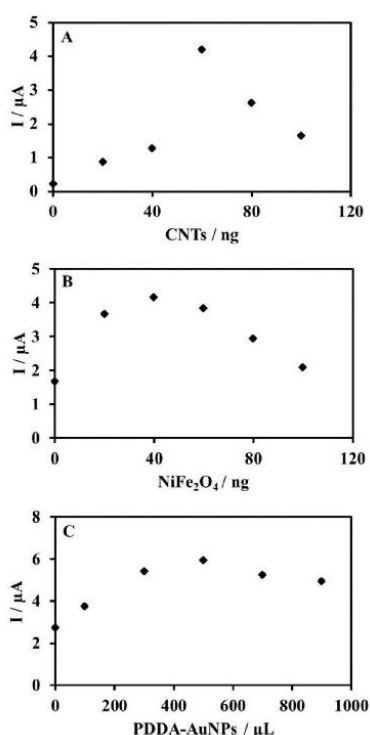

Fig. 5. The quantitative effect of MCM; CNTs (A) NiFe$_2$O$_4$ (B) and PDDA-AuNPs (C) on GCE in 0.05 M PBS pH 7.0 containing 2 mM glucose using amperometric technique.

ure 5C) volume mixed as solution were quantitatively examined to gain its suitable ratio for modification of the GCE surface. The results suggested that the MCM with 60 ng of CNTs, 40 ng of NiFe$_2$O$_4$ and 500 µL of PDDA-AuNPs provided the highest current response and were proper for further application.

3.4 Effect of Interferences

The selectivity of developed biosensors to the analyte is an important property and must be considered. Commonly, the electroactive species found in human blood samples which can affect glucose detection are aspirin, uric acid, caffeine, dopamine, cholesterol, and ascorbic acid. To determine the effect of these, the modified electrode was studied using amperometric technique at optimal condition. The presence of 2 mM glucose was compared to each interference addition in 0.05 M PBS pH 7.0, data showed in supplementary S2. The result suggested that all interferences failed to affect the obtained current response from glucose (S/N = 3) this is due to the enzyme specificity. The strong immobilization and effective catalytic reaction on the electrode surface with the enzyme are, in part, a result of the modified biocompatible composite materials as well. This indicated that the GOx/PoPD/MCM/GCE was very selective to glucose.

3.5 Linearity

The developed GOx/PoPD/MCM/GCE can be used to detect glucose using amperometric technique. Linearity of this biosensor was operated by the successive addition method under the optimal condition (E$_{applied}$ = −0.35 V, 0.05 M PBS pH 7.0, 60 ng CNT, 40 ng NiFe$_2$O$_4$, 500 µL PDDA-AuNPs, 15 cycles PoPD, 2 mU GOx). As Figure 6A, the amperometric current response of the modified electrode increased with respect to glucose concentration in two linear ranges of 0.5 to 10 µM (R^2 = 0.998) and 10 to 15,000 µM (R^2 = 0.991). At the low concentration linear range, a low detection limit (LOD = 0.35 µM, S/N = 3) and high sensitivity (853.07 µA mM^{-1} cm^{-2}) were determined by statistical calculations shown in Figure 6B (small box in the bottom, right-hand corner).

Also, information of the linearity was applied for calculation of the enzyme-substrate kinetic parameter as measured by the Michaelis-Menten constant (K_m) [40]. In this work, the Lineweaver-Burk equation [41] was used to calculate this parameter using the following equation:

$$\frac{1}{I_{SS}} = \frac{1}{I_{max}} + \frac{K_m}{I_{max}C}$$

where I_{ss} is the current at steady-state, I_{max} is the maximum current at saturated substrate and C is a certain concentration of the substrate (glucose, in this case). The resulting K_m value was found to be 93.51 µM (I_{max} = 46.30 µA) which was lower than earlier reported values [42]. Typically, it is desirable to obtain low K_m values because it accounts for good affinity of the modification layer of PoPD/MCM platform to the substrate and favorable conformation and effective loading of GOx onto GCE surface as well. These excellent calculated analytical parameters (LOD, sensitivity, K_m), presented
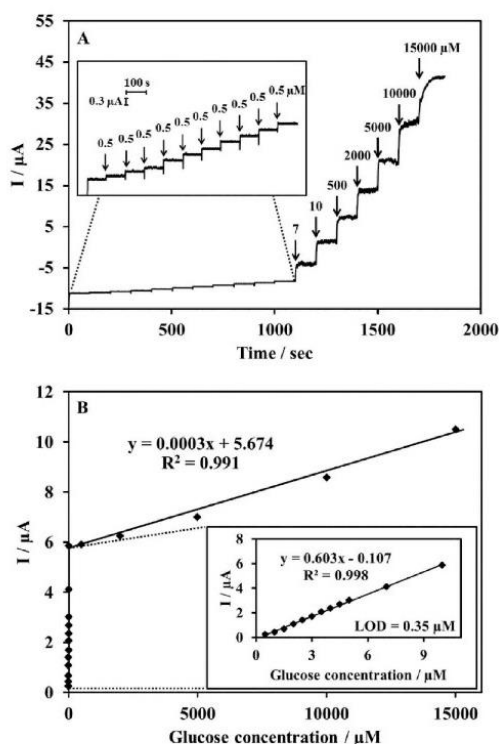
Full Paper

Fig. 6. (A) Amperometric response of the modified electrode towards glucose successive addition in 0.05 M PBS pH 7.0. Inset of A: amperogram of spiked glucose concentration range from 0.5 to 10 μM. (B) Calibration curve between the response current of the modified electrode and glucose concentration (0.5 to 15,000 μM). Inset of B: plot of the current versus low glucose concentration.

the obvious ability of this modified electrode to serve as a glucose biosensor when compared to other glucose biosensors [43]. These were attributed to more binding of the GOx (isoelectric point 4.2 [44]) due to the high isoelectric points of metal oxides (Ni, Cu, Fe phase varying from 6.6–9.5) [45]. Moreover, the biocompatibility and synergy of each material in the PoPD/MCM platform is suitable for GOx to provide highly effective electron communication between its active site and GCE surface.

3.6 Repeatability, Reproducibility and Stability Studies

Robustness of the developed method was studied regarding repeatability, reproducibility, and stability by amperometric technique. The GOx/PoPD/MCM/GCE was operated by spiking 2 mM glucose in 0.05 M PBS pH 7.0 under continuous stirring. The results exhibited acceptable repeatability and reproducibility to determine glucose calculated as 0.38 %RSD (n = 10) and 1.60 %RSD (n =

10), respectively. Additionally, the stable performance was operated by each spiking of 2 mM glucose in 0.05 M PBS pH 7.0 under continuous stirring by an intraday operation. It was an outstanding quantity count for the operation time up to 97 times that the percent current response was more than half the first operation (%I more than 50 %). These were due to biocompatibility and high flexible surface area of the PoPD/MCM platform resulting from the strong immobilization and effective catalytic reaction of GOx on the electrode surface.

3.7 Sample Analysis

To evaluate the performance of the GOx/PoPD/MCM/GCE as a glucose biosensor, it was applied to monitor glucose level in 5 human blood samples from Sansai Hospital, Chiang Mai, Thailand by standard addition method. The obtained results were compared to the results from commercial glucose biosensors (Blood glucose monitoring system, Easy G Optima, Pharmahof Co., Ltd., Thailand) as shown in Table 1. This indicated that

Table 1. Glucose detection in whole human blood samples.

Sample	Glucose biosensors[a] (mM)	Commercial glucose biosensors[a] (mM)	T-test (95 % CL)[b] Crit	Cal	F-test (95 % CL)[b] Crit	Cal
1	3.14 ± 0.10	3.07 ± 0.06	2.78	0.25	6.39	0.99
2	6.95 ± 0.17	6.87 ± 0.15				
3	3.29 ± 0.03	3.27 ± 0.12				
4	10.82 ± 0.11	10.90 ± 0.26				
5	1.51 ± 0.05	1.53 ± 0.06				

[a]n = 3 [b]Crit = critical value, Cal = calculation value, CL = confidence limit.

both were significantly indistinguishable at a confidence level of 95 % according to statistical F-test and T-test values.

Also, the developed method has high potential to determine the glucose level in whole real blood samples and was comparable to earlier reports in Table 2. Besides simplicity and quick fabrication, this modified electrode provided excellent stability and robustness due to the novel PoPD/MCM platform.

4 Conclusions

In summary, the novel and robust multicomposite materials solution, PDDA-AuNPs-NiFe$_2$O$_4$-CNTs-CHIT, was successfully prepared and efficiently used with a PoPD film and GOx for the surface modification of a glassy carbon electrode for use as a glucose biosensor. The sensor, developed with a low cost and high-throughput method, exhibited outstanding stability of up to 97 % of current response greater than 50 % compared to the initial current response. The GOx/PoPD/MCM/GCE exhibited

Full Paper

ELECTROANALYSIS

Table 2. Comparison of glucose biosensors.

Biosensors	Detection techniques	Voltage (V)	LOD (µM)	Linearity (mM)	K_m (mM)	Sensitivity (µA mM^{-1} cm^{-2})	Ref.
GOx/cage-like PbS/Nafion/GCE	BA	−0.45	10	0.05–1.45	0.49	11.02	[46]
PUCNT/GOD/GCE	DPV	−0.3 to −0.6	–	0–17	5.09	19.50	[47]
Glu-GOx/GNS-PEI-AuNPs/AuE	FIA-BA	−0.35	0.32	0.001–0.1	–	93	[48]
GOx/Ag@MWCNT-IL-Fe$_3$O$_4$/MGCE	BA	−0.51	3.8	0.01–1	0.49	–	[49]
GOx/p-NiO/n-Bi$_4$Ti$_3$O$_{12}$/Ti foil electrode	BA	−0.442	1.26	0.02–3.55	0.22	215	[50]
GOx/SiO$_2$(LuPc$_2$)-PANI(PVIA)-CNB/SPCE	BA	0.2	100	1–16	10.36	38.53	[51]
PCS/HB/GOD/CPE	CV	−0.3 to 0.8	32	0.1–5	–	76.43	[52]
GOx/PoPD/MCM/GCE	BA	−0.35	0.35	0.01–15	0.09	853.07	TW

AuE = Gold electrode, AuNPs = Gold nanoparticles, BA = Batch amperometry, CNB = Conducting nanobeads, CPE = Carbon paste electrode, CV = Cyclic voltammetry, DPV = Differential pulse amperometry, FIA = Flow injection analysis, GCE = Glassy carbon electrode, Glu = Glutaraldehyde, GNS = Graphene, GOD = Glucose oxidase, GOx = Glucose oxidase, HB = Hemoglobin, IL = Ionic liquid, MGCE = Magnetic glassy carbon electrode, MWCNT = Multi-walled carbon nanotubes, PANI(PVIA) = Poly(vinyl alcohol-vinyl acetate) itaconic acid, PCS = Polyaniline/multiwall carbon nanotubes/starch, PEI = Polyethyleneimine, PoPD/MCM = Poly(o-phenylenediamine)/multicomposite materials, PUCNT = Partially unzipped carbon nanotubes, LuPc$_2$ = Lutetium phthalocyanine, SPCE = Screen printed carbon electrode, TW = This work.

high sensitivity (853.07 µA mM^{-1} cm^{-2}), low detection limit (0.35 µM), repeatability (%RSD = 0.38, n = 10), reproducibility (%RSD = 1.60, n = 10) and good selectivity without exhibiting interference from electroactive species such as aspirin, uric acid, caffeine, dopamine, cholesterol and ascorbic acid. Moreover, the results suggested that the MCM covered by PoPD film in GOx/PoPD/MCM/GCE was suited for glucose detection in whole human blood samples and is possible to be used as a robust platform for fabrication of other biosensors.

References

[1] C. Jiang, L. Lan, Y. Yao, F. Zhao, J. Ping, *TrAC Trends Anal. Chem.* **2018**, *102*, 236–249.

[2] S. Gupta, C. N. Murthy, C. R. Prabha, *Int. J. Biol. Macromol.* **2018**, *108*, 687–703.

[3] M. E. Ghica, R. Pauliukaite, O. Fatibello-Filho, C. M. A. Brett, *Sens. Actuators B* **2009**, *142*, 308–315.

[4] M. F. Islam, E. Rojas, D. M. Bergey, A. T. Johnson, A. G. Yodh, *Nano Lett.* **2003**, *3*, 269–273.

[5] A. Star, J. F. Stoddart, D. Steuerman, M. Diehl, A. Boukai, E. W. Wong, X. Yang, S.-W. Chung, H. Choi, J. R. Heath, *Angew. Chem. Int. Ed.* **2001**, *40*, 1721–1725; *Angew. Chem.* **2001**, *113*, 1771–1775.

[6] a) S. Bibi, A. Jamil, T. Yasin, M. A. Rafiq, M. Nawaz, G. J. Price, *Eur. Polym. J.* **2018**, *105*, 297–303; b) M. J. Pannell,

E. E. Doll, N. Labban, M. B. Wayu, J. A. Pollock, M. C. Leopold, *J. Electroanal. Chem.* **2018**, *814*, 20–30.

[7] Y. Li, M. Zhao, J. Chen, S. Fan, J. Liang, L. Ding, S. Chen, *Appl. Surf. Sci.* **2016**, *362*, 115–120.

[8] R. Galindo, E. Mazario, S. Gutiérrez, M. P. Morales, P. Herrasti, *J. Alloys Compd.* **2012**, *536*, S241–S244.

[9] H. Salazar-Tamayo, M. A. Márquez, C. A. Barrero, *Powder Technol.* **2016**, *289*, 126–134.

[10] R. Sen, J. Pain, R. Patidar, S. Srivastava, R. S. Rana, N. Gupta, *Mater. Today* **2015**, *2*, 3750–3757.

[11] J. Wang, F. Ren, R. Yi, A. Yan, G. Qiu, X. Liu, *J. Alloys Compd.* **2009**, *479*, 791–796.

[12] D. S. Jung, Y. C. Kang, *J. Magn. Magn. Mater.* **2009**, *321*, 619–623.

[13] J. Huo, M. Wei, *Mater. Lett.* **2009**, *63*, 1183–1184.

[14] M. Venkatesh, G. S. Kumar, S. Viji, S. Karthi, E. K. Girija, *Mod. Electron. Mater.* **2016**, *2*, 74–78.

[15] K. Maaz, S. Karim, A. Mumtaz, S. K. Hasanain, J. Liu, J. L. Duan, *J. Magn. Magn. Mater.* **2009**, *321*, 1838–1842.

[16] V. S. Kiran, S. Sumathi, *J. Magn. Magn. Mater.* **2017**, *421*, 113–119.

[17] M. Amatatongchai, W. Sroysee, S. Chairam, D. Nacapricha, *Talanta* **2015**, *133*, 134–141.

[18] S. A. Rothwell, S. J. Killoran, E. M. Neville, A. M. Crotty, R. D. O'Neill, *Electrochem. Commun.* **2008**, *10*, 1078–1081.

[19] A. Y. Khan, S. B. Noronha, R. Bandyopadhyaya, *Adv. Powder Technol.* **2016**, *27*, 85–92.

[20] R. Khan, R. Ahmad, P. Rai, L.-W. Jang, J.-H. Yun, Y.-T. Yu, Y.-B. Hahn, I.-H. Lee, *Sens. Actuators B* **2014**, *203*, 471–476.

[21] A. V. Fonin, O. I. Povarova, M. Staiano, S. D'Auria, K. K. Turoverov, I. M. Kuznetsova, *Opt. Mater.* **2014**, *36*, 1676–1679.

[22] X. Zhang, L. Shen, M. Wang, G. Siqin, Z. Tong, R. Xu, D. Zhang, J. Ma, L. Liu, *Mater. Lett.* **2014**, *135*, 39–42.

[23] S. Das, M. Saha, *J. Pharma. Anal.* **2014**, *4*, 351–359.

[24] T. Bobrowski, W. Schuhmann, *Curr. Opin. Electrochem.* **2018**, *10*, 112–119.

[25] C. Hou, D. Zhao, Y. Wang, S. Zhang, S. Li, *J. Electroanal. Chem.* **2018**, *822*, 50–56.

[26] V. Vukojević, S. Djurdjić, M. Ognjanović, M. Fabián, A. Samphao, K. Kalcher, D. M. Stanković, *J. Electroanal. Chem.* **2018**, *823*, 610–616.

Full Paper

[27] a) M. Dervisevic, E. Çevik, M. Şenel, *Enzyme Microb. Technol.* **2015**, *68*, 69–76; b) X. Zhou, X. Dai, J. Li, Y. Long, W. Li, Y. Tu, *Mater. Sci. Eng. C* **2015**, *49*, 579–587.

[28] a) F. N. Comba, M. R. Romero, F. S. Garay, A. M. Baruzzi, *Anal. Biochem.* **2018**, *550*, 34–40; b) J.-C. Chou, J.-S. Chen, Y.-H. Liao, C.-H. Lai, M.-S. Huang, T.-Y. Wu, B.-Y. Zhuang, S.-J. Yan, H.-T. Chou, C.-C. Hsu, *Mater. Lett.* **2016**, *175*, 241–243; c) H. A. Wahab, A. A. Salama, A. A. El Saeid, M. Willander, O. Nur, I. K. Battisha, *Results Phys.* **2018**, *9*, 809–814.

[29] S. Rajendran, D. Manoj, K. Raju, D. D. Dionysiou, M. Naushad, F. Gracia, L. Cornejo, M. A. Gracia-Pinilla, T. Ahamad, *Sens. Actuators B* **2018**, *264*, 27–37.

[30] B. N. Aini, S. Siddiquee, K. Ampon, K. F. Rodrigues, S. Suryani, *Sens. Bio-sens. Res.* **2015**, *4*, 46–56.

[31] L. Luo, Q. Li, Y. Xu, Y. Ding, X. Wang, D. Deng, Y. Xu, *Sens. Actuators B* **2010**, *145*, 293–298.

[32] Y. Yu, Z. Chen, S. He, B. Zhang, X. Li, M. Yao, *Biosens. Bioelectron.* **2014**, *52*, 147–152.

[33] D. Vanossi, L. Pigani, R. Seeber, P. Ferrarini, P. Baraldi, C. Fontanesi, *J. Electroanal. Chem.* **2013**, *710*, 22–28.

[34] N. Gupta, P. Jain, R. Rana, S. Shrivastava, *Mater. Today* **2017**, *4*, 342–349.

[35] S. Karmakar, K. L. Routray, B. Panda, B. Sahoo, D. Behera, *J. Alloys Compd.* **2018**, *765*, 527–537.

[36] a) R. Bala, M. Kumar, K. Bansal, R. K. Sharma, N. Wangoo, *Biosens. Bioelectron.* **2016**, *85*, 445–449; b) Y. Ghazi, F. Haddadi, H. Kamaladini, *Mol. Cell. Probes* **2018**.

[37] a) S. U. Haque Inamuddin, A. Nasar, B. Rajender, A. Khan, A. M. Asiri, G. M. Ashraf, *Sci. Rep.* **2017**, *7*, 12703; b) H.-C. Liu, C.-C. Tsai, G.-J. Wang, *Nanotechnology* **2013**, *24*, 215101.

[38] C. Moonla, A. Preechaworapun, T. Tangkuaram, *Electroanalysis* **2017**, *29*, 2698–2707.

[39] a) X. B. Kang, G. C. Pang, X. Y. Liang, M. Wang, J. Liu, W. M. Zhu, *Electrochim. Acta* **2012**, *62*, 327–334; b) L.-T. Cai, H.-Y. Chen, *Sens. Actuators B* **1999**, *55*, 14–18.

[40] R. Nenkova, D. Ivanova, J. Vladimirova, T. Godjevargova, *Sens. Actuators B* **2010**, *148*, 59–65.

[41] M. Piano, S. Serban, R. Pittson, G. A. Drago, J. P. Hart, *Talanta* **2010**, *82*, 34–37.

[42] a) Y. Fang, D. Zhang, Y. Guo, Y. Guo, Q. Chen, *Sens. Actuators B* **2015**, *221*, 265–272; b) M. Shukla, Pramila, T. Dixit, R. Prakash, I. A. Palani, V. Singh, *Appl. Surf. Sci.* **2017**, *422*, 798–808; c) Q. Zeng, J.-S. Cheng, X.-F. Liu, H.-T. Bai, J.-H. Jiang, *Biosens. Bioelectron.* **2011**, *26*, 3456–3463.

[43] a) H. Deng, A. K. L. Teo, Z. Gao, *Sens. Actuators B* **2014**, *191*, 522–528; b) T. C. Gokoglan, S. Soylemez, M. Kesik, I. B. Dogru, O. Turel, R. Yuksel, H. E. Unalan, L. Toppare, *Food Chem.* **2017**, *220*, 299–305; c) M. Kesik, F. E. Kanik, G. Hızalan, D. Kozanoglu, E. N. Esenturk, S. Timur, L. Toppare, *Polymer* **2013**, *54*, 4463–4471.

[44] A. A. Saei, J. E. N. Dolatabadi, P. Najafi-Marandi, A. Abhari, M. de la Guardia, *TrAC Trends Anal. Chem.* **2013**, *42*, 216–227.

[45] J. Singh, A. Roychoudhury, M. Srivastava, V. Chaudhary, R. Prasanna, D. W. Lee, S. H. Lee, B. D. Malhotra, *J. Phys. Chem. C* **2013**, *117*, 8491–8502.

[46] J. Li, Y. Tang, J. Yang, Z. Yang, Y. Zhang, X. Hu, *Sens. Actuators B* **2014**, *190*, 549–554.

[47] H. Hu, M. Feng, H. Zhan, *Talanta* **2015**, *141*, 66–72.

[48] P. Rafighi, M. Tavahodi, B. Haghighi, *Sens. Actuators B* **2016**, *232*, 454–461.

[49] M. Baghayeri, H. Veisi, M. Ghanei-Motlagh, *Sens. Actuators B* **2017**, *249*, 321–330.

[50] W. Mao, B. Cai, Z. Ye, J. Huang, *Sens. Actuators B* **2018**, *261*, 385–391.

[51] H. Al-Sagur, S. Komathi, H. Karakaş, D. Atilla, A. G. Gürek, T. Basova, N. Farmilo, A. K. Hassan, *Biosens. Bioelectron.* **2018**, *102*, 637–645.

[52] V. Gautam, K. P. Singh, V. L. Yadav, *Int. J. Biol. Macromol.* **2018**, *111*, 1124–1132.

CURRICULUM VITAE

NAME	TIK OUIRAM
DATE OF BIRTH	01 january 1992
EDUCATION	2010 – 2013 B.Sc in Chemistry Pibulsongkram Rajabhat University GPA 3.78
	2014 – 2015 M.Sc. in Applied Chemistry Maejo University GPA 3.56
	2016 – Present Ph.D. in Applied Chemistry Maejo University GPA 3.75
WORK EXPERIENCE	2017 – 2019 Teaching Assistant Maejo University Thailand